

RL-TR-92-160
Final Technical Report
June 1992

AD-A255 823



2

ACOUSTO-OPTIC APPLICATIONS FOR MULTICHANNEL ADAPTIVE OPTICAL PROCESSOR

Dynetics, Inc.

Dr. Merv C. Budge, Robert J. Berinato, Michael C. Zari



APPROVED FOR PUBLIC RELEASE; DISTRIBUTION UNLIMITED.

92 0 00 090

92-26278

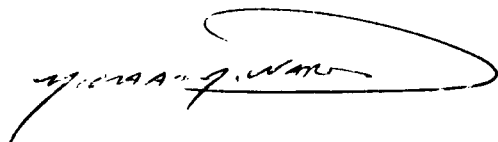


Rome Laboratory
Air Force Systems Command
Griffiss Air Force Base, NY 13441-5700

This report has been reviewed by the Rome Laboratory Public Affairs Office (PA) and is releasable to the National Technical Information Service (NTIS). At NTIS it will be releasable to the general public, including foreign nations.

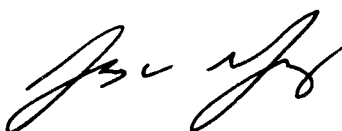
RL-TR-92-160 has been reviewed and is approved for publication.

APPROVED:



MICHAEL J. WARD, Capt, USAF
Project Engineer

FOR THE COMMANDER:



JAMES W. YOUNGBERG, Lt Col, USAF
Deputy Director
Surveillance and Photonics Directorate

If your address has changed or if you wish to be removed from the Rome Laboratory mailing list, or if the addressee is no longer employed by your organization, please notify RL (OCP) Griffiss AFB NY 13441-5700. This will assist us in maintaining a current mailing list.

Do not return copies of this report unless contractual obligations or notices on a specific document require that it be returned.

REPORT DOCUMENTATION PAGE

Form Approved
OMB No. 0704-0188

Public reporting burden for this collection of information is estimated to average 1 hour per response, including the time for reviewing instructions, searching existing data sources, gathering and maintaining the data needed, and completing and reviewing the collection of information. Send comments regarding this burden estimate or any other aspect of this collection of information, including suggestions for reducing this burden, to Washington Headquarters Services, Directorate for Information Operations and Reports, 1215 Jefferson Davis Highway, Suite 1204, Arlington, VA 22202-4302, and to the Office of Management and Budget, Paperwork Reduction Project (0704-0188), Washington, DC 20503.

1. AGENCY USE ONLY (Leave Blank)		2. REPORT DATE June 1992		3. REPORT TYPE AND DATES COVERED Final Feb 91 - Feb 92	
4. TITLE AND SUBTITLE ACOUSTO-OPTIC APPLICATIONS FOR MULTICHANNEL ADAPTIVE OPTICAL PROCESSOR				5. FUNDING NUMBERS C - F30602-91-D-0001 PE - 62702F Task 5 PR - 4600 TA - P1 WU - PE	
6. AUTHOR(S) Dr Merv C Budge, Robert J Bertinato, Michael C Zari					
7. PERFORMING ORGANIZATION NAME(S) AND ADDRESS(ES) Dynerics, Inc. P.O. Drawer B Huntsville AL 35814-5050				8. PERFORMING ORGANIZATION REPORT NUMBER	
9. SPONSORING/MONITORING AGENCY NAME(S) AND ADDRESS(ES) Rome Laboratory (OCPA) Griffiss AFB NY 13441-5700				10. SPONSORING/MONITORING AGENCY REPORT NUMBER RL-TR-92-160	
11. SUPPLEMENTARY NOTES Rome Laboratory project engineer: Michael Ward, Capt, USAF/ OCPA/315-330-2944 Prime Contractor: SRI Intl, 333 Ravenswood Ave, Menlo Park CA 94025					
12a. DISTRIBUTION/AVAILABILITY STATEMENT Approved for public release; distribution unlimited.				12b. DISTRIBUTION CODE	
13. ABSTRACT (Maximum 200 words) This final report describes the design and hardware implementation of an acousto-optic (AO) multichannel adaptive optical processor (MADOP) for application to the cancellation of multipath jamming interference in advanced surveillance radars. The primary objective of this effort was the design and preliminary fabrication of a multichannel adaptive system that can perform cancellation of multiple wideband (10 MHz) jamming interference in the presence of multipath. The MADOP system is composed of three primary subsystems. A multichannel time-integrating AO correlator performs a correlation between the residual cancellation error and each of the auxiliary omnidirectional antennas to arrive at updates for each of the adaptive weight functions. A digital interface accepts this update information and generates the appropriate adaptive weight functions for performing auxiliary channel filtering. Finally, a multichannel AO tapped delay line (AOTDL) filter system accepts these weight functions through an AO spatial light modulator (AOSLM) and taps the auxiliary channel inputs to form the estimate of the noise signal in the main receiver channel. This noise signal estimate is then subtracted from the main receiver channel at the system intermediate frequency to form the residual cancellation error for input to the multichannel time-integrating AO correlator, thereby closing the adaptive loop.					
14. SUBJECT TERMS Adaptive processing, acousto-optics, optical signal processing				15. NUMBER OF PAGES 150	
				16. PRICE CODE	
17. SECURITY CLASSIFICATION OF REPORT UNCLASSIFIED	18. SECURITY CLASSIFICATION OF THIS PAGE UNCLASSIFIED	19. SECURITY CLASSIFICATION OF ABSTRACT UNCLASSIFIED	20. LIMITATION OF ABSTRACT UL		

ABSTRACT

This final report describes the design and hardware implementation of an acousto-optic (AO) multichannel adaptive optical processor (MADOP) for application to the cancellation of multipath jamming interference in advanced surveillance radars. The primary objective of this effort was the design and preliminary fabrication of a multichannel adaptive system that can perform cancellation of multiple wide-band (10 MHz) jamming interference in the presence of multipath. The MADOP system is composed of three primary subsystems. A multichannel time-integrating AO correlator performs a correlation between the residual cancellation error and each of the auxiliary omnidirectional antennas to arrive at updates for each of the adaptive weight functions. A digital interface accepts this update information and generates the appropriate adaptive weight functions for performing auxiliary channel filtering. Finally, a multichannel AO tapped delay line (AOTDL) filter system accepts these weight functions through an AO spatial light modulator (AOSLM) and taps the auxiliary channel inputs to form the estimate of the noise signal in the main receiver channel. This noise signal estimate is then subtracted from the main receiver channel at the system intermediate frequency to form the residual cancellation error for input to the multichannel time-integrating AO correlator, thereby closing the adaptive loop.

DTIC QUALITY INSPECTED 3

Accession For	
NTIS GRA&I	<input checked="checked" type="checkbox"/>
DTIC TAB	<input type="checkbox"/>
Unannounced	<input type="checkbox"/>
Justification	
By	
Distribution/	
Availability Codes	
Dist	Avail and/or Special
A-1	

TABLE OF CONTENTS

	<u>Page</u>
1. INTRODUCTION.....	1-1
2. SYSTEM CONCEPT AND REQUIREMENTS	2-1
2.1 RADAR SYSTEM OVERVIEW AND REQUIREMENTS.....	2-1
2.1.1 Signal Representations	2-4
2.1.2 Delay Resolution Requirements.....	2-5
2.2 SURVEILLANCE TEST-BED ASSESSMENT	2-9
3. ADAPTIVE CANCELLATION ALGORITHM AND SIMULATION.....	3-1
3.1 ADAPTIVE CANCELLATION ALGORITHM	3-1
3.2 SIMULATION ACTIVITIES	3-4
3.2.1 OJC1	3-4
3.2.2 OJC2	3-9
3.2.3 OJC3	3-9
4. MULTICHANNEL ADAPTIVE OPTICAL PROCESSOR DESIGN AND IMPLEMENTATION.....	4-1
4.1 OVERALL SYSTEM ARCHITECTURE	4-2
4.2 TIME-INTEGRATING CORRELATION FOR WEIGHT FUNCTION CALCULATION.....	4-6
4.2.1 Design Alternative I: In-Line Multichannel Correlator Architecture	4-6
4.2.2 Design Alternative II: Two-Path Multichannel Correlator Architecture	4-20
4.2.3 Time-Integrating Correlator Architectural Considerations	4-39
4.3 AOTDL FILTER.....	4-45
4.3.1 AOTDL Interferometric Architecture Design and Limitations.....	4-46
4.3.2 Noninterferometric Architecture Design and Implementation.....	4-64
4.3.3 AOSLM Intermodulation Products.....	4-90

TABLE OF CONTENTS (Concluded)

	<u>Page</u>
5. CONCLUSIONS AND RECOMMENDATIONS	5-1
5.1 RADAR INSERTION CONSIDERATIONS	5-1
5.2 MADOP HARDWARE DEVELOPMENT CONSIDERATIONS	5-2
APPENDIX A. MATLAB SIMULATION ROUTINES.....	A-1
REFERENCES.....	R-1

LIST OF ILLUSTRATIONS

<u>Figure</u>	<u>Title</u>	<u>Page</u>
2-1	Two-Dimensional Operational Scenario for MADOP	2-2
2-2	Surveillance Radar Simplified Schematic with Adaptive IF Processing	2-3
2-3	Geometry for TDOA	2-6
2-4	TDOA Versus Angle Off Boresight Referenced to 1 m of Antenna Separation	2-7
2-5	Angular Resolution Versus Antenna Separation Referenced to 5-ns Delay Resolution	2-8
3-1	Classical Multichannel LMS Adaptive Filter	3-2
3-2	OJC1 Simulation Performance	3-5
3-3	OJC2 Simulation Performance	3-10
3-4	OJC3 Simulation Performance	3-12
4-1	MADOP System Layout for Two Channels	4-3
4-2	Possible Signal and Interference Sources	4-4
4-3	Electronic Interfaces	4-5
4-4	Conceptual Layout for In-Line Correlator	4-7
4-5	Schlieren Image of NEOS AO Cell	4-9
4-6	Laser Diode Dynamic Range Measurements	4-12
4-7	In-Line Correlator Breadboard Design	4-14
4-8	Autocorrelation of $s(t)$ (In-Line); $s(t)$ = Pulse, $\tau = 0.5 \mu\text{s}$, $T = 2.5 \mu\text{s}$, $f_0 = 10 \text{ MHz}$	4-16
4-9	In-Line Autocorrelation Results	4-17
4-10	In-Line Correlator Dynamic Range Measurements	4-21
4-11	Illumination of CCD Array - No Modulation Input to Laser Diode, Tone Into AO Cell	4-23
4-12	Conceptual Layout for Two-Channel Two-Path Correlator	4-24
4-13	Two-Path Time-Integrating Correlator	4-27
4-14	Spatial Fringe Frequency/Orientation as Function of Acoustic Beam Image Overlap Positions	4-29
4-15	Multichannel Correlation of 5 MHz Noise Source Input	4-30

LIST OF ILLUSTRATIONS (Continued)

<u>Figure</u>	<u>Title</u>	<u>Page</u>
4-16	Multichannel Correlation of 1 MHz Square Wave Input	4-32
4-17	Interferometric Path Optical Layout.....	4-35
4-18	Electronics Design for Signal Inputs to AO Cells	4-36
4-19	Correlation Results: $s(t) = 500$ kHz Sinusoid	4-37
4-20	Noise Autocorrelation.....	4-40
4-21	Two-Path Correlator Dynamic Range Measurements	4-41
4-22	In-Line Schematic Illustrating Additional Delay Required in LD Path.....	4-45
4-23	Tapped-Delay Line Architecture (Two Taps Shown)	4-47
4-24	Representative Tapped Delay Line Signals	4-58
4-25	AO Heterodyning Phenomenology.....	4-61
4-26	Noninterferometric Tapped Delay Line Architecture	4-65
4-27	Optical Layout for Multichannel AOTDL Architecture.....	4-71
4-28	RF Layout for Multichannel AOTDL Architecture	4-72
4-29	Cancellation of a Single Tone	4-74
4-30	Cancellation of a 3.2-MHz Separation, Two-Tone Waveform.....	4-75
4-31	Cancellation of a 10-MHz Separation, Two-Tone Waveform.....	4-76
4-32	AOTDL System Test Measurements (Case 1).....	4-77
4-33	AOTDL System Test Measurements (Case 2).....	4-83
4-34	Network Analyzer Measurement Setup.....	4-86
4-35	Tapped Delay Line Frequency Response for $f_{ER} = 69.4$ MHz	4-87
4-36	Tapped Delay Line Frequency Response for $f_{ER} = 72.8$ MHz	4-88
4-37	Tapped Delay Line Phase Response for $f_{ER} = 69.4$ MHz	4-89
4-38	Two-Tone Intermodulation Products	4-91
4-39	Two-Tone Intermodulation Dynamic Ranges of Longitudinal TeO_2 Bragg Cells for Several Acoustic Power Densities	4-92

LIST OF ILLUSTRATIONS (Concluded)

<u>Figure</u>	<u>Title</u>	<u>Page</u>
4-40	Three-Tone Intermodulation Products	4-93
A-1	Flowchart for OJC1	A-2

LIST OF TABLES

<u>Table</u>	<u>Title</u>	<u>Page</u>
2-1	Feasibility Demonstration Goals	2-4
4-1	Optical Path Length Parameters	4-28
4-2	Time-Integrating Correlator Architecture Features.....	4-44
4-3	Amplitude Response Versus Tap Position.....	4-59
A-1	Parameters Employed in OJC1, OJC2, and OJC3	A-1

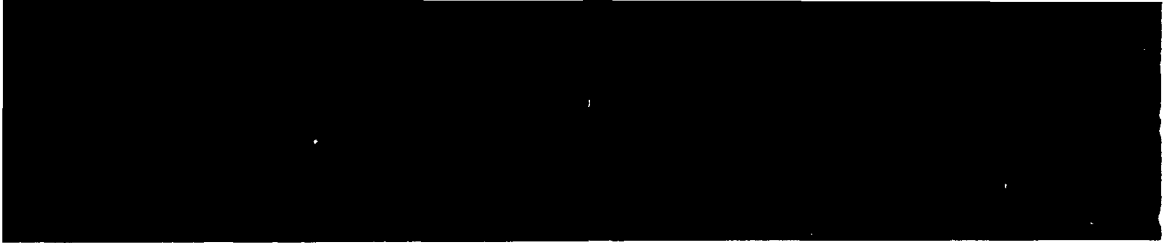
1. INTRODUCTION

This final report describes the design and hardware implementation of an acousto-optic (AO) multichannel adaptive optical processor (MADOP), for application to the cancellation of multipath jamming interference in advanced surveillance radars. This Expert in Science and Engineering (ESE) effort is a continuation of an ongoing program within the Rome Laboratory Photonics Center (References 1 through 4). Greater than half of the Dynetics, Inc., effort was performed on-site at Rome Laboratory, Griffiss Air Force Base, N.Y. This work was accomplished in conjunction with Photonics Center personnel: CPT Michael Ward, CPT Christopher Keefer, and 1LT Harold Andrews under the In-House Project 4600P1063; and Dr. Stephen Welstead of COLSA, Inc., who was under a separate ESE contract. All work reported herein was performed under ESE Contract F30602-91-D-0001, Subcontract C-140545, during the period 1 February 1991 to 31 January 1992.

The primary objective of this effort was the design and preliminary fabrication of a multichannel adaptive system that can perform cancellation of multiple wideband (10 MHz) jamming signals in the presence of multipath. In developing this system, it was recognized that emphasis must be placed on the effective interface of the MADOP to experimental radar test-beds. For the radar system applications pursued in this effort, cancellation is best performed at the radar intermediate frequency (IF), which, for our design, is 80 MHz. Therefore, the MADOP, when properly interfaced, acts as a "black box" component within the IF chain of the radar. This approach drove the design away from earlier architectures that performed cancellation at baseband.

The MADOP system is composed of three primary subsystems: a multichannel time-integrating AO correlator that performs a correlation between the residual cancellation error and each of the auxiliary omnidirectional antennas to arrive at updates for each of the adaptive weight functions; a digital interface that accepts the update information and generates the appropriate adaptive weight functions for performing auxiliary channel filtering; and a multichannel AO tapped delay line (AOTDL) system that accepts the weight functions through an AO spatial light modulator (AOSLM) and taps the auxiliary channel inputs to form the estimate of the noise signal in the main receiver channel. This noise signal estimate is then subtracted from the main receiver channel at the system IF to form the residual cancellation error for input to the multichannel time-integrating AO correlator, thereby closing the adaptive loop. The emphasis of the system design during this effort has been on the two AO subsystems. Some assistance has been provided by Dynetics, Inc., toward the design of the digital interface, and it is anticipated that this digital subsystem will be increasingly emphasized as integration into radar test-beds draws near.

This technical report is organized as follows: After this introduction, the radar system application and design-to requirements are provided in Section 2, with emphasis on the integration of the MADOP into a radar testbed at an IF of 80 MHz. This is followed in Section 3 by a description of the adaptive signal



processing algorithms being implemented, including initial simulation results. The analysis, design, and hardware implementation of the multichannel AO subsystems constitutes the majority of the report and is presented in detail in Section 4. Conclusions and recommendations for continued development of this promising technology are presented in Section 5.

2. SYSTEM CONCEPT AND REQUIREMENTS

The MADOP has been designed to achieve time-domain cancellation of interference sources in the presence of a multipath environment. As designed, the system will be able to cancel four independent interference sources, each having up to four multipaths, with each source having up to a 10 MHz bandwidth. The initial implementation emphasizes two channels. The key advantage of our optical approach over the current state-of-the-art in digital and analog electronic implementations is the ability to cancel wideband signals (greater than 1 MHz) by using multiple tap weights per channel. Subsection 2.1 states the specific design-to requirements and summarizes the radar problem being addressed. This discussion emphasizes the ultimate integration of the MADOP black box into radar systems, and the interfaces required. Subsection 2.2 reviews the analysis performed under the current effort to assess the suitability of available test-beds at Rome Laboratory for testing the MADOP system.

2.1 RADAR SYSTEM OVERVIEW AND REQUIREMENTS

Surveillance in the presence of multipath jamming interference is an extremely demanding problem due to the multidimensional nature of the cancellation required. This is especially true for wideband interference sources that have several multipath delays. This subsection will begin with a general overview of the radar system block diagram and how the MADOP black box would fit into the system.

Figure 2-1 presents an illustrative summary of the scenario being addressed. In this figure, two independent interference sources, $n_1(t)$ and $n_2(t)$, having spectral content in the radar system passband, contaminate the directional main antenna target return, $s(t)$, through the sidelobes. The multipath versions of the two interference sources also contribute a significant noise term to the main channel signal resulting in the reception of:

$$d(t) = s(t) + \sum_{n=1}^N a_{1n} n_1(t - \tau_{1n}) + \sum_{m=1}^M a_{2m} n_2(t - \tau_{2m}), \quad (2-1)$$

where a_{1n} and a_{2m} represent relative attenuations due to multipath losses together with antenna sidelobe gain relative to mainlobe gain, and τ_{1n} and τ_{2m} represent the signal delays. The direct-path interference is given for $n = 1$ and $m = 1$. It is assumed that the interference noise is on the order of, or much larger than, the target return, $s(t)$, resulting in negative signal-to-noise ratio (SNR) in the main antenna. The two omnidirectional auxiliary antennas receive the interference noise but the target return entering these antennas is negligible because of the low main-channel SNR assumption. Thus, the two auxiliary antennas receive the signals:

$$N_1(t) = \sum_{n=N+1}^{2N} a_{1n} n_1(t - \tau_{1n}) + \sum_{m=M+1}^{2M} a_{2m} n_2(t - \tau_{2m}),$$

$$N_2(t) = \sum_{n=2N+1}^{3N} a_{1n} n_1(t - \tau_{1n}) + \sum_{m=2M+1}^{3M} a_{2m} n_2(t - \tau_{2m}).$$

(2-2)

In addition to these correlated noises, uncorrelated receiver noise is present at each antenna.

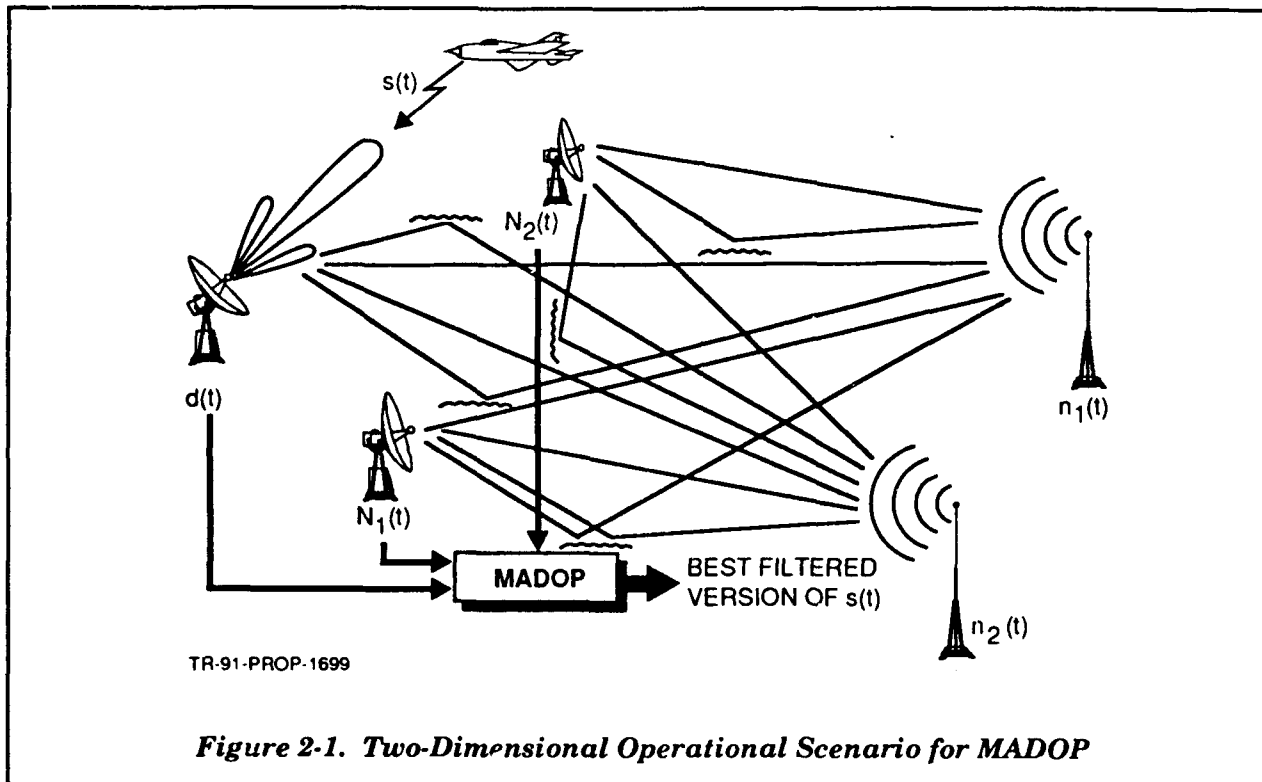
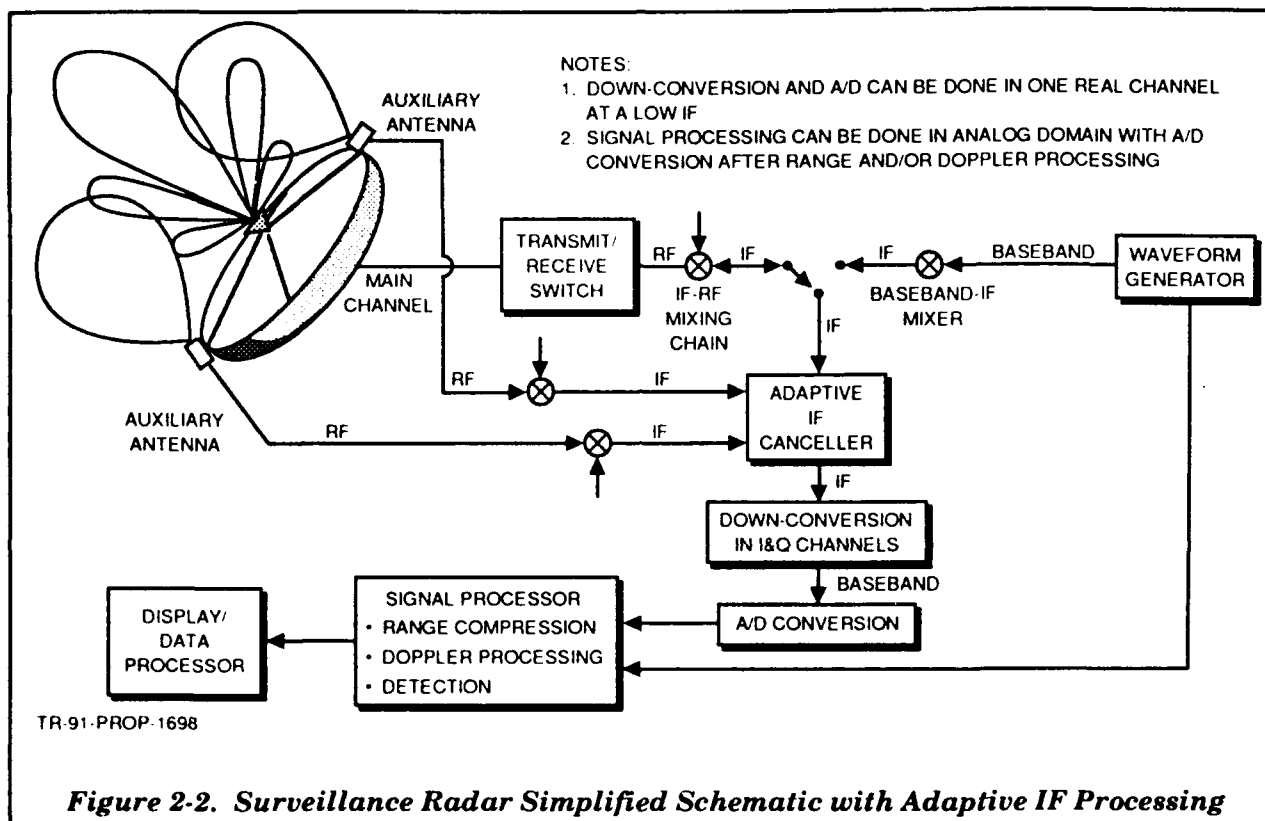


Figure 2-1. Two-Dimensional Operational Scenario for MADOP

Figure 2-2 shows a simplified block diagram of a typical surveillance radar that may benefit from the MADOP. This diagram is not intended to represent a specific radar system. The MADOP is shown in this figure at the appropriate point in the signal processing chain. First note that the processing is done at the radar IF after downconversion from the radio frequency (RF) carrier (3 or 10 GHz for example). The waveform generator provides the signal to be transmitted and also provides the matched filter to the signal processor to allow for pulse compression and pulse integration/Doppler filtering. The antenna system, whether phased-array or dish, forms a beam (or multiple independent beams, as possible with a phased-array antenna) that illuminates the target in the presence of interference. The target reflection, contaminated by interference and noise, is received in the main channel, while the interference is also received in auxiliary antenna channels (which can be portions of a single phased array). All signals are

downconverted to the IF and input into the MADOP. The output of the MADOP is the desired signal with the interference suppressed. This signal then enters the coherent pulse compression and Doppler filtering system, which is often implemented digitally following analog to digital (A/D) conversion of in-phase and quadrature (I&Q) channels. After this signal processing, target detection takes place using some form of constant false alarm rate (CFAR) processing. The data processor performs such operations as target tracking, beam scheduling, system control, and interface to the display.



As stated above, the goal of the adaptive processor is to react to the multipath interference environment in such a way that the main antenna noise is canceled, resulting in a satisfactory SNR for further processing. The algorithm for achieving this objective, together with simulated results, will be described in Section 3. The goals for this feasibility demonstration program, as coordinated with personnel in the Surveillance Technology Division of the Surveillance and Photonics Directorate (OCTS), are shown in **Table 2-1**. It is recognized that although the loop lock time (time to reach steady state) is critical in system applications (500 μ s is desirable), the personal computer interface in the digital subsystem makes practical loop lock times unachievable. The development of real-time, special-purpose digital interfaces will greatly increase system speed.

Table 2-1. Feasibility Demonstration Goals

System Bandwidth (MHz)	10
Number of Interference Sources	4 (initial demo will accommodate 2)
Maximum Multipath Delay (μ s)	5 (corresponds to 1.5-km differential path)
Interference Cancellation Ratio (dB)	30
Number of Multipath Delays	>4
Loop Lock Time (ms)	5
Processor IF (MHz)	80

2.1.1 Signal Representations

The carrier frequency of the main and auxiliary antennas is generally much higher than the desired signal processing IF. Therefore, the radar will mix the signal down to the signal processor's IF, f_{IF} (80 MHz). The radar will not demodulate the signal down to baseband and then modulate the signal back to the IF for processing. The signal processor must therefore not be restricted to the processing of double sideband suppressed carrier (DSB-SC) modulated signals (real modulations of a carrier). An example of a signal that must be accommodated is a single-tone interference source. Although this is the case, it is appropriate to use DSB-SC signals as test waveforms in characterizing the processor. In addition, it is desirable to use DSB-SC waveforms as opposed to amplitude modulation (AM), which has a dc component at baseband. These DSB-SC waveforms are more representative of realistic signals.

In general, the signal return and the interference noise terms are complex modulations of a carrier and must be expressed in I&Q channels at baseband. Let the baseband representation, $g_m(t)$, of a signal, $g(t)$, be given as:

$$g_m(t) = g_I(t) + jg_Q(t) = A(t) \exp[j\phi(t)] \quad (2-3)$$

where $g_I(t)$ and $g_Q(t)$ are the I&Q channel signals, respectively, and $A(t)$ and $\phi(t)$ are the signal magnitude and phase, respectively. On a carrier frequency, f_c , the resultant signal, $g(t)$, is given as:

$$\begin{aligned} g(t) &= \text{Re} \{ g_m(t) \exp[j2\pi f_c t] \} = g_I(t) \cos 2\pi f_c t - g_Q(t) \sin 2\pi f_c t \\ &= A(t) \cos [2\pi f_c t + \phi(t)]. \end{aligned} \quad (2-4)$$

A property of this modulation is that to preserve the information at baseband, I&Q channels must be employed. Also, the bandwidth of a signal on a carrier is the same as at baseband, where the I and Q channels each contain half the bandwidth of the total signal. For DSB-SC modulation, the carrier modulated

signal covers twice the bandwidth of the baseband representation. This is another way of visualizing the loss of information when demodulating a complex signal in one real channel. Therefore, earlier approaches to cancellation that relied on DSB-SC modulation (Reference 1) are not general enough to handle arbitrary modulations.

To visualize the correlation that will result between the residual error and the auxiliary channel inputs (the algorithm is further discussed in Section 3), it is helpful to examine the bandwidth properties of signals. The autocorrelation of a signal will have a half-power (3 dB) width approximately equal to the inverse bandwidth. Thus, a 10-MHz bandwidth signal will have an autocorrelation width of 100 ns, while a 1-MHz bandwidth signal will have an autocorrelation width of 1000 ns. It is evident that for multipath delays of less than, or on the order of the inverse signal bandwidth, there will be significant overlap in the correlation peaks, which severely complicates any peak-finding algorithm. The phase of each correlation may provide information useful to resolving the presence of two or more peaks, but the problem is still severe. In addition, the interaction of the phases of the two overlapping peaks changes the general appearance of the envelope significantly. For example, two closely spaced peaks can be made to look like one peak, or a null of tens of dB can be placed between them, depending on the relative phases of the peaks.

Another consideration is the positioning of the correlation peaks and the total number of peaks for a given scenario. First, note that for a source and its multipath replica, the cross-correlation between two antennas yields four peaks. The multipath delay is, in general, different for each antenna; if not, there appears to be just one signal to cancel without multipath. The number of peaks will be the square of the number of multipaths. The ultimate goal of the processor is to cancel four interference sources, each having four multipaths. When four independent interference sources are considered, each having four multipaths, and four auxiliary antennas, the total number of correlation peaks will be 64 per channel (16 per interference source), for a total of 256 correlation peaks. These issues must be considered in designing a robust algorithm for noise cancellation.

2.1.2 Delay Resolution Requirements

Current program goals include a total multipath delay capability of 5 μ s, but consideration of direct path delay is also an important issue. The issues related to direct path cancellation will be described in this subsection, and their impact on system development will be assessed. In addition to the impact on system design and performance, the spatial nature of the cancellation, i.e., the sidelobe cancellation viewpoint, will become evident.

Figure 2-3 shows a scenario containing only direct path jamming interference from a single source, and a single auxiliary antenna to cancel interference in the main channel. Consider an antenna separation, d , and assume that the jamming source is in the far-field. For this case, the time-difference-of-

arrival (TDOA) of an interference signal at the two antennas is determined only by the angle, Θ , of the source in the far-field, relative to the antenna boresight. This TDOA is given geometrically as:

$$\text{TDOA}(\Theta) = \frac{d \sin \Theta}{c} \quad (2-5)$$

where c is the speed of light. This forms the basis for true time-delay beamforming. **Figure 2-4** graphs this relationship as the ratio of the TDOA to d , the antenna separation. For example, for an antenna separation of 10 m and an angle off boresight of 5° , the TDOA is 2.9 ns. Thus, if the antenna system is to cancel the interference in this direction (sidelobe cancellation in the space domain), the delay must be set to precisely this value. For two such interference sources, the resolution between taps must be this precise to achieve cancellation of both sources while, at the same time, preserving the mainbeam integrity.

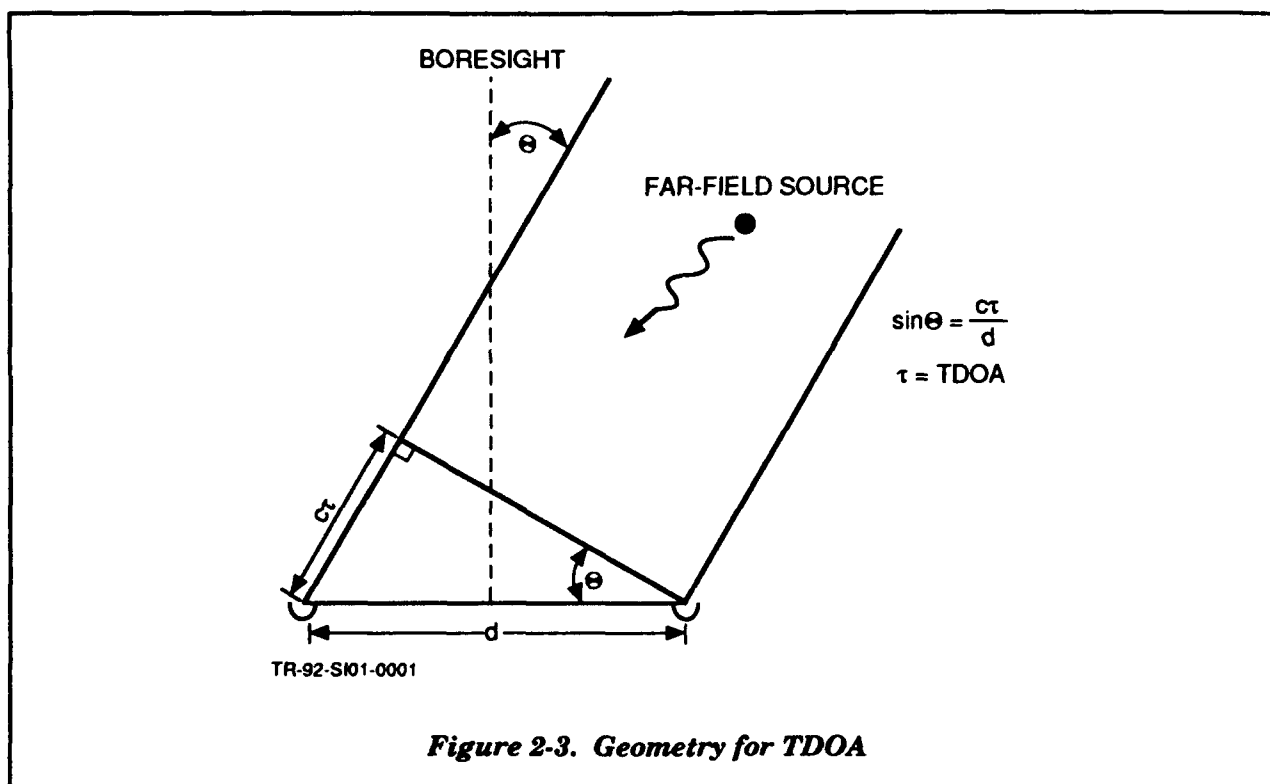
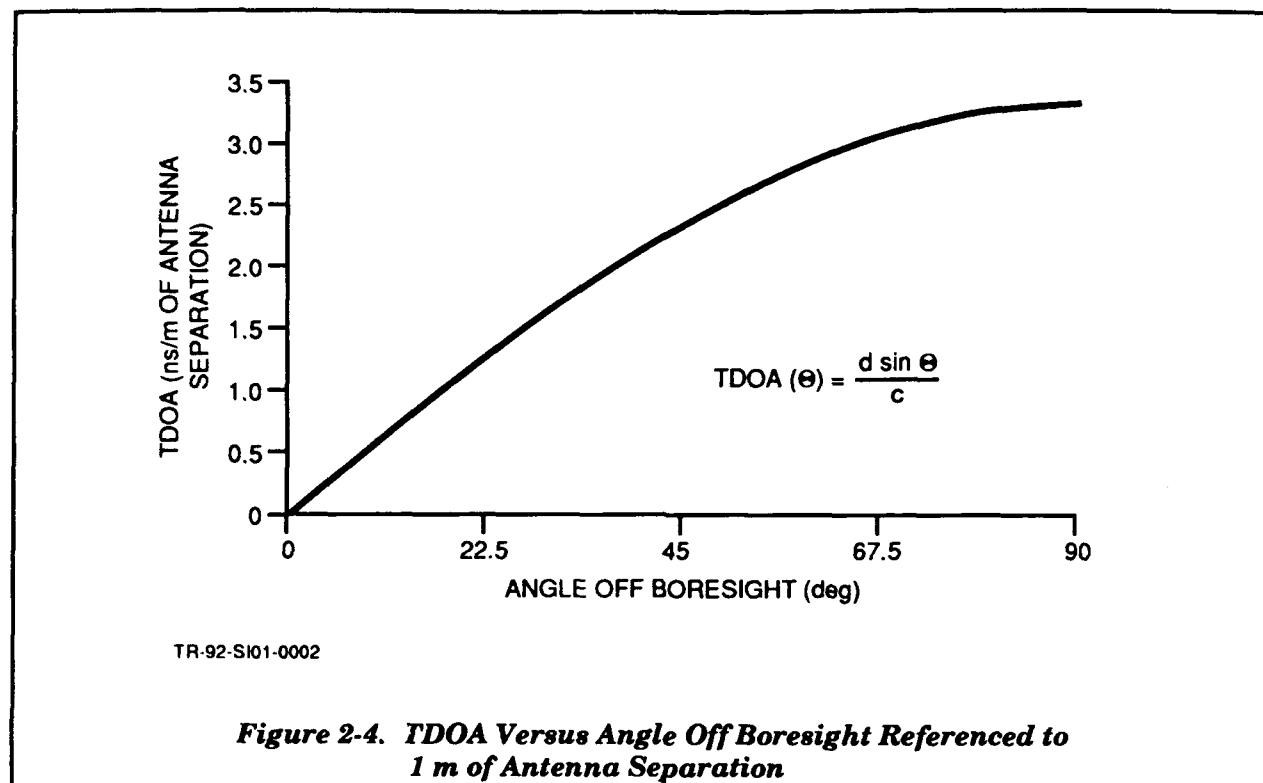


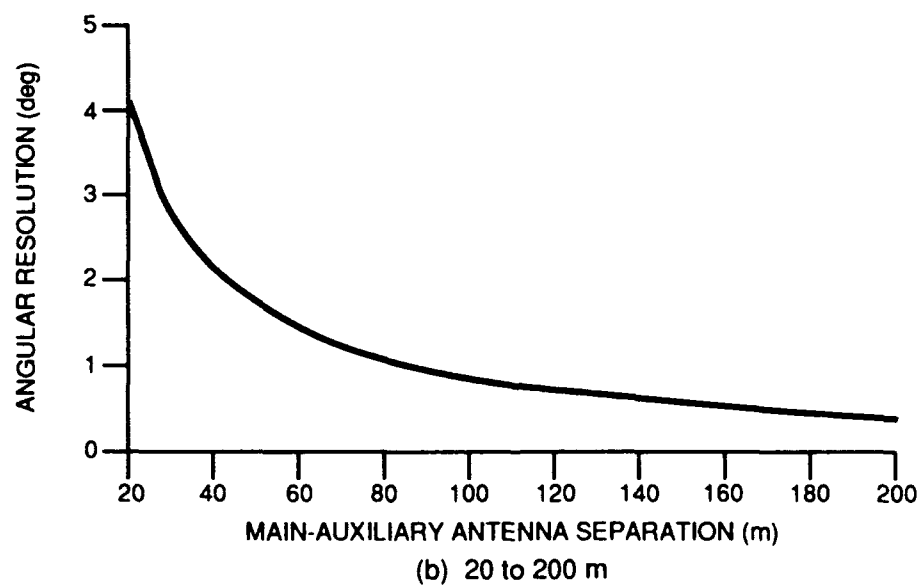
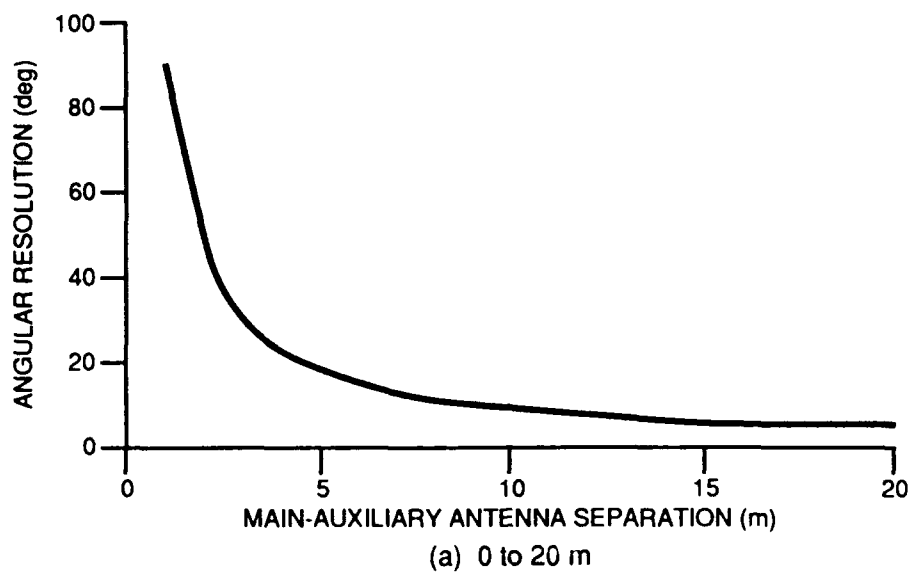
Figure 2-5 further clarifies this relationship for a canceller having a resolution of 5 ns over a $5 \mu\text{s}$ delay window (1000 resolvable spots for the AOSLM to be discussed in Section 4). For this constraint, the angular resolution of the canceller will be a function of the antenna separation. **Figure 2-5(a)** illustrates the poor angular resolution achieved for a 5-ns delay resolution when closely spaced antennas are employed. To achieve an angular resolution of 3° , an antenna separation of 28.7 m is required, as shown in **Figure 2-5(b)**. For small antenna separations, characteristic of auxiliary antennas that are part of a larger

phased-array main antenna or mounted on the main antenna, the delay resolution must be very precise to cancel direct-path jamming with high angular resolution.



If the interference reaches the auxiliary antenna and the main antenna with a TDOA of less than d/c ($\theta = 90^\circ$), the appropriate spatial direction will be cancelled. For this case, which will most likely occur for each multipath reflection reaching both antennas, the interference source appears to be at a given spatial direction. If the multipath delay is greater than this, it is appropriate to consider the cancellation process in the temporal domain without consideration of spatial cancellation. In the special case of multipath reaching the main and auxiliary antennas simultaneously, the system will have the undesirable effect of cancelling the mainbeam return, even though the jammer is spatially in the sidelobes.

For the AOTDL filter system to be described in detail in Subsection 4.2, the impact of this requirement is best viewed in terms of the number of resolvable spots in the AOSLM system. The accuracy of the taps can be very precise, but the resolution of two closely spaced taps will most likely be limited to less than the time bandwidth (BT) product of the AOSLM, typically on the order of 1000. A possible solution to this constraint is to use very high temporal resolution over a very small delay window, and then to form coarser taps over the total 5 μ s window. This could possibly be achieved in a single optical system, or may be performed by a large delay window multipath optical canceller in conjunction with a traditional electronic sidelobe canceller.



TR-92-SI01-0003

**Figure 2-5. Angular Resolution Versus Antenna Separation
Referenced to 5-ns Delay Resolution**

2.2 SURVEILLANCE TEST-BED ASSESSMENT

During the on-site support, meetings with personnel from organizations outside the Photonics Center were held to identify potential test-beds for the MADOP system. The first meeting was concerned with the L-band and S-band radars operated by OCTS. The discussions were specifically concerned with attempting to determine if the MADOP would be useful in the aforementioned radars and whether one of the radars could serve as a test-bed for evaluating the MADOP. It was concluded that the mission of these two radars is such that the MADOP would not be useful. In particular, these radars appear to be test-beds that are used to evaluate concepts proposed by other organizations. OCTS would not have a need to incorporate an adaptive interference canceller since it would not enhance the role of the radars as test-beds. The L-band and S-band radars also would not serve as good test-beds for evaluating the MADOP. This conclusion stems from a perception that it would be very difficult to interface the MADOP to the radars or to configure them to provide data that could be used to exercise the MADOP in an off-line fashion. The main difficulty lies in the fact that there was no evidence that the radars had the auxiliary antennas and receiver channels required for this application.

A second meeting was held with personnel from OCDR. The purpose of this meeting was to discuss the C-band radar operated by OCDR. This radar is a 6 by 12 ft planar phased array that was developed for electronic counter-countermeasure (ECCM) testing. As with the L- and S-band radars, the mission of this radar is not such that the MADOP would be useful in it. However, it could serve as a test-bed for evaluating the MADOP. It has an auxiliary antenna and extra receiver channels that can be used to interface to the MADOP. All the receiver channels are readily available and provide outputs at the proper IF. They also appear to have bandwidths that are compatible with the capabilities of the MADOP. The radar has a second auxiliary antenna that could be mounted near the existing auxiliary antenna to provide two auxiliary channels. Furthermore, it might be possible to form additional auxiliary channels by accessing individual subarrays of the main array. However, before such an approach is tried, it would be necessary to obtain details on the scanning characteristics of the subarray. If the subarrays are scanned, this could introduce complications into the operation of the MADOP. Other attractive features of the C-band array radar are the two jammers and a boresight tower associated with it. If a corner reflector or some type of signal repeater could be attached to the boresight tower, it could provide a target signal source for some of the testing.

A third meeting was held with personnel from C3BA. This group has an X-band communications-type system that they use to study sidelobe cancellation and other functions. The system consists of a 12-horn antenna with one receiver channel per horn. All of the beamforming, sidelobe cancellation, and other processing are done at baseband by a digital computer. They have not pursued the area of noise cancellation, nor are they conveniently set up to do so. Because of this, it is questionable as to whether this

system would provide a good test-bed for the MADOP. If the MADOP were to be modified to serve as a sidelobe canceller, this facility might be useful for testing.

A fourth meeting was held with personnel from OCDE on the potential application of photonics to radars. A system that was of some interest in terms of the MADOP was their 256-element patch array. They apparently plan to use this array to study sidelobe cancellation and adaptive beamforming techniques. At a later time, this radar could also serve as a test-bed for the MADOP. Another thought is that if the MADOP was converted to a sidelobe canceller or a piece of hardware to support adaptive beamforming, OCDE might be interested in using it in their patch array.

It appears that the MADOP is maturing to a point where it can be tested in a radar. To this end, there are several issues related to potential performance and system implementation that must be addressed. One of these is a concern for how the MADOP performs relative to a multichannel jamming suppression system that does not contain the delay-line feature. A further concern is whether or not the existing version of the MADOP offers better performance than an interference canceller that does not include the delay-line feature. There is a related issue of whether the nondelay-line version could be easily implemented with optical processing techniques. It is recommended that this area be pursued with analysis and simulation.

Another area of performance that should be considered is the convergence time of the MADOP. This impacts the implementation, use and performance of the radar when it incorporates the MADOP. It may be that all pulses transmitted during the convergence period will not be available for other signal processing functions. The net effect of this is a loss in radar resources. If the convergence period is a significant portion of the processing interval, this could seriously impact system performance. Another area related to convergence time is the use of the MADOP in a continuously scanning search radar. If the convergence time is too large, the scan rate of the radar would have to be slowed, which could affect overall performance of the radar. Of course, if jamming is severe enough, the resultant performance degradation could be much worse due to convergence. Also related are the effects of MADOP operation on clutter cancellation, pulse distortion, target parameter measurements, and probably many others.

In the area of system implementation, the problem exists as to just how the jammer suppression system should be implemented in the sum and difference channels of the radar and what effect the jammer suppression system would have on monopulse performance. It should also be noted that for search radars, which typically do not employ monopulse techniques, this may not be a problem; for track radars however, it will definitely be an issue. Furthermore, the impact on performance will depend upon the type of monopulse processing; e.g., two channel, three channel, or four channel. There is also a need to consider the implementation impact on multiple-beam antennas.

3. ADAPTIVE CANCELLATION ALGORITHM AND SIMULATION

The cancellation of noise from desired signals using auxiliary channel inputs has been applied to a number of systems with success (References 5 through 7). In addition, the application of optical, and more specifically acousto-optic (AO), signal processing techniques to the adaptive filtering problem has been researched by others (References 8 through 14). Subsection 3.1 will present a summary of the specific adaptive algorithm being implemented by the MADOP system, and will point out differences between this algorithm and those employed by others. Following this theoretical development, a number of alternative weight update and application schemes will be compared through simulation in Subsection 3.2.

3.1 ADAPTIVE CANCELLATION ALGORITHM

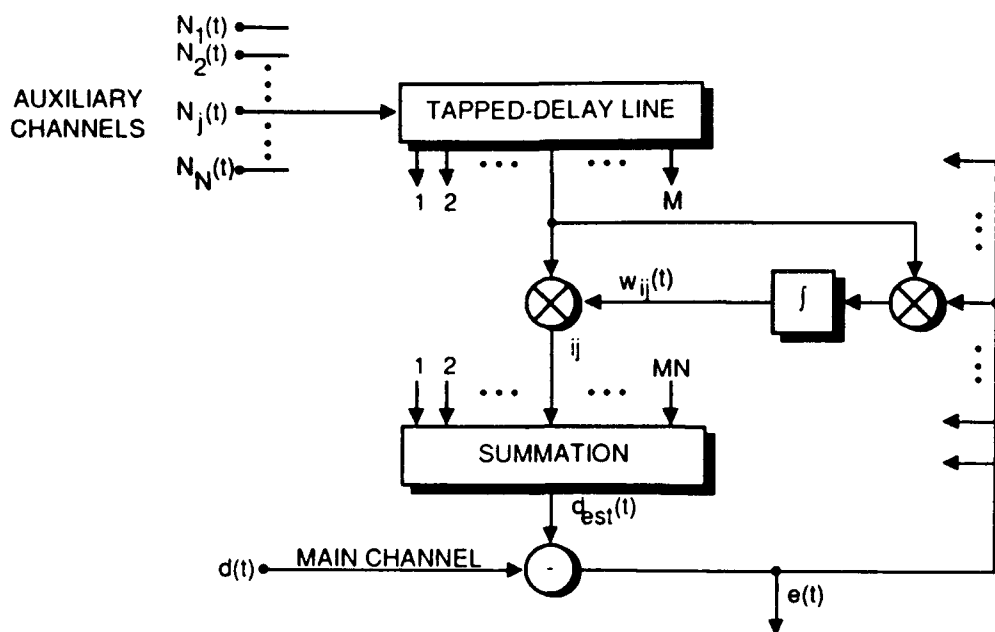
The standard multidimensional tapped delay line implementation of the least-mean-square (LMS) algorithm is shown in **Figure 3-1**. We note that the LMS algorithm is based on steepest descent techniques, where the weight function is updated in the direction opposite the gradient at the current weight value. This will cause the weights to move in such a way as to reduce the mean-squared-error (MSE) along the steepest gradient. The input signals from the auxiliary antennas, $N_i(t)$, are convolved with the weight functions $w_i(t;\tau)$, which are functions of time, t , and delay, τ , to yield an estimate, $d_{est}(t)$, of the main channel signal:

$$d_{est}(t) = \sum_{j=1}^P \int_{-\frac{T_a}{2}}^{\frac{T_a}{2}} w_j(t;\tau) N_j(t-\tau) d\tau \quad (3-1)$$

where P is the number of auxiliary antennas and T_a is the length of each tapped delay line. This estimate is subtracted from the main channel signal, $d(t)$, to form an error signal, $e(t)$. The weights are then updated according to the degree of correlation between this error and the auxiliary channel inputs. The i^{th} weight function is represented mathematically as:

$$w_i(t;\tau) = w_i(0;\tau) + \int_0^t \alpha(t) e(t) N_i^*(t-\tau) dt \quad (3-2)$$

where $\alpha(t)$ is a time-varying (in general) acceleration parameter. As this process continues in time, the adaptively changing weights converge to a steady-state solution (if the signal environment is stationary). This cancels the noise in the main channel, which equivalently yields the minimum MSE and maximum output SNR.



TR-91-PROP-1700

Figure 3-1. Classical Multichannel LMS Adaptive Filter

This classical LMS algorithm performs a weight update at each point in time. If a discrete algorithm is employed, the weight update is achieved at each time step, which must be at a frequency greater than twice the widest bandwidth to be processed. Thus, for 10 MHz bandwidth signals, the time step and weight update occur every 50 ns. **Figure 3-1** implies that taps must be positioned every 50 ns if discrete taps are employed. The integration shown in Equation 3-2 occurs over the entire observation period, resulting in a continuous weight update. In addition, as the weights are updated, the error continues to be reduced, which then feeds back into the weight calculation integration.

The algorithm being implemented by the MADOP differs from this classical LMS algorithm. The filter function given by Equation 3-1 is implemented in the classical form, but the weight update given in Equation 3-2 is implemented differently. For our system, the correlation between the error and the auxiliary antenna signals is performed over some window of time, T , during which the weight functions do not change. This window of time has typically been greater than 2 ms for the single channel system, and is ultimately limited to approximately 1 μ s due to linear detector array readout times and limited detector sensitivity. After this correlation has been obtained, the result is used to update the weight functions, a process that takes an additional increment of time, t_u . Thus, Equation 3-2 is modified to yield:

$$w_j [M (T + t_u) ; \tau] = w_j (0 ; \tau) + \sum_{j=1}^M \int_{j(T+t_u)}^{j(T+t_u)+T} \alpha_j e(t) N_j^* (t - \tau) dt \quad (3-3)$$

where M is the processing iteration step. If t_u , the weight update time, is not less than or equal to T , then during the time that the weights are being updated there is no consideration of the signal environment (no correlations are being integrated in Equation 3-3). The incremental changing of the weights and the loss of correlation information need to be further studied to determine the impact on system performance.

This windowed algorithm, as described in Equation 3-3, is similar to the "block" adaptive filtering approach, which has been increasingly researched in the digital adaptive filtering community (References 15 through 17). The primary motivation for this interest is the compatibility of block routines with fast convolution algorithms that employ fast Fourier transforms (FFT). In these adaptive filters, the weights are updated based on a window of data, rather than at each time step. This is characteristic of the MADOP algorithm. An interesting result related to these block routines is that the convergence generally proceeds much faster than for the classical LMS routine due to the reduction in the gradient estimate noise. Also, highly correlated input data (resulting in a high correlation matrix condition number and generally slow convergence) are better processed through block techniques.

Another algorithmic consideration is the need to develop complex weights based on complex correlation outputs. The emphasis to date in the MADOP program has been the generation of real weights. If the multipath summations described in Equation 2-2 are, in fact, strictly time delays with no phase shift imposed on the RF (and IF) carrier, and if there are no propagation or receiver-induced phase shifts, then the complex weighting scheme will not be required. For other situations, performance may be degraded if complex weights are not employed.

An additional algorithm is being considered that will provide a discrete number of taps based on the location of the correlation peaks arising in Equation 3-3 (Reference 18). Several issues must be addressed relating to this approach. First, the number of peaks arising in the correlation window grows very large in complex signal environments, as described at the end of Subsection 2.1.1. Also, for a single source with two multipaths, the number of correlation peaks in the cross-correlation will be four, and there remains the ambiguity as to which peak, or peaks, to choose. When single tones or combinations of single tones (a two-tone DSB-SC signal for example) are interference sources, there are a number of peaks because of the periodicity of the correlation. Also, a signal composed of the sum of sinusoids of the same frequency is still a sinusoid at that same frequency, with an amplitude and phase shift, so it is inappropriate to consider multipath with sinusoidal inputs. Note that this comment also applies to DSB-SC two-tone signals created by modulating a sinusoid onto a carrier.

3.2 SIMULATION ACTIVITIES

Three software simulations of the MADOP system, known as Optical Jammer Cancellers 1, 2, and 3 (OJC1, OJC2, OJC3), were developed to assess alternative weighting schemes. These simulations, developed using MATLAB software obtained from MathWorks, Inc., are provided in Appendix A of this report. The three simulations employ a pulse input signal immersed in white noise (band-limited in OJC3). The three simulations differ in their weight schemes as described below.

3.2.1 OJC1

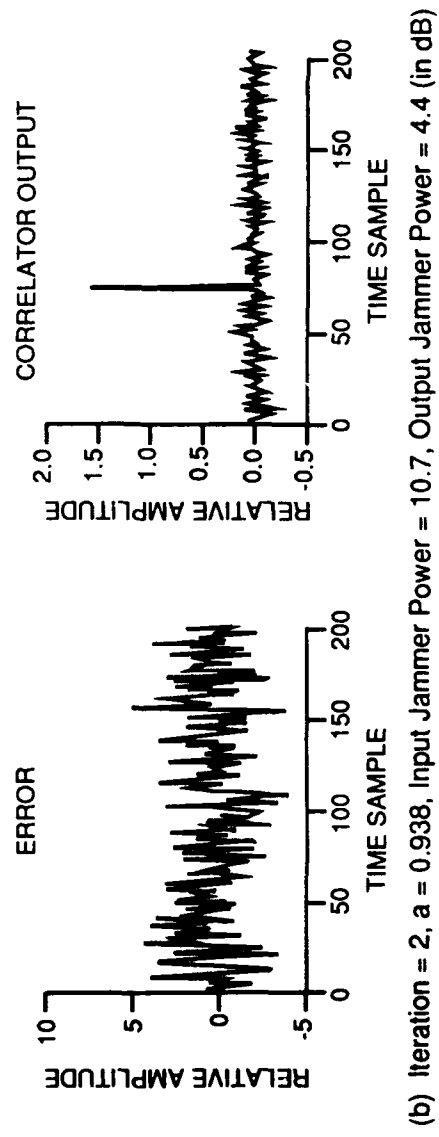
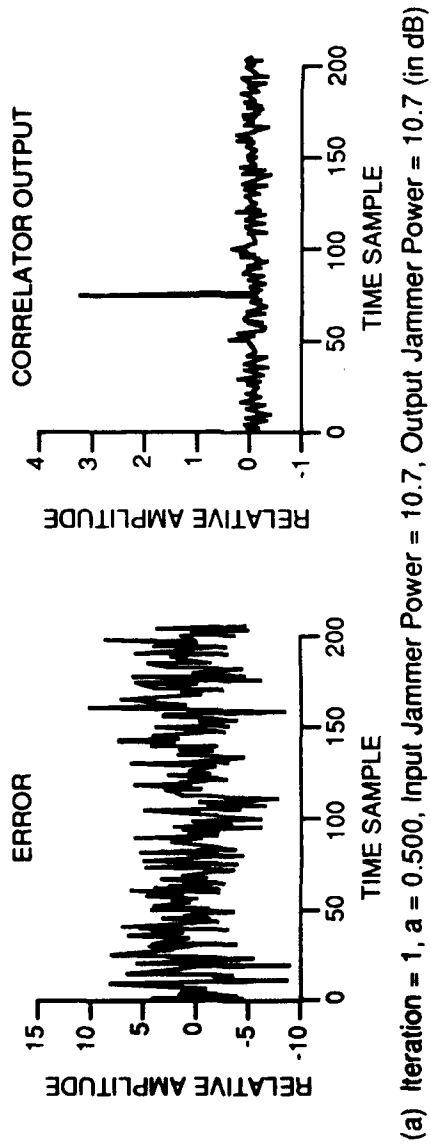
OJC1 demonstrates the capability to cancel wideband interference after several iterations using any of three weighting schemes, namely a thresholded weight vector update, a peak weight update selection, and a full weight vector update. The fully-commented code appears in Appendix A, where the "%" symbol denotes a comment in the software. Parameters used in the software are summarized in the Appendix in **Table A-1**, and a flowchart of the software for OJC1 is shown in **Figure A-1**. **Figure 3-2** was generated using the thresholded weight vector update scheme, which is not commented out in Appendix A.

The primary motivation for simulating the thresholded weight vector schemes is the desire to minimize the number of taps applied in the AOTDL, since this drives the complexity of the electronic interface for weight vector application. This is done in either of two ways. The thresholded weight vector update normalizes *delw* to the range [0, 1] and sets to zero any value greater than 0.1 (this value is easily changed to simulate other thresholds). The peak weight update scheme selects the largest unnormalized weight and sets all other weights to zero. In both cases, the weight update is added to the previous weight vector to generate the new weight vector, which is not further thresholded.

The acceleration parameter *a* was chosen on recommendations from Dr. Welstead. If the previous weight update vector *delwold* is zero, or if there is no change between *delwold* and the current weight update vector *delw*, then *a* = 0.5. If this is not the case, the previous value of *a* (*aold*) is changed using the equation

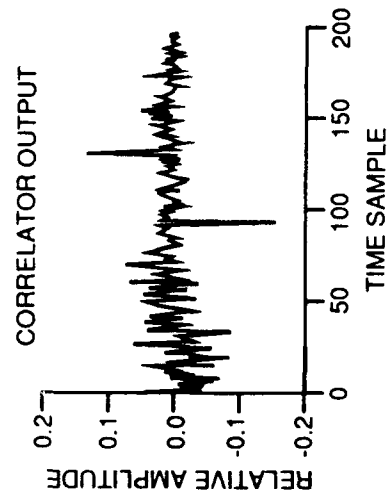
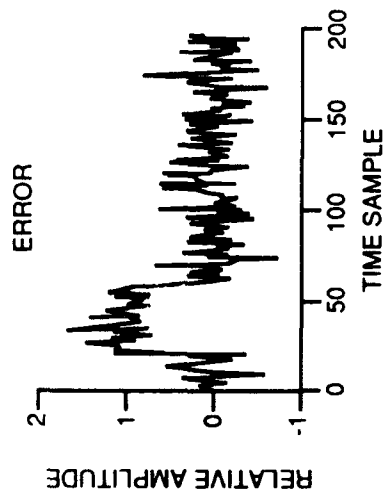
$$a = aold \frac{(\text{delwold}) * (\text{delwold})^T}{(\text{delwold}) * (\text{delwold} - \text{delw})^T} \quad (3-4)$$

where the superscript T denotes the transpose operation. Thus, the numerator and denominator are vector inner products. This equation states that for fast changing weight update vectors (large denominator), *a* is decreased and vice-versa. This helps maintain a fast rate of convergence while minimizing the possibility of unstable operation.

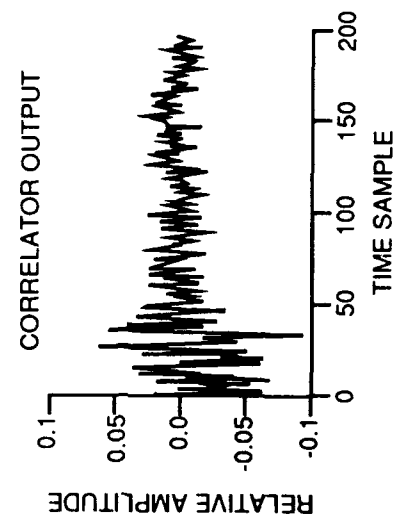
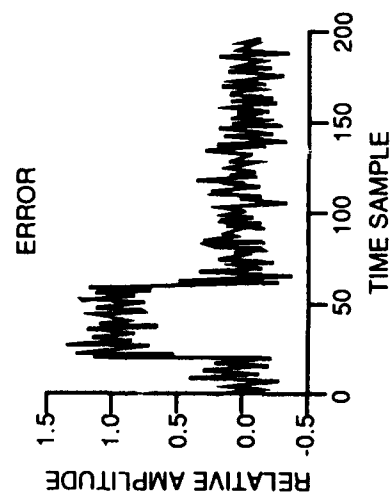


TR-92-S101-0405

Figure 3.2. OJCI Simulation Performance



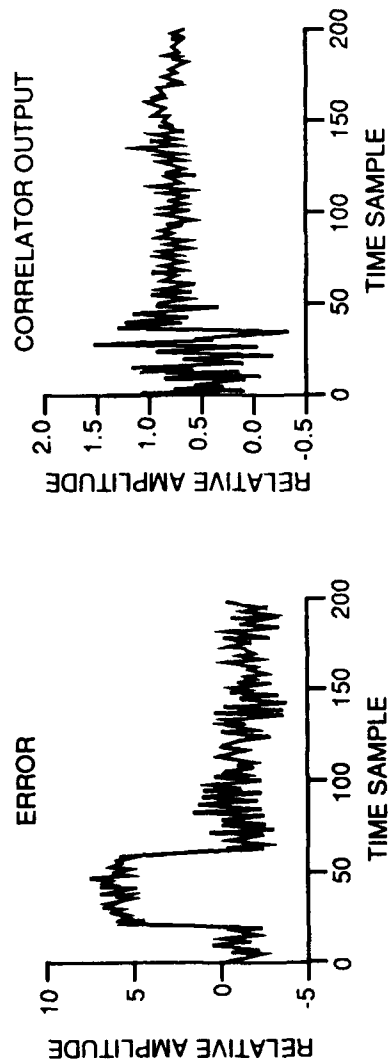
(c) Iteration = 3, $a = 0.986$, Input Jammer Power = 10.7, Output Jammer Power = -11.6 (in dB)



(d) Iteration = 4, $a = 0.973$, Input Jammer Power = 10.7, Output Jammer Power = -15.5 (in dB)

TR-92-SIO1-0405

Figure 3-2. OJCI Simulation Performance (Continued)



(e) Iteration = 5, $a = 0.761$, Input Jammer Power = 10.7, Output Jammer Power = -17.5 (in dB)
 TR-92-S001-0405

Figure 3-2. OJC1 Simulation Performance (Concluded)

The simulated signal environment has inherent simplifications that will be upgraded in future simulation developments. The spacing between time samples is $0.5 \mu\text{s}$ (20 MHz sampling rate) and the simulated signal environment is periodic with a period of $10 \mu\text{s}$ (200 samples). The uncorrupted received signal s is a $20\text{-}\mu\text{s}$ pulse (500 kHz bandwidth) and the jamming signal is a Gaussian-distributed zero-mean random vector having a bandwidth of 20 MHz (equal to the sampling rate). The sum of the received and jamming signals, with a known signal-to-jammer power ratio, represents the received main channel signal d . The auxiliary channel is equivalent to the jamming signal in the main channel but delayed by $1 \mu\text{s}$ and weighted by the auxiliary-to-main channel voltage ratio AM ($AM = 1$ in OJC1 but can easily be changed). In the current simulation the signal and jammer representation are constant during the adaptive cancellation algorithm and thus represent a very idealized situation. This will be changed to a more realistic signal and jammer representation in future studies.

The function $\text{filter}(b, a, x)$ filters a vector x with the tapped delay line filter described by the difference equation

$$y[n] = b(1)x[n] + b(2)x[n-1] + \dots + b(n_b+1)x[n-n_b] \\ - a(2)y[n-1] - \dots - a(n_a+1)y[n-n_a] \quad (3-5)$$

where b is a vector of length n_b corresponding to the weight vector in our analysis, and the coefficients a are all set to zero except $a(1) = 1$ (the filter is nonrecursive in our analysis). In the z-transform frequency domain this function is expressed as

$$Y(z) = \frac{b(1) + b(2)z^{-1} + \dots + b(n_b+1)z^{-n_b}}{1 + a(2)z^{-1} + \dots + a(n_a+1)z^{-n_a}} X(z). \quad (3-6)$$

Therefore, in OJC1, the auxiliary channel jammer signal na is filtered by the finite impulse response (FIR) filter having weights w using the equation

$$y = \text{filter}(w, 1, na). \quad (3-7)$$

The function $\text{xcorr}(x, y, \text{"biased"})$ forms the biased estimate of the cross-correlation of the vectors x and y given by

$$C(m) = \frac{1}{N} \sum_{n=0}^{n-|m|-1} x(n)y^*(n+m). \quad (3-8)$$

The plots shown in **Figure 3-2** demonstrate clearly the effectiveness of the OJC1 algorithm for this signal environment. After five iterations, the jammer power in the main channel has been reduced from

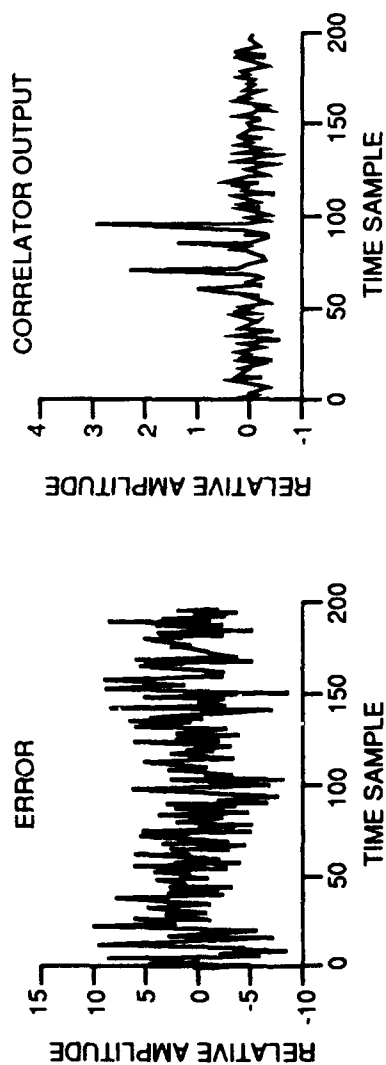
10.7 dB to -17.5 dB, an improvement of 28.2 dB, as shown in **Figure 3-2 (e)**. The pulse, which is initially immersed in the noise, is clearly visible in the error output (the best filtered version of s). Note also that the acceleration parameter a increases as the noise is suppressed, allowing for faster convergence while maintaining stability.

3.2.2 OJC2

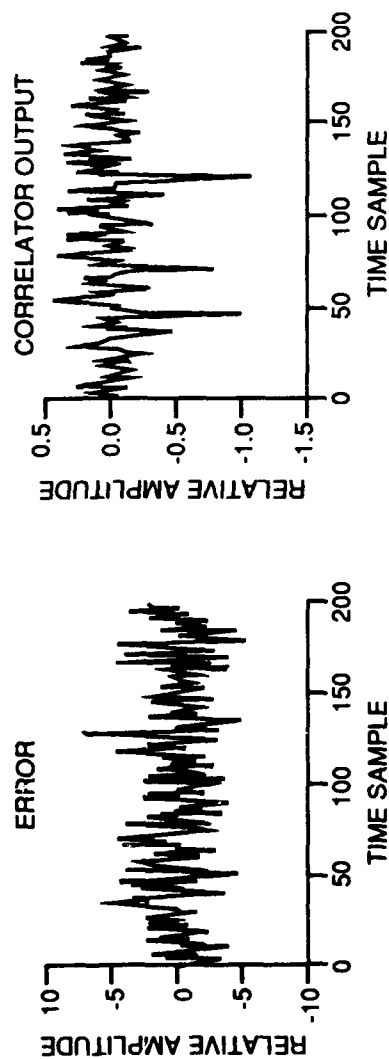
The routine OJC2 is similar to OJC1 with the addition of a multipath replica of the jammer. The main channel receives two replicas of the jammer separated by 10 samples ($0.5\ \mu\text{s}$) in addition to the pulse s . The auxiliary channel contains the same two replicas but this time separated by 25 samples ($1.25\ \mu\text{s}$). Because the multipath environment is more severe for this case, this single auxiliary channel system does not cancel this multipath jamming signal adequately, as is clearly evident in **Figure 3-3**. Even after 11 iterations, the noise still dominates the s signal.

3.2.3 OJC3

The routine OJC3 is similar to OJC1 except that the jamming signal is now passed through a 2-MHz, 5-pole Butterworth filter. Also, for the results shown in **Figure 3-4**, the entire weight update vector was employed, as shown by the use of comments in the OJC3 code in Appendix A. It is observed once again that the system effectively cancels the jammer as shown after five iterations in **Figure 3-4 e**. For this bandlimited noise case, the improvement in jammer power in the main channel is 18.8 dB.



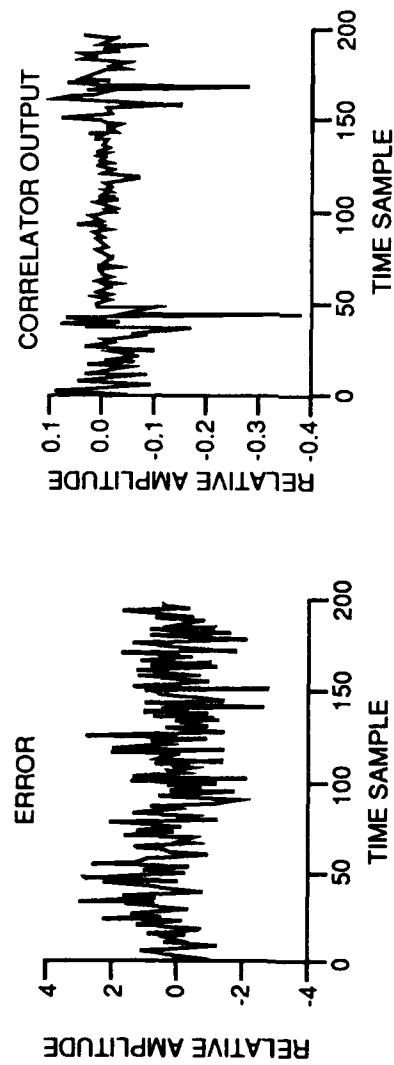
(a) Iteration = 1, $a = 0.500$



(b) Iteration = 2, $a = 0.406$

TR-92-S101-0406

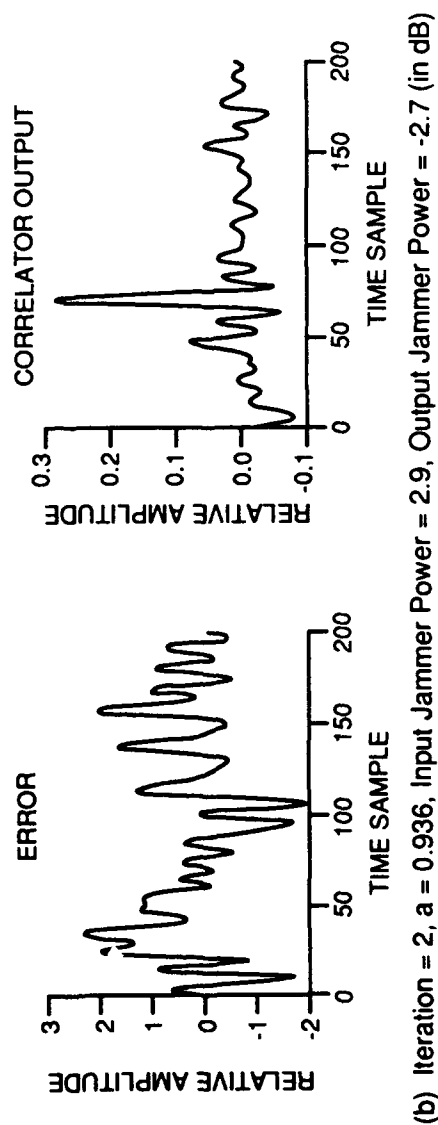
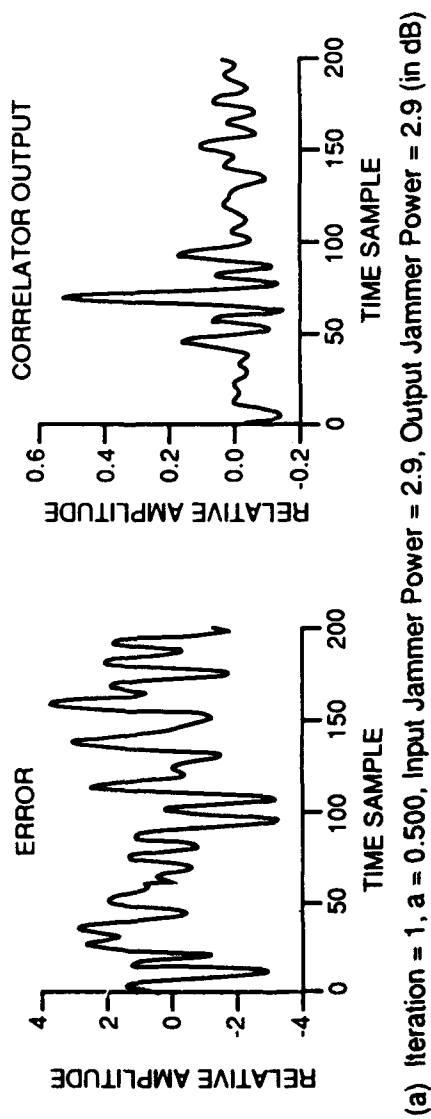
Figure 3-3. OJC2 Simulation Performance



(c) Iteration = 11, $a = 0.678$

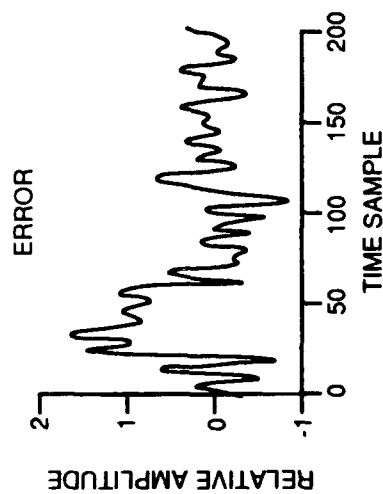
TR-92-S101-0406

Figure 3-3. OJC2 Simulation Performance (Concluded)

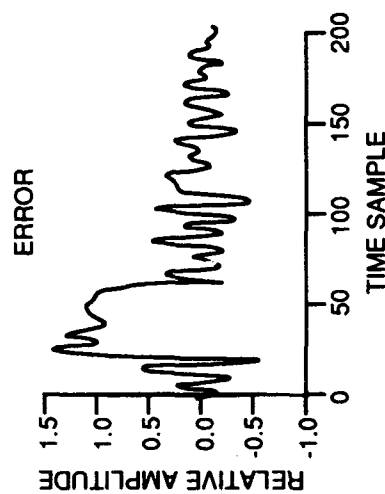


TR-92-S101-0407

Figure 3-4. OJC3 Simulation Performance



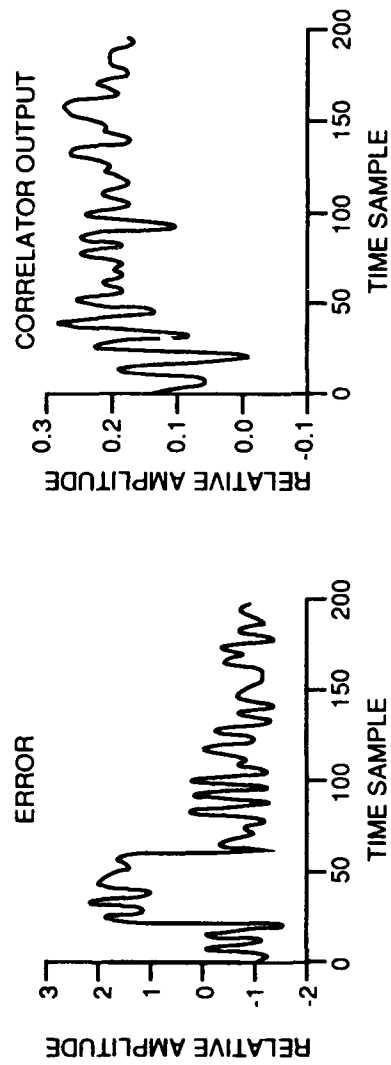
(c) Iteration = 3, $a = 1.166$, Input Jammer Power = 2.9, Output Jammer Power = -10.4 (in dB)



(d) Iteration = 4, $a = 1.646$, Input Jammer Power = 2.9, Output Jammer Power = -14.3 (in dB)

TR-92-SI01-0407

Figure 3-4. OJC3 Simulation Performance (Continued)



(e) Iteration = 5, $a = 1.818$, Input Jammer Power = 2.9, Output Jammer Power = -15.9 (in dB)

TR-92-SI01-0407

Figure 3-4. OJC3 Simulation Performance (Concluded)

4. MULTICHANNEL ADAPTIVE OPTICAL PROCESSOR DESIGN AND IMPLEMENTATION

The use of AO signal processing techniques for adaptive filtering has been studied by others. For example, time-domain implementations employing optical integrators such as liquid crystal light valves (LCLV) and photorefractive crystals have been demonstrated (References 8, 9, 10, and 11). An architecture not requiring an integrating device was proposed in Reference 12. VanderLugt has developed an equivalent frequency-domain architecture that also does not require an optical integrator (Reference 13). An excellent review and performance comparison of several of these architectures is provided in Reference 14.

As described in Subsection 3.1, the MADOP architecture implements the block LMS algorithm as opposed to the classical LMS approach. This is achieved through the integration of the weight update correlation information (over a finite block of data) on a charge coupled device (CCD) detector array. This result is then used to update the adaptive weight vector that is applied to the AOTDL filter to generate the desired main channel estimate. This architecture is also being implemented using multichannel AO cells and parallel processing of multiple auxiliary channel inputs. This multichannel processor is the first such architecture reported.

Specific accomplishments made on the optical implementations of the time-integrating correlators for weight update calculation include:

1. Modification of an existing single-channel, in-line, time-integrating correlator (Reference 1) to accommodate coherent processing at the system IF;
2. Performance characterization of the modified in-line architecture using laboratory-generated test waveforms;
3. Design and development of a two-channel, two-path Mach-Zehnder time-integrating correlator;
4. Performance characterization of the two-path architecture using laboratory-generated test waveforms;
5. Comparison of the Mach-Zehnder two-path architecture to the in-line architecture; and
6. Definition of post-detection operations for the interface between the weight update calculation and the tapped delay line filter, and verification of initial post-detection processing routines developed by 1LT Andrews.

Specific accomplishments made on the optical implementations of the AO tapped delay line filter include:

1. Design and mathematical description of a coherent AOTDL architecture employing a Mach-Zehnder interferometer, a modification of a prior baseband AOTDL architecture (Reference 1);
2. Fabrication of a single-channel version of this system;
3. Test and analysis of the coherent architecture that employs a Mach-Zehnder interferometer to provide an output signal at the desired IF without the effects of the frequency shift induced by the AOSLM;
4. Development of a coherent noninterferometric architecture with an electronic reference that overcomes the true time delay shortcomings of the Mach-Zehnder architecture;
5. Fabrication of a two-channel version of this processor at 80 MHz center frequency, and
6. Initial performance characterization of this architecture using laboratory-generated test waveforms.

4.1 OVERALL SYSTEM ARCHITECTURE

The design and implementation of these AO subsystems is the subject of this section. First the overall system will be described, followed by the theory, design, and test results for the AO time-integrating correlators and the AO tapped delay line filter architectures.

The adaptive IF canceller shown in *Figure 2-2* accepts the main channel signal and auxiliary channel inputs, and outputs the filtered main channel signal to the radar signal processor. The MADOP implementation of the adaptive IF canceller employing two auxiliary channels is shown in *Figure 4-1*. The AO time-integrating correlator accepts the two auxiliary-channel inputs and correlates these against the error signal (the filtered main-channel signal). The two finite-time correlations that result represent the weight update information and are input into a personal computer (PC) to generate the adaptive weight vectors. These two sets of weights are then applied to the AO tapped delay line architecture to filter each of the auxiliary channel inputs to arrive at a multichannel estimate of the noise in the main channel (assuming low SNR in the main channel and therefore no target-return signal information in the auxiliary channel inputs). This noise estimate is subtracted from the main channel signal to form the error signal to be input into the time-integrating correlator, thereby closing the loop.

Potential signal and interference sources for testing and characterizing the MADOP in a laboratory environment are shown in *Figure 4-2*. The Lecroy 9100 Arbitrary Function Generator (AFG) can be used to generate baseband waveforms such as tones, linear frequency modulation (LFM), and noise-like modulations, for interference source simulation. These baseband signals can then be mixed up to the 80-MHz IF using DSB-SC modulation. Another option is to employ a noise generator that outputs a waveform at each 80 MHz IF, thus requiring no mixing. The signal source can be provided using the Hewlett

Packard (HP) Frequency Agile Signal Simulator (FASS) or the General Electric (GE) Radar Signal Simulator (RSS), both of which are available in the Photonics Center. Another possibility is to generate a third uncorrelated interference source using the options shown in *Figure 4-2 (a)* and call this third source the signal.

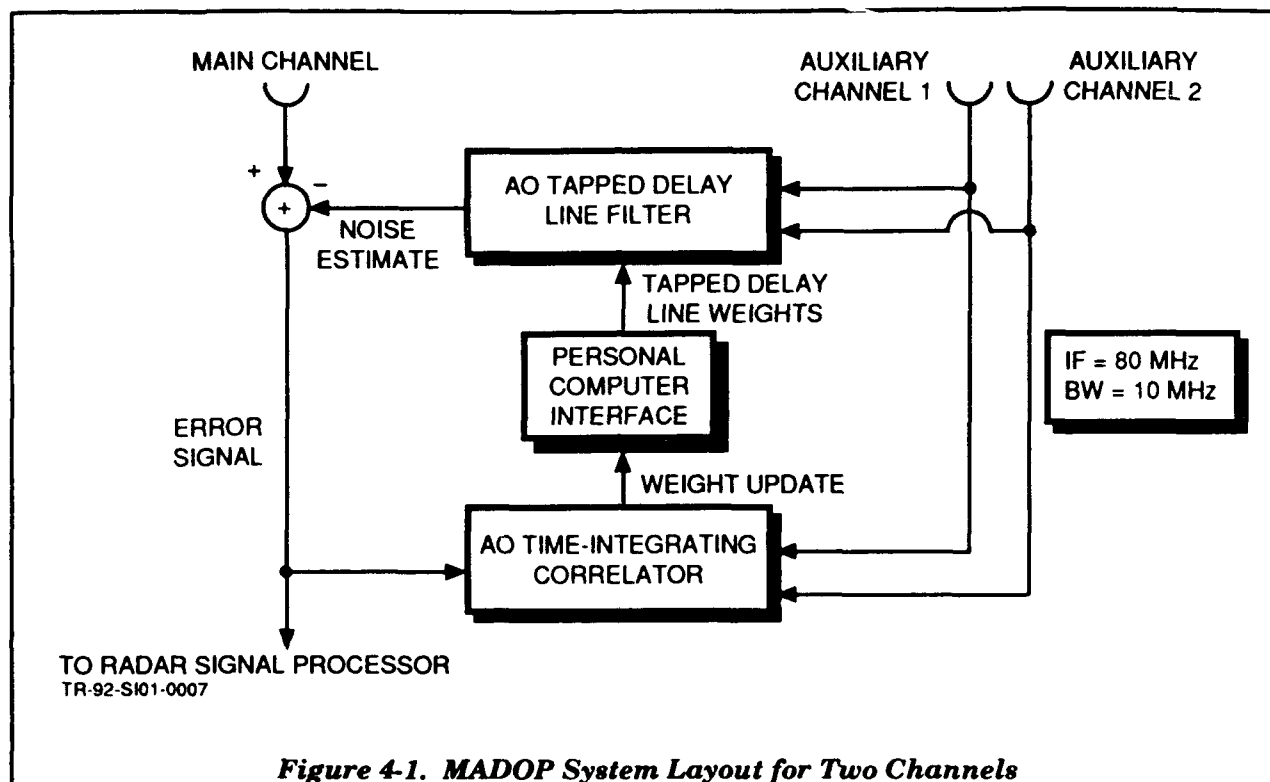


Figure 4-1. MADOP System Layout for Two Channels

The electronic interfaces between the two AO subsystems are shown in *Figure 4-3*. Referring to *Figure 4-3 (a)*, the outputs from the AO time-integrating correlator are centered at the carrier frequency of the correlation information after detector readout. A Girard 3197 interface board then digitizes the data with 8-bit resolution and stores the digital data in memory for further digital processing. The weights are updated in the PC and provide the AOTDL filter weights. In the future, the PC will provide automatic gain control (AGC) to the error signal to maintain strong correlation results as the error is adaptively reduced.

The error generation interface is shown in *Figure 4-3 (b)*. The photodiode output is at a center frequency equal to the system IF minus the electronic reference frequency, which is approximately 15 MHz (see Subsection 4.3.2 for details on the electronic reference). After amplification this signal is mixed back up to the 80-MHz IF, bandpass filtered, and subtracted from the main channel signal. This error signal then drives the time-integrating correlator, which amplifies and, in the future, performs AGC for matching signal levels in the correlator system.

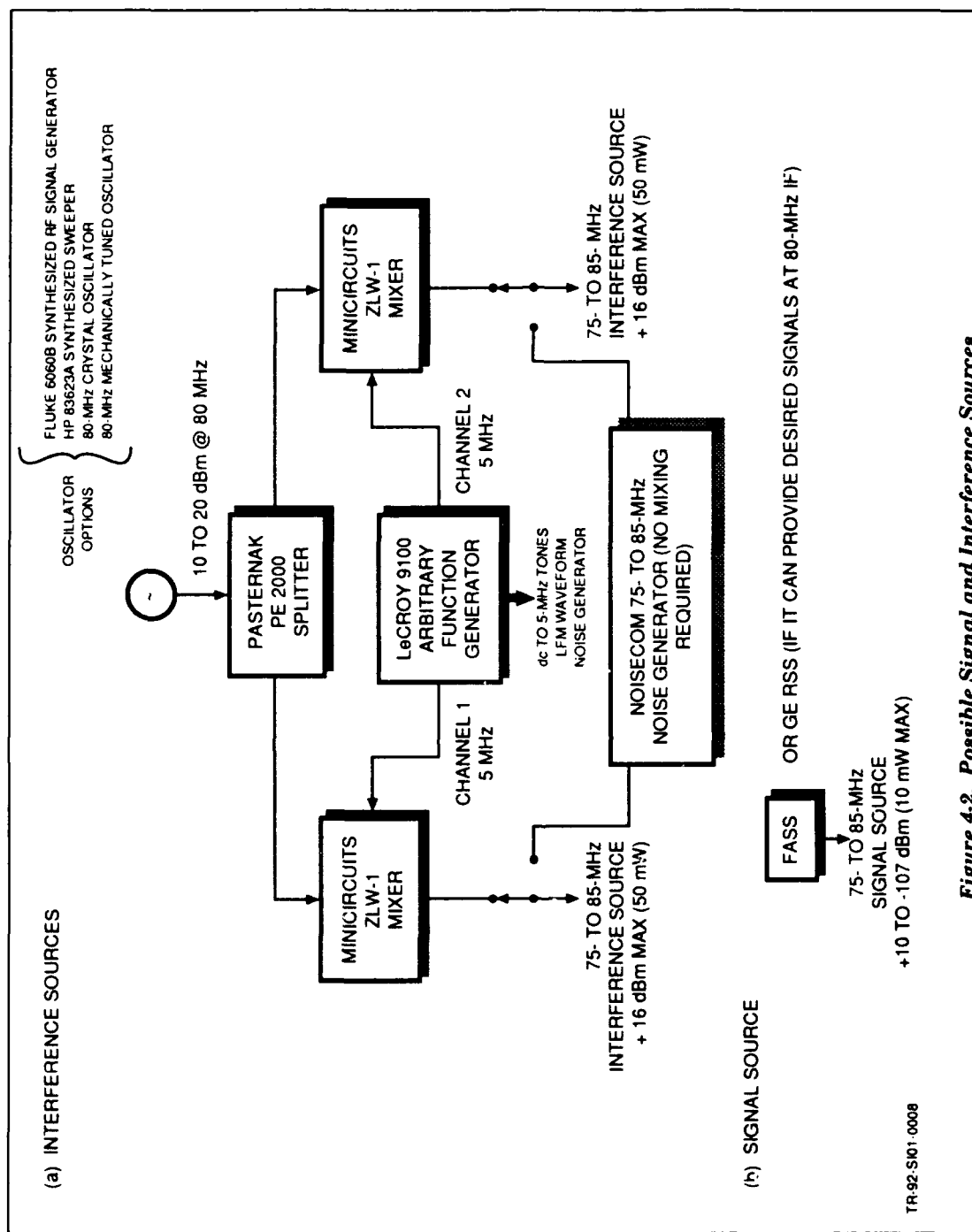
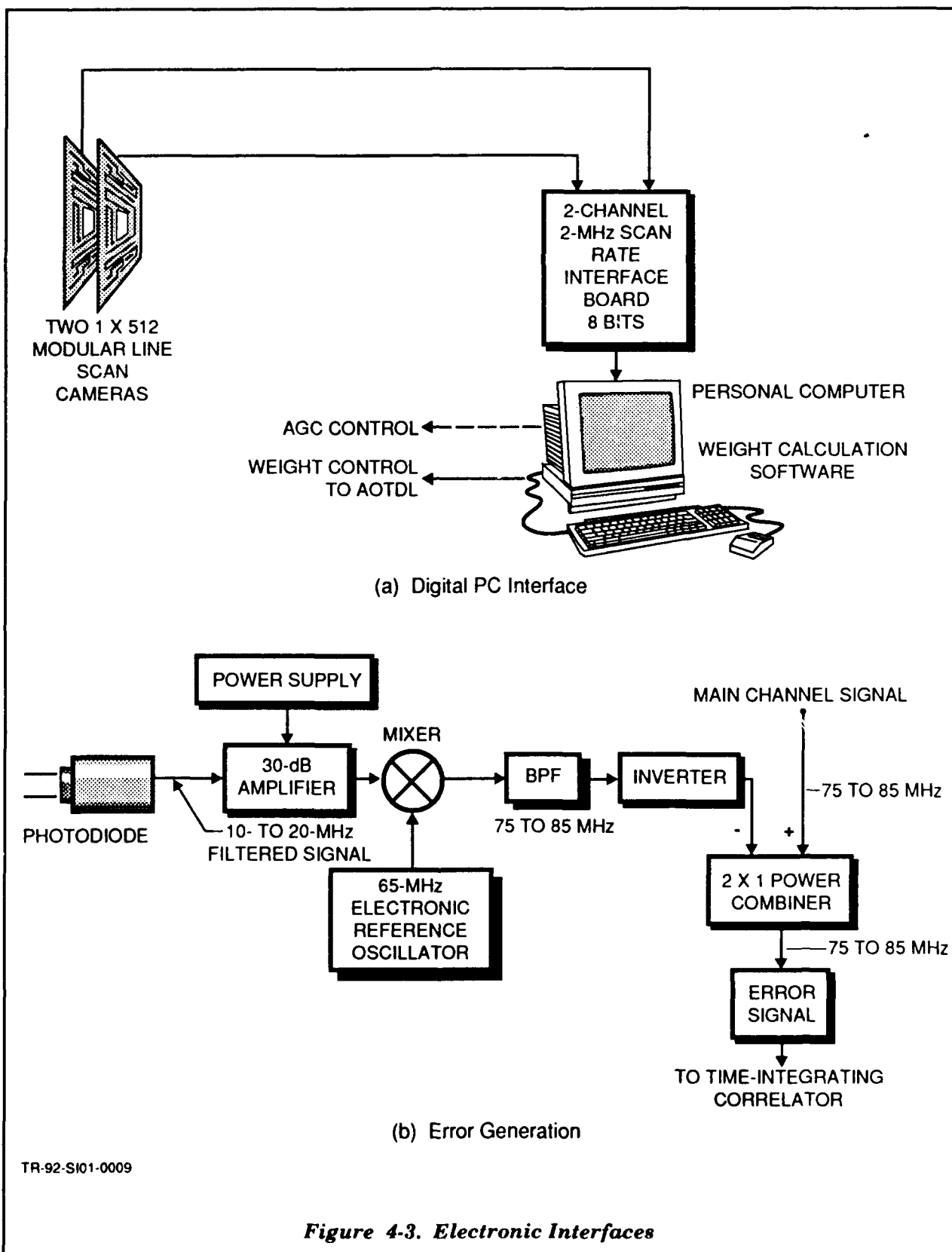


Figure 4-2. Possible Signal and Interference Sources



4.2 TIME-INTEGRATING CORRELATION FOR WEIGHT FUNCTION CALCULATION

As mentioned previously, the time-integrating correlator portion of the MADOP is used for the calculation of the weight function and generation of the inputs to the AOTDL filter. We consider the error signal, $e(t)$, and auxiliary antenna input, $N(t)$, given at baseband as the complex modulations

$$e(t) = A_e(t) \exp[j\phi_e(t)] \quad (4-1)$$

and

$$N(t) = A_N(t) \exp[j\phi_N(t)]. \quad (4-2)$$

The coherent (magnitude and phase) correlation, as described in Equation 3-2 with α incorporated in $e(t)$, is given by:

$$R(\tau) = \int_0^T A_e(t) \exp[j\phi_e(t)] A_N(t-\tau) \exp[-j\phi_N(t-\tau)] dt = A_R(\tau) \exp[j\phi_R(\tau)] \quad (4-3)$$

where $A_R(\tau)$ and $\phi_R(\tau)$ are the correlation magnitude and phase, and T is the total integration time. This integral can be realized on the CCD array (all values are positive and real) by modulating $R(\tau)$ onto a spatial carrier, f_τ , and adding a bias. Thus, the desired correlation output is

$$\begin{aligned} R(\tau) &= \text{bias} + \text{Re} \left\{ \exp[j2\pi f_\tau \tau] \int_0^T e(t) N^*(t-\tau) dt \right\} \\ &= \text{bias} + A_R(\tau) \cos[2\pi f_\tau \tau + \phi_R(\tau)] \end{aligned} \quad (4-4)$$

which can be coherently demodulated to obtain the magnitude and phase of the correlation. In the following subsections, techniques for achieving this coherent correlation operation in a multichannel configuration will be described. In addition, the design, testing, and initial performance evaluations of the different time-integrating correlator architectures will be presented.

4.2.1 Design Alternative I: In-Line Multichannel Correlator Architecture

Figure 4-4 illustrates the conceptual in-line correlator architecture for a two-channel configuration. The actual optical layout is depicted later in **Figure 4-7(a)**. A modulated laser diode is used as the optical source for this architecture. Also shown in the figure is a diagram of the spectral inputs to the laser diode and multichannel AO cell for coherent operation. As shown in the figure, beam conditioning and replicating optics are used in conjunction with the laser diode to illuminate separate channels of the

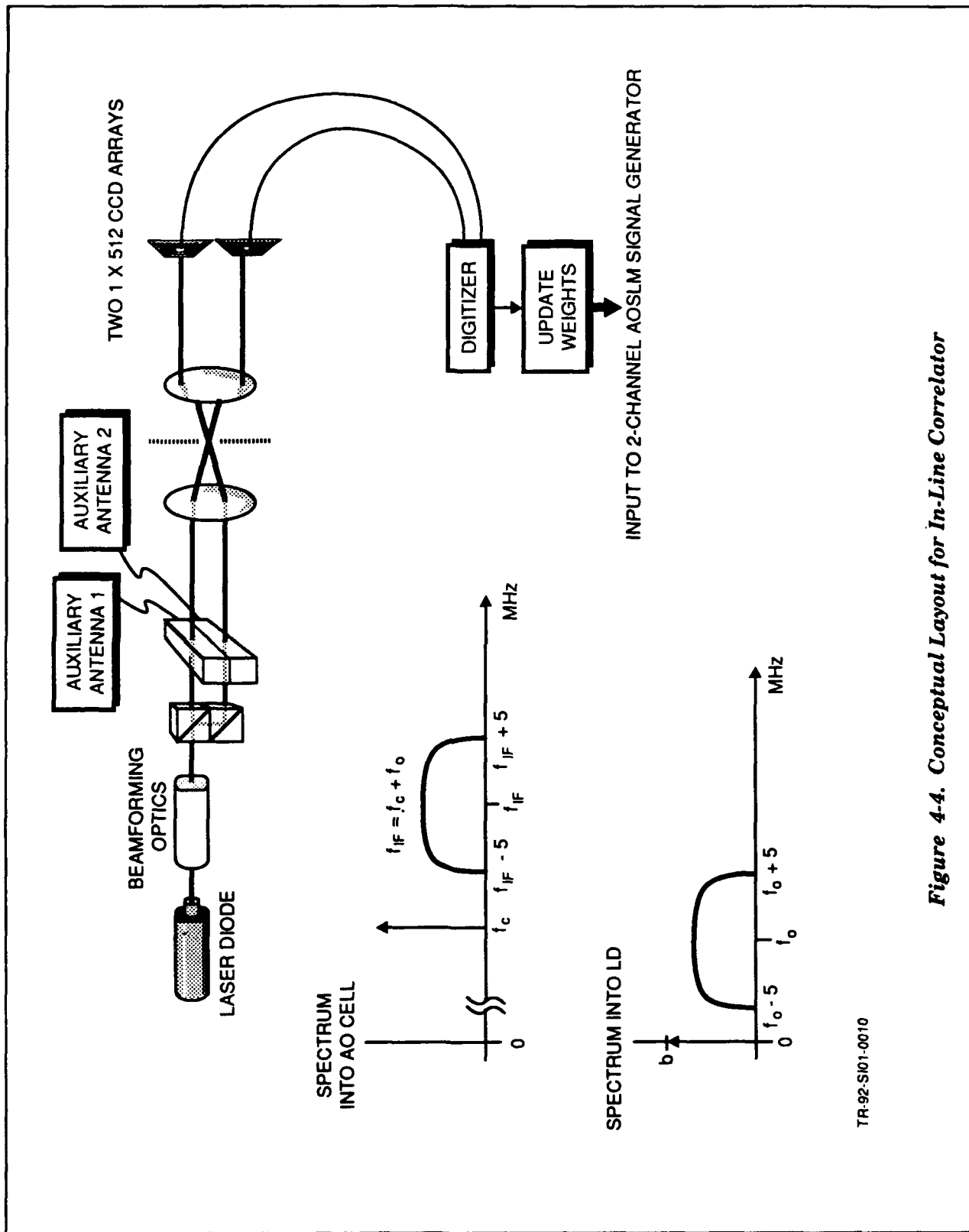


Figure 4-4. Conceptual Layout for In-Line Correlator

multichannel AO cell. The diffracted signals from the AO channels are schlieren imaged onto separate CCD arrays where they are time integrated and read-out to calculate the weight updates. Schlieren imaging is used to view, or image, an object whose characteristics of interest are spatial phase variations. Schlieren imaging is accomplished here by using a spatial filter in the Fourier plane of the AO cell of interest. An example of a schlieren image is shown in **Figure 4-5**. This figure shows the schlieren image of the Newport Electro-Optical Systems (NEOS) multichannel AO cell with an RF signal applied to four adjacent channels. Through this imaging technique, AO cell acoustic apertures can be analyzed and characterized to assess such acoustic column properties as spreading, crosstalk, and time aperture.

Coherent operation is achieved with the in-line architecture by adding a reference oscillator to the AO cell input to create a reference beam to spatially and temporally interfere with the information beam. The interference between the reference beam and the information beam at a relative angle will create the spatial fringe pattern described above. In addition, due to the different Doppler shifts induced by the AO cell, the fringe pattern will oscillate at the difference frequency between the reference frequency and the information frequency. Modulation of the laser diode cancels this beat frequency in order to freeze the fringe pattern and allow for time integration. The undiffracted beam can be used to interfere with the information beam, but the resulting spatial carrier frequency will be prohibitively high, requiring a very long detector array to adequately sample the carrier. Using the reference oscillator allows the user to set the output carrier at the desired frequency. The condition on this carrier is that the reference oscillator be at least 1.5 times the bandwidth away from the information center frequency. Thus, for an 80-MHz center and a 10-MHz bandwidth, the reference oscillator must be at a frequency of 65 MHz or less (or greater than 95 MHz). For this numerical example, with a 65-MHz reference oscillator resulting in a 15-MHz oscillator offset, the laser diode must be driven with the 10-MHz bandwidth signal on a 15-MHz carrier.

Mathematically, these operations are summarized as follows. The laser diode intensity modulation is given by:

$$I_1(t) = A_1 [1 + m_1 \operatorname{Re} \{ A_e(t) \exp[j\phi_e(t)] \exp[j2\pi f_0 t] \}], \quad (4-5)$$

where m_1 is the modulation depth. Each channel of the AO cell is amplitude modulated to provide the spatial and temporal signal:

$$\begin{aligned} A_2(t - \tau) = & \sqrt{A_2} \{ 1 + m_2 A_N(t - \tau) \exp[-j\phi_N(t - \tau)] \exp[-j2\pi f_0(t - \tau)] \} \\ & \cdot \exp[-j2\pi f_c(t - \tau)] \end{aligned} \quad (4-6)$$

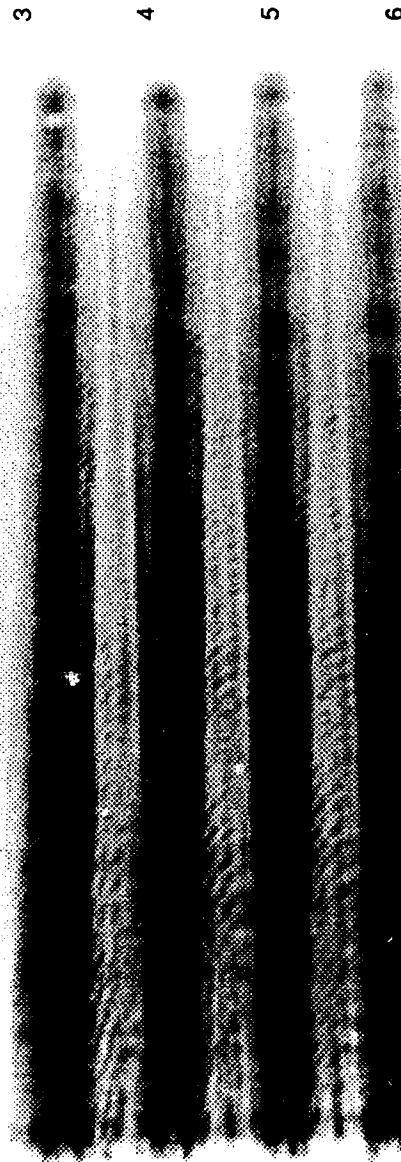
where m_2 is the ratio of signal amplitude to reference oscillator amplitude. Taking the squared magnitude of this amplitude and multiplying by the laser intensity modulation given above provides the detected intensity for the i^{th} correlation,

NEOS MULTICHANNEL AO CELL
N43080-8-BD

8 CHANNELS, BW = 40 MHz, $f_c = 80$ MHz, $\tau = 5 \mu s$

$f = 60$ MHz INTO CHANNELS 3, 4, 5, AND 6

TRANSDUCER



TR-92 S101-0430A

Figure 4-5. Schlieren Image of NEOS AO Cell

$$\begin{aligned}
I_d(t; \tau) = & A_1 A_2 (1 + m_2^2 |A_N(t - \tau) \exp[-j\phi_N(t - \tau)]|^2) \\
& + A_1 A_2 m_1 (1 + m_2^2 |A_N(t - \tau) \exp[-j\phi_N(t - \tau)]|^2) \\
& \bullet \operatorname{Re} \{ A_e(t) \exp[j\phi_e(t)] \exp[j2\pi f_0 t] \} \\
& + A_1 A_2 2m_2 \operatorname{Re} \{ A_N(t - \tau) \exp[-j\phi_N(t - \tau)] \exp[-j2\pi f_0(t - \tau)] \} \\
& + A_1 A_2 m_1 m_2 \operatorname{Re} \{ A_e(t) \exp[j\phi_e(t)] \\
& \bullet A_N(t - \tau) \exp[-j\phi_N(t - \tau)] \exp[j2\pi f_0 \tau] \} \\
& + A_1 A_2 m_1 m_2 \operatorname{Re} \{ A_e(t) \exp[j\phi_e(t)] A_N(t - \tau) \\
& \bullet \exp[j\phi_N(t - \tau)] \exp[j2\pi(2f_0 t - f_0 \tau)] \} .
\end{aligned} \tag{4-7}$$

The second, third, and fifth terms shown have a temporal modulation at frequency f_0 and will integrate to zero over typical detector integration times. The first term is low frequency in both space and time relative to the desired term, which simply results in an intensity bias. The fourth term in this equation is the desired term relative to the desired term, which when integrated over time yields the carrier-modulated correlation given previously in Equations 4-3 and 4-4. After detector readout, but before digitization, it is desirable to employ a band-pass filter (BPF) to eliminate both the low-frequency bias and the high-frequency clock noise.

The detector sampling requirement is calculated according to standard Nyquist sampling theory. First consider the imaging of the 5- μ s correlation window across the linear array. The highest temporal frequency (encoded spatially) for the numerical example above is 20 MHz (15-MHz center frequency with a 10-MHz bandwidth). One cycle at this frequency corresponds to 50 ns, which implies a required pixel spacing of 25 nsec. Using this spacing over a 5- μ s window requires a total of 200 pixels. Thus, the Nyquist sampling requirement will be satisfied with a standard 512-pixel array. If the carrier frequency is increased to greater than 15 MHz (by using a reference oscillator of less than 65 MHz), more than 200 pixels will be required. This shows why the use of the undiffracted beam as a reference oscillator is impractical (the reference oscillator offset is 80 MHz requiring more than 800 pixels).

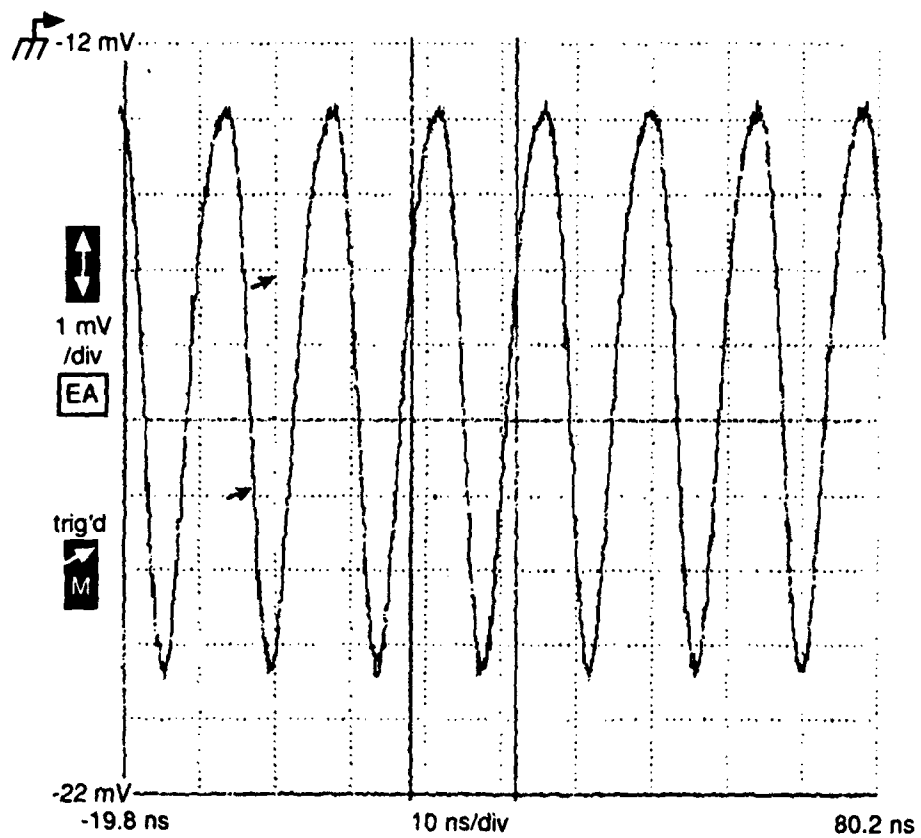
Tests were performed to determine the dynamic range of the laser diode to be used in the in-line correlator initial breadboard. A DO Industries GALA laser system (model 067-02-04, 670 nm, 5 mW maximum power) was chosen as the laser diode. A high-speed photodiode (Antel Corporation) was used to detect the temporal modulation of the laser diode. The output of the photodiode was observed on a

Tektronix 11403 digitizing oscilloscope. The dynamic range was calculated in the following manner. A sinusoid was input to the laser diode. The signal power was set to correspond to the maximum output of the laser diode. After photodiode detection, the input signal to the laser diode was attenuated and the corresponding results observed on the oscilloscope. The amount of attenuation that still resulted in the detection of the modulated waveform was used as an indication of the dynamic range. For the test, a 70 MHz sinusoid was input into the laser diode. After phone conversations with DO Industries, it was determined that an upper limit on input signal voltage is $15 V_{pp}$. It was decided to use a $10 V_{pp}$ input signal to the laser diode, which provides a 90% modulation of the optical beam. **Figure 4-6 (a)** illustrates the oscilloscope trace for the $10 V_{pp}$ input signal after photodiode detection. After 46 dB of electrical attenuation, a 70 MHz sinusoid was still visible on the oscilloscope, as shown in **Figure 4-6 (b)**. As noted in the figure, the detected attenuated signal is very noisy, possibly due to detector noise. As a result of the tests, it was determined that the dynamic range of the laser diode was on the order of 46 dB. This will be adequate for the MADOP demonstration program.

A single-channel, in-line correlator was designed, constructed, and tested at the Photonics Center with laboratory-generated signals. As mentioned previously, an extension of this design to a multichannel, in-line correlator would require a multichannel AO cell and additional beam replication optics. A conceptual system layout for multichannel operation was shown in **Figure 4-4**. A more detailed layout of the single-channel, in-line correlator design is illustrated in **Figure 4-7 (a)**. The combination of the 45° prism line generator and plano-cylindrical lens CY1 results in a collimated laser line used to illuminate the AO cell. Spherical lenses S1 and S2 are used to image the AO cell onto a linear CCD array. Note that the CCD array and the AO cell used in this setup could be replaced by the multichannel AO cell and the two-channel line-scan camera system described in Subsection 4.1. The AO material for this IntraAction AOD-70 device was flint glass ($n=1.68$ @ 670 nm, thickness ~ 60 mm). The optical path-length due to the index of refraction and thickness of the AO cell was taken into consideration when setting up the imaging system consisting of S1 and S2. During setup, it was assumed that the acoustic column object was located at the center of the crystal.

Figure 4-7 (b) illustrates the design of the electronics used to generate the input signals to the laser diode and to the AO cell. Note that the dc bias term for the laser diode input is generated internal to the GALA laser system. Also, the electronics design shown in the figure is configured for realizing an autocorrelation. Thus, $s(t)$ represents the temporal signal to be autocorrelated. As shown in the figure, the offset frequency, f_0 , was chosen to be 10 MHz. The requirement on the tone separation depends on the bandwidth of information being input to the correlator and is given by:

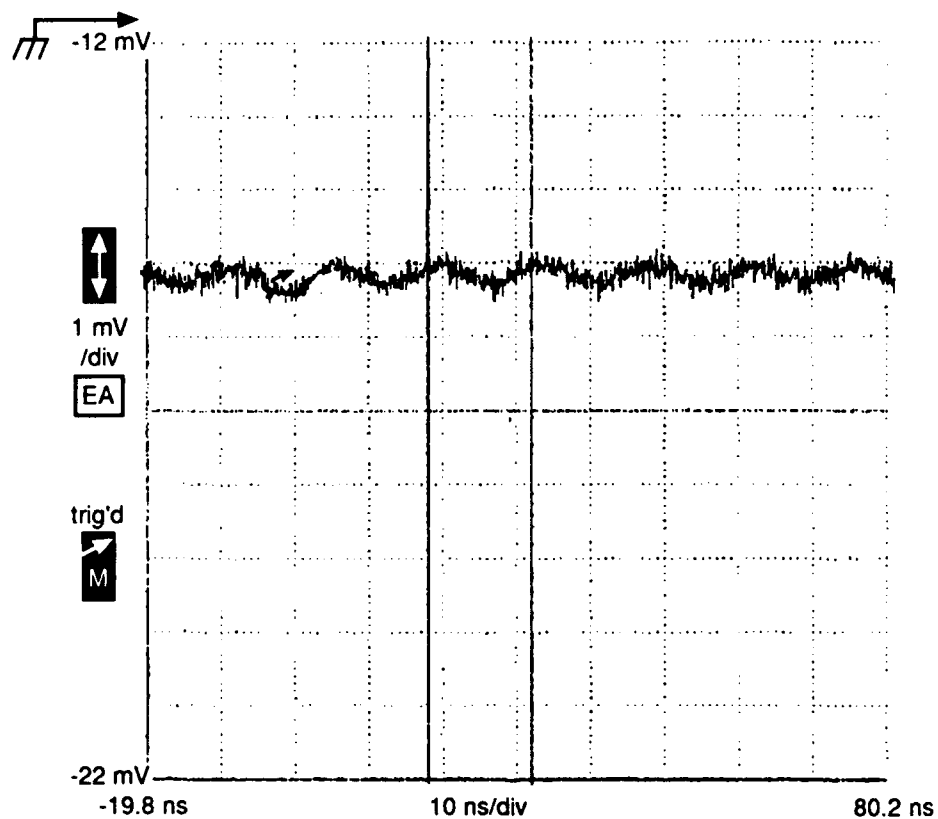
$$f_0 \geq 1.5B \quad (4-8)$$



(a) $s(t) = 70 \text{ MHz Sinusoid, } 10 \text{ V}_{pp}$

TR-92-SI01-0408

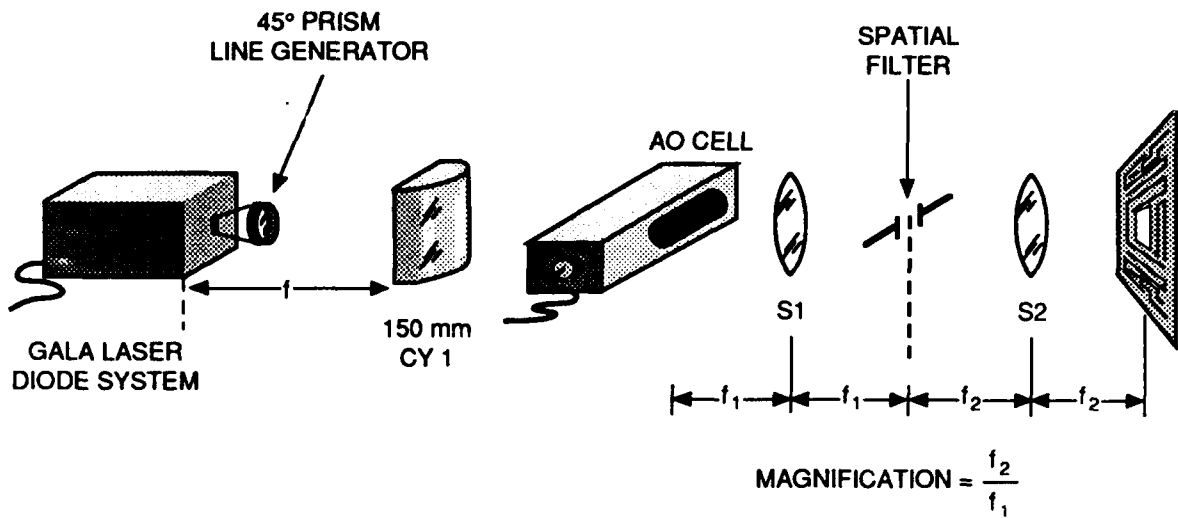
Figure 4-6. Laser Diode Dynamic Range Measurements



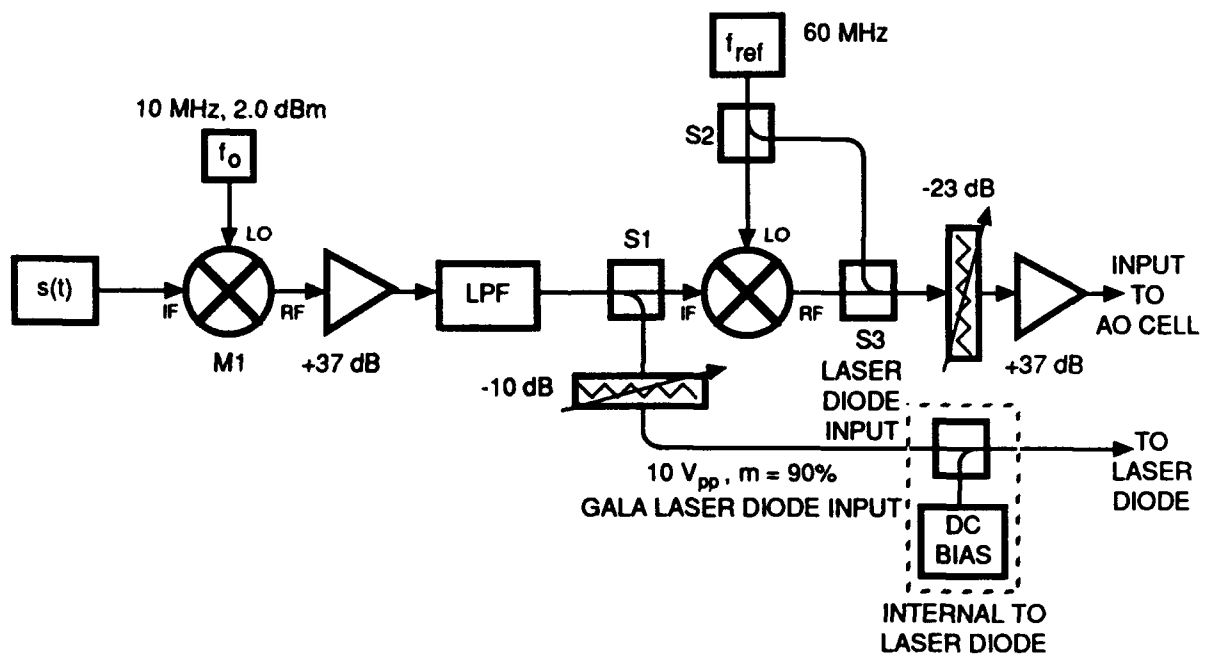
(b) $s(t) = 70 \text{ MHz Sinusoid, After } 46 \text{ dB Attenuation}$

TR-92-SI01-0409

Figure 4-6. Laser Diode Dynamic Range Measurements (Concluded)



(a) Optical Layout of In-Line Correlator



(b) Electronic Signal Generator Design

TR-92-S101-0011

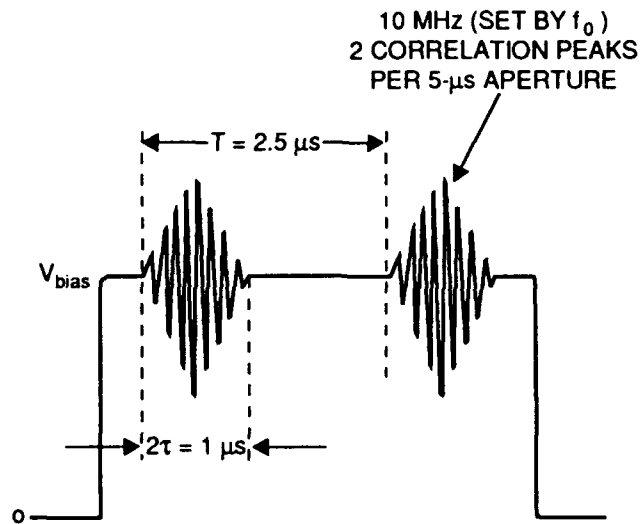
Figure 4-7. In-Line Correlator Breadboard Design

where f_0 is the frequency separation between the IF of the information and the reference tone frequency, and B is the largest bandwidth of information input into either the laser diode or AO cell. The upper limit on f_0 depends on the bandwidths of the AO cell and the laser diode, and the sampling of the CCD array.

Figure 4-8 (a) illustrates the theoretical prediction of the autocorrelation of a pulse train whose parameters are listed in the figure. Given a pulsewidth of t and a pulse-to-pulse separation of T ($T=1/\text{prf}$), the expected triangular correlation theoretically has a width of $2t$ and a correlation peak-to-peak separation of T . Thus, for a pulse train that has a pulsewidth of $t = 0.5 \mu\text{s}$ and $T = 2.5 \mu\text{s}$, the expected autocorrelation width would be $1 \mu\text{s}$ with correlation separation of $2.5 \mu\text{s}$. Since $5.0 \mu\text{s}$ of the AO cell aperture was imaged across the CCD, it was expected that there would be two correlation peaks across the CCD array. **Figure 4-8 (b)** shows the autocorrelation of $s(t)$ at the output of the CCD array. Note that another detector with a 12-bit A/D conversion system was employed during this data collection. The spatial carrier of the correlation corresponds to a reference tone separation of 10 MHz, and the integration time for the CCD array was nominally set at 3 ms. As seen in **Figure 4-8 (b)**, the experimental results were very similar to the theoretical results described earlier. The additional background ripple is a result of an additional bias term imparted on the signal, $s(t)$.

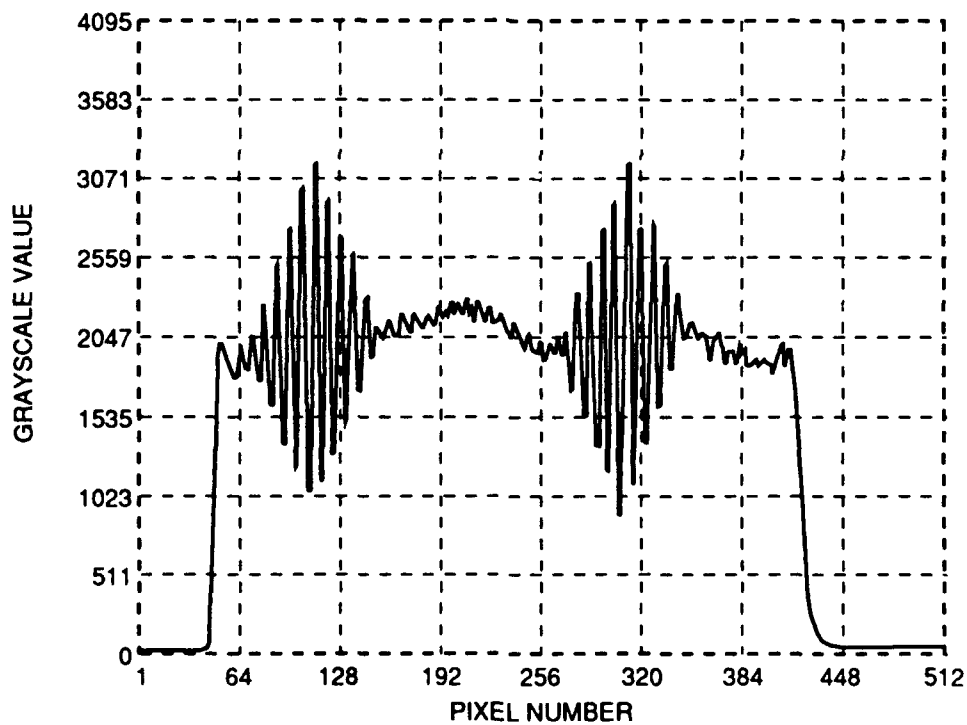
Figure 4-9 (a) shows $s(t)$ for a pulse train for which $t = 0.25 \mu\text{s}$ and $T = 1.25 \mu\text{s}$. Note the additional bias term previously mentioned results in the background ripple. The correlation should be similar in shape to that in **Figure 4-8 (b)**. However, it is expected that the correlation width and separation would be half of that given in the previous example and that the number of correlation peaks would double over the $5.0 \mu\text{s}$ imaged time aperture. **Figure 4-9 (b)** shows the autocorrelation of $s(t)$ at the output of the CCD array and the agreement with expected results. As in the previous example, the spatial carrier of the correlation corresponds to a reference tone separation of 10 MHz and the integration time for the CCD array was set at 3 ms.

As mentioned earlier, the spatial carrier for the in-line architecture can be modified by changing the separation of the electronic reference tone with respect to the information at the IF. Increasing the separation between the reference tone and the IF increases the spatial frequency of the correlation carrier. **Figure 4-9 (c)** shows the autocorrelation of $s(t)$ for a pulse train for which $t = 0.25 \mu\text{s}$, $T = 1.25 \mu\text{s}$, and $f_0 = 15 \text{ MHz}$. Comparing with **Figure 4-9 (b)**, it is obvious that the spatial carrier frequency has increased for increasing tone separation. There are restrictions/limits that must be taken into consideration when selecting the tone separation. As mentioned earlier, the minimum separation is set by the bandwidths to be correlated (see equation 4-8). The upper limit on the tone separation is a function of the number of pixels in the CCD array and the total delay window. There must be an adequate number of pixels to sample each fringe. Other signals were tested with the in-line correlator, including square waves and sinusoids. These results are documented in the Dynetics on-site lab notes.



THEORETICAL PREDICTION FOR AUTOCORRELATION
OF PULSE TRAIN; $\tau = 0.5 \mu\text{s}$, $T = 2.5 \mu\text{s}$, $f_0 = 10 \text{ MHz}$

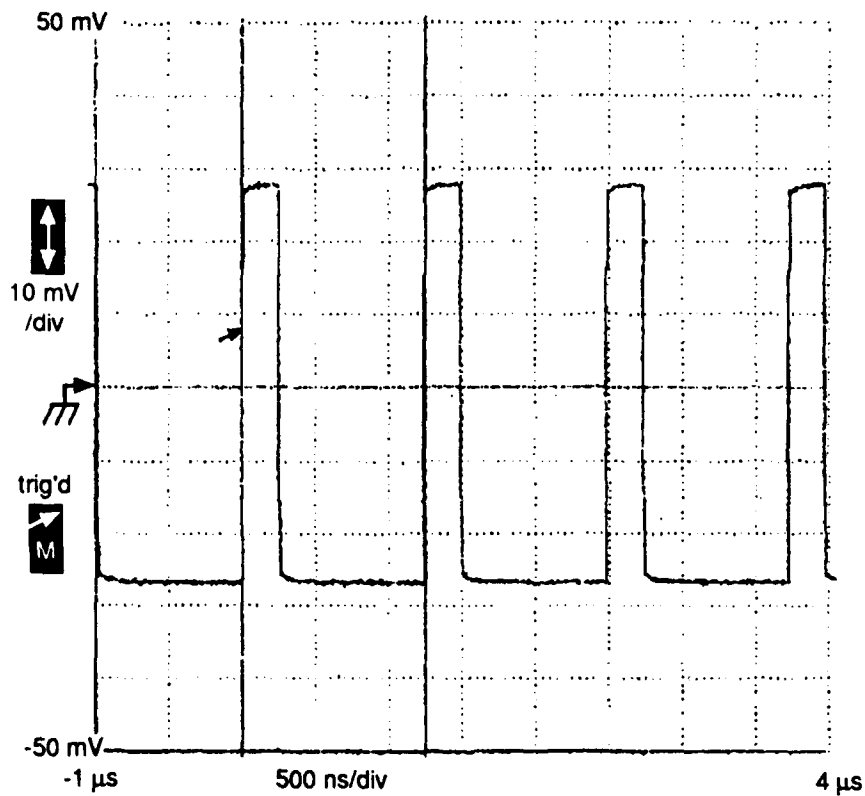
(a) Theoretical Prediction



(b) Experimental Result

TR-92-SI01-0450

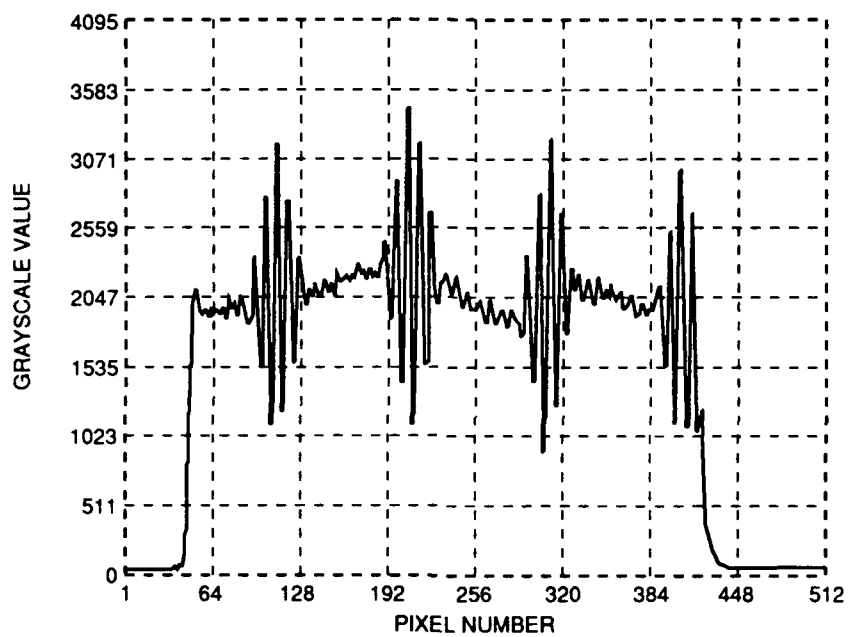
**Figure 4-8. Autocorrelation of $s(t)$ (In-Line): $s(t) = \text{Pulse}$, $\tau = 0.5 \mu\text{s}$,
 $T = 2.5 \mu\text{s}$, $f_0 = 10 \text{ MHz}$**



(a) $s(t) = \text{Pulse}, \tau = 0.25 \mu\text{s}, T = 1.25 \mu\text{s}$

TR-92-S101-0410

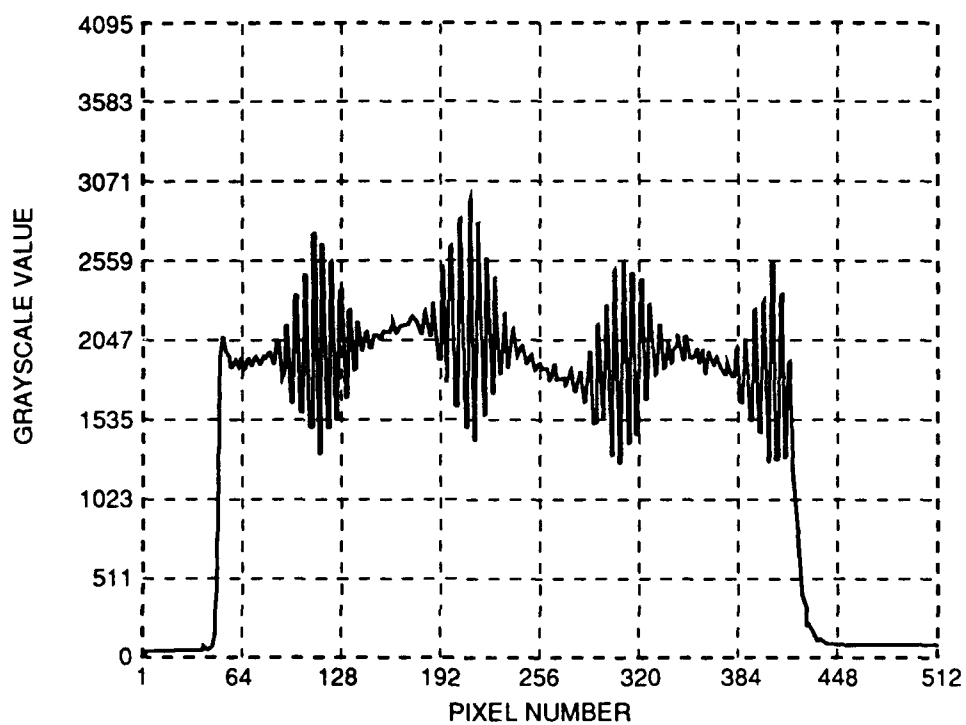
Figure 4-9. In-Line Autocorrelation Results



(b) Autocorrelation with $f_0 = 10.0$ MHz

TR-92-S101-0431

Figure 4-9. In-Line Autocorrelation Results (Continued)



(c) Autocorrelation with $f_0 = 15.0$ MHz

TR-92-SI01-0432

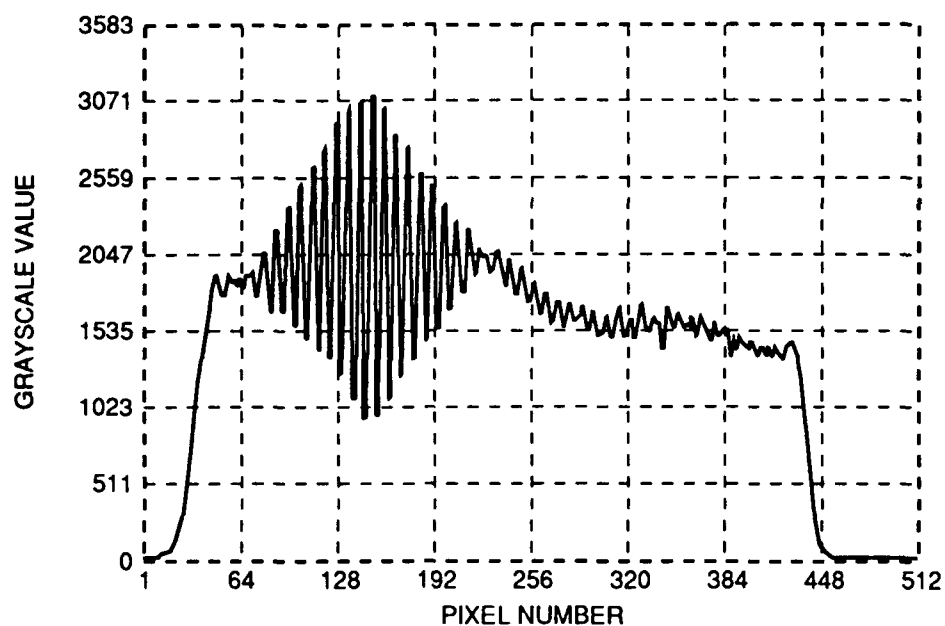
Figure 4-9. In-Line Autocorrelation Results (Concluded)

Preliminary testing was performed to determine an estimate of the in-line correlator dynamic range. The method used was similar to that for testing the dynamic range of the laser diode. A pulse signal, $s(t)$, with pulsewidth $t = 1.0 \mu s$, pulse repetition interval $T = 5.0 \mu s$, and peak-to-peak amplitude $A = 1 V_{pp}$, was input to the in-line correlator system. **Figure 4-10 (a)** illustrates the autocorrelation of the pulse waveform with the above parameters. The waveform was attenuated prior to insertion into the laser diode (the power into the AO cell was kept constant). This would be similar to the reduction of the error signal in the MADOP demonstration. **Figure 4-10 (b) and 4-10 (c)** shows the autocorrelation of $s(t)$ after 25 and 33 dB of signal attenuation. Even after 33 dB of attenuation, the correlation of the signal still can be observed. During this set of tests, however, the background nonuniformities were significant on the CCD array. The background nonuniformities can be seen by inputting a single tone to the AO cell and switching off the modulation to the laser diode. The resultant CCD output is illustrated in **Figure 4-11**. Possible sources for this non-uniformity may include acoustic attenuation in the AO cell and illumination beam nonuniformities. Reduction of this noise can be accomplished through post-processing techniques, as will be illustrated in the next section for the two-path correlator architecture. At the time that these data were recorded, no post-processing software had been developed.

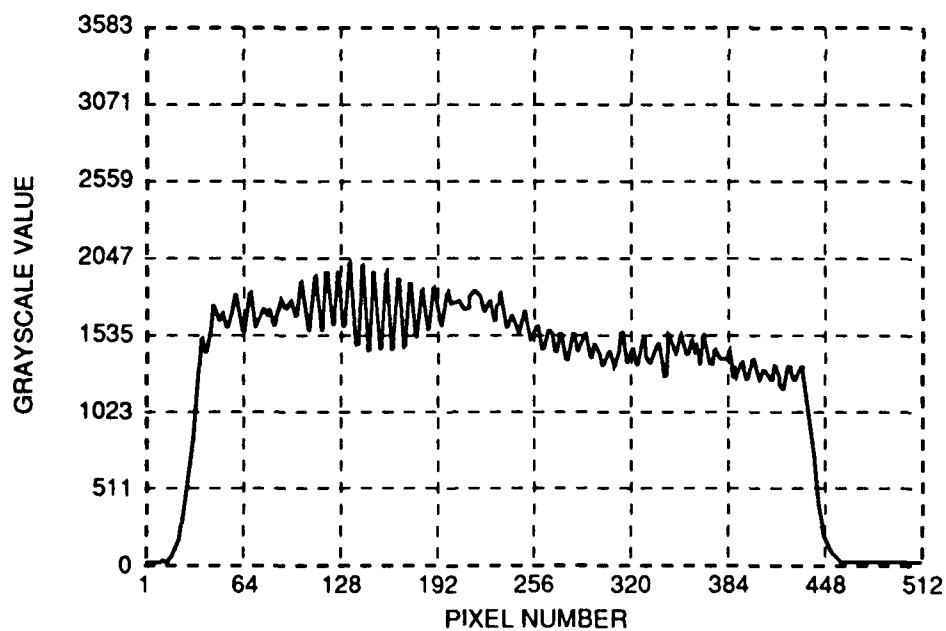
The testing performed on the in-line correlator has given much insight to the architecture setup, operation, capabilities and limitations. Further analysis/testing should be performed since operation and performance of the new components, such as the multichannel AO cell and CCD array, may differ from that of the current components in the preliminary setup. Tests that should be performed include further dynamic range characterization, linearity, delay window uniformity, and the effects of the post-detection processing algorithms on these measurements. Due to time and hardware constraints, full characterization of the in-line architecture did not occur.

4.2.2 Design Alternative II: Two-Path Multichannel Correlator Architecture

An alternative to the above in-line design is achieved through the application of two AO cells in independent paths of a Mach-Zehnder interferometer, as shown in **Figure 4-12**. A continuous wave (CW) laser source is split into two separate paths through the use of a beam splitter. Both paths of the interferometer contain AO cells through which the auxiliary antenna signals and the error signal will be input to the correlator. The error signal is input to the single-channel AO cell and the auxiliary antenna inputs are connected to separate channels of a multichannel device. The error channel can be replicated in the same manner as the laser diode signal replication described previously, or through the use of another multichannel AO cell in the error-signal path. In the latter case, additional RF components would be needed to electrically replicate the RF signal and input the signals into separate channels of the second multichannel device. Advantages of using another multichannel AO cell in the error channel path will be



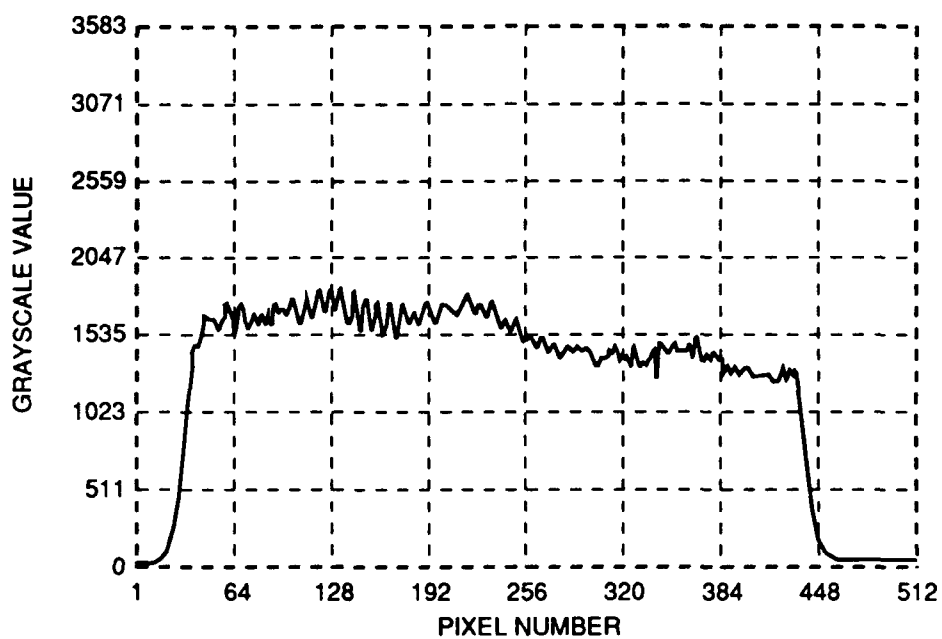
(a) Autocorrelation of $s(t)$ = Pulse, $\tau = 1 \mu s$, $T = 5 \mu s$, $A = 1 V_{pp}$



(b) Autocorrelation after 25 dB Attenuation of $s(t)$

TR-92-SI01-0433

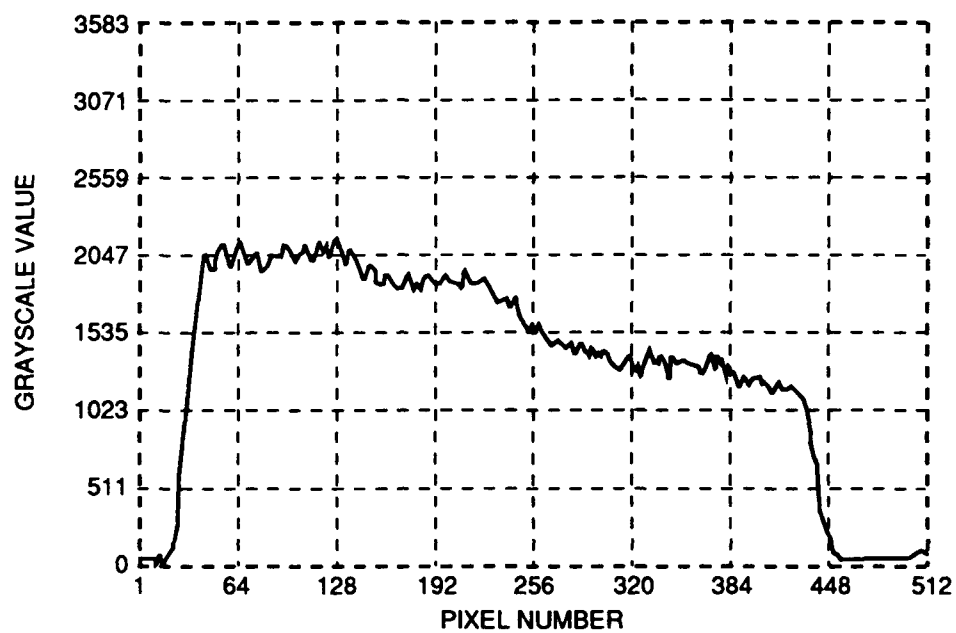
Figure 4-10. In-Line Correlator Dynamic Range Measurements



(c) Autocorrelation after 33 dB Attenuation of $s(t)$

TR-92-SI01-0435

Figure 4-10. In-Line Correlator Dynamic Range Measurements (Concluded)



TR-92-SI01-0436

Figure 4-11. Illumination of CCD Array - No Modulation Input to Laser Diode, Tone Into AO Cell

described later. The separate paths are recombined through another beamsplitter and optical components are used to schlieren image the AO cell diffracted beams onto linear CCD arrays.

In this architecture, the spatial carrier frequency required to operate coherently is set by tilting the beam combiner cube to offset the images on the detector array in angle. Because the recombined beams from a given channel have been equally Doppler-shifted by the AO interaction (the same diffraction order must be selected for each path), the correlation fringe pattern is stationary, thus allowing CW illumination of the AO cells.

Mathematically, this architecture can be viewed as follows. The amplitude of the single-channel AO cell can be expressed as:

$$A_1(t-\tau) = A_e(t-\tau) \exp[-j\phi_e(t-\tau)] \exp[-j2\pi f_0(t-\tau)], \quad (4-9)$$

and for a channel of the multichannel AO cell as:

$$A_2(t+\tau) = A_N(t+\tau) \exp[-j\phi_N(t+\tau)] \exp[-j2\pi f_0(t+\tau)]. \quad (4-10)$$

It can be seen from these equations that the propagation directions are counterpropagating. The detector sees the squared magnitude of the sum of these two amplitudes resulting in the detected signal:

$$\begin{aligned} I_{\text{det}}(t;\tau) &= |A_e(t-\tau) \exp[-j\phi_e(t-\tau)] \exp[-j2\pi f_0(t+\tau)] \\ &\quad + A_N(t+\tau) \exp[-j\phi_N(t+\tau)] \exp[-j2\pi f_0(t+\tau)]|^2 \\ &= |A_e(t-\tau)|^2 + |A_N(t+\tau)|^2 \\ &\quad + 2\text{Re} \{ A_e(t-\tau) \exp[-j\phi_e(t-\tau)] A_N(t+\tau) \\ &\quad \cdot \exp[j\phi_N(t+\tau)] \exp[j4\pi f_0\tau] \}, \end{aligned} \quad (4-11)$$

where $I_{\text{det}}(t;\tau)$ is the instantaneous intensity at the detector. Letting $t' = t - \tau$, this equation as can be written as:

$$\begin{aligned} I_{\text{det}}(t';\tau) &= \text{low frequency biases} \\ &\quad + 2\text{Re} \left\{ \int_0^T A_e(t') \exp[-j\phi_e(t')] A_N(t'+2\tau) \right. \\ &\quad \left. \cdot \exp[j\phi_N(t'+2\tau)] \exp[j4\pi f_0\tau] dt' \right\}. \end{aligned} \quad (4-12)$$

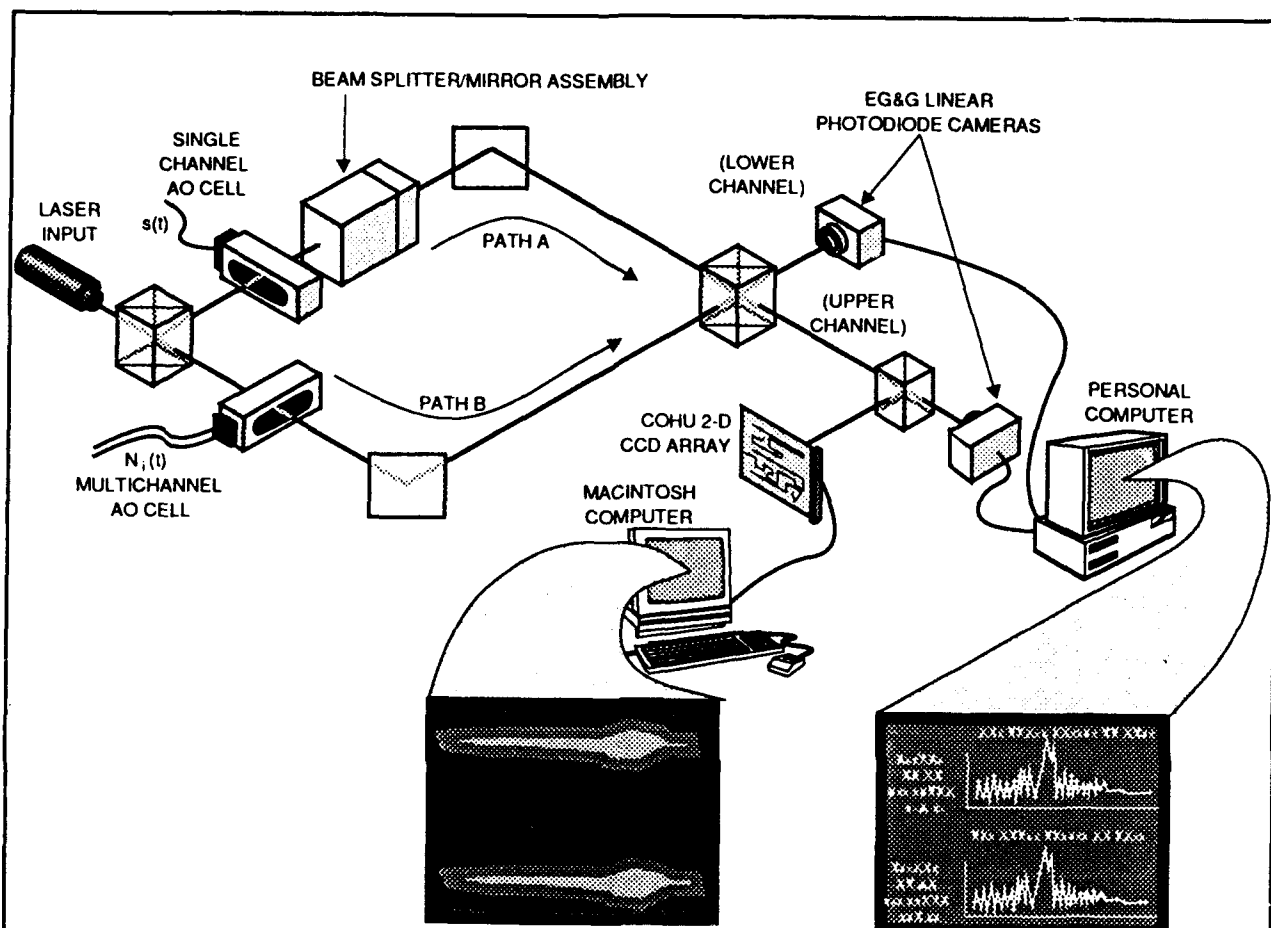
It can be seen from this coordinate transformation that the effective correlation window is doubled for the counterpropagating signals relative to the noncounterpropagating situation characteristic of the in-line alternative. Here again, only one term is at a spatial carrier and temporally at dc. Integration of this term results in the desired carrier-modulated correlation given above. The spatial carrier frequency shown above is the result of the diffraction angle from each cell (a function of the center frequency), and as previously mentioned, can be modified to the desired spatial carrier through adjustment of the beam combiner cube.

In this design of the two-path architecture, the error signal is input to a single-channel AO cell and the auxiliary returns are input to the multichannel AO cell. The diffracted beam from the single-channel AO cell is replicated through the use of beam splitting optics for interference with the multi-channel diffracted beams at the final beam combiner. As a result, the straight-through, single-channel diffracted beam would interfere with one of the multichannel diffracted beams, and the replicated single-channel beam would interfere with the other.

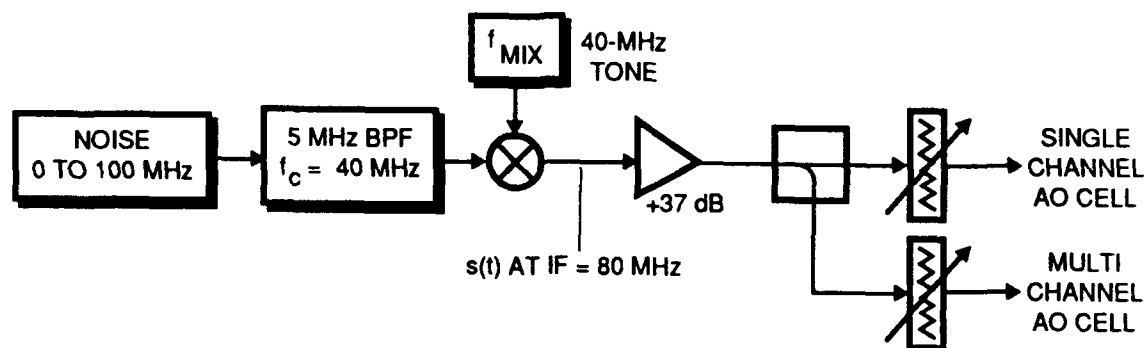
A multichannel, two-path, time-integrating correlator was designed, implemented in hardware, and tested with laboratory-generated signals. The purpose of this stage of design was to determine the utility of the beam splitter/mirror assembly proposed as the beam-replication optics. **Figure 4-13** shows the layout of the two-path correlator with the incorporation of the two 1×512 pixel EG&G LC1901FKN-011 modular line scan cameras and the display of the correlations through the PC and the MAC computer systems. Software developed by 1LT Andrews allowed for real-time display of the camera outputs. With the linear CCD array and display software previously utilized, real-time display of the CCD array output was not possible.

The single-channel AO cell used in this architecture is identical to the AO cell used in the in-line hardware implementation. The multichannel AO cell used for the two-channel test setup is a NEOS device. The index of refraction and thickness of the AO cells and the beam splitter (part of the beam replicating optics in the error signal path) are given in **Table 4-1**. This information was used to calculate the path lengths due to the above components, interferometer path length differences, and imaging compensation due to these components. Imaging compensation refers to the fact that there is a common image/interference plane and that AO cell locations from the imaging lenses are adjusted accordingly.

Unlike the in-line architecture, where the electronic reference determines the spatial carrier frequency, the spatial carrier in the two-path architecture is set by the angles at which the beams in the two paths interfere. This angle is controlled by the tilt and rotation of the second beam splitter/combiner, (BS2). Referring to **Figure 4-14**, rotation of BS2 in the y direction results in changing the tilt angle of fringes. Also, rotation of BS2 in the x direction results in changing the frequency spacing of the spatial fringes. Note that in both cases, the correlation envelope width stays the same and only the tilt and rotation of the fringes within the correlation envelope changes. Wider separation of fringes, accomplished by $\pm x$ direction



(a) Component Layout



(b) Electronic Design for Two-Path Correlator Signal Generation

TR-92-SIO1-0014

Figure 4-13. Two-Path Time-Integrating Correlator

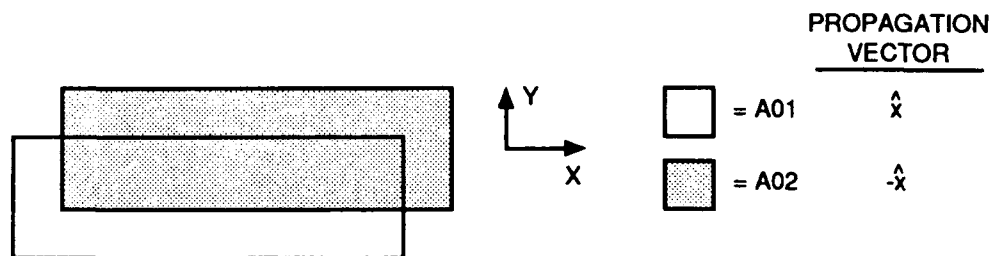
movement, leads to a "zero fringe" condition during which the correlation peak appears to be either all light or all dark. This is illustrated in **Figure 4-14 (c)**. Continuing to move in the x direction leads to increasing fringe frequency (smaller fringe separation). From past experience, it is highly desirable to have vertical fringes if the CCD pixels and acoustic apertures are oriented along the horizontal axis. If a cylindrical lens is used to collapse the information onto a linear CCD array, vertical fringes will aid in increasing fringe contrast by minimizing collapsed fringe overlap on the CCD array.

Table 4-1. Optical Path Length Parameters

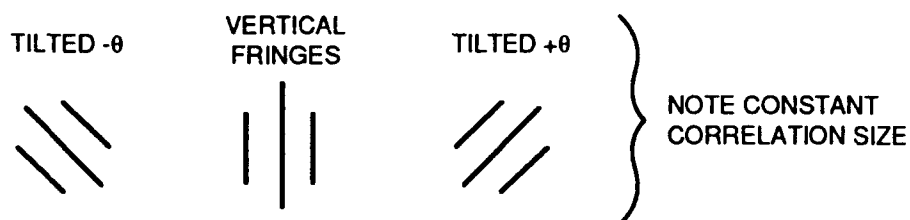
Component	Index at 633 nm	Thickness (nm)
Single-Channel AO Cell	1.68 (flint glass)	60.0
Multichannel AO Cell	2.26 (TeO ₂)	20.0
Beam splitter	1.515 (glass)	50.8

Multichannel correlation was achieved using a 5 MHz noise source (centered at the system IF) as the system input. A 1 MHz square-wave input signal was DSB-SC modulated at 80 MHz and input to the AO cells as a second test waveform. **Figures 4-15 and 4-16** show the multichannel correlation results as displayed on the PC monitor and from the 2-D CCD array.

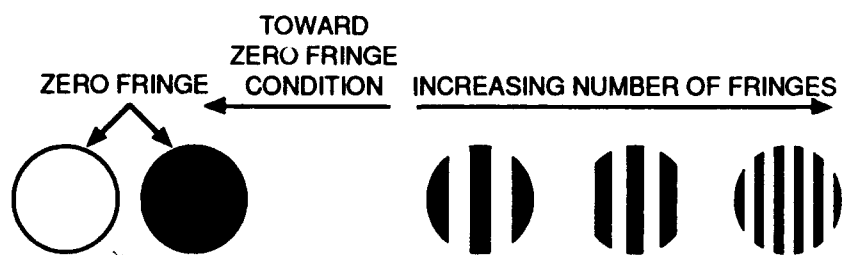
In **Figures 4-15 (b) and 4-16 (b)**, the correlation pattern toward the bottom of both figures is that from the replicated signal path. As can be seen in the figures, there appear to be some additional distortions in the replicated path. This can be best visualized in **Figure 4-16 (b)** by noting the "S" pattern of the fringes for the replicated-path correlation pattern. This was the best fringe pattern obtainable through the use of the beam splitter/mirror assembly adjustments. One cause of the distortions may be the surface quality of the flat mirror. With this in mind, it was decided that in the MADOP hardware implementation, it would be easier, from an alignment standpoint, to use a multichannel AO cell in the error path of a two-path architecture. The insertion of the second multichannel AO cell into the error path of the correlator would allow easy replication of the error channel by signal splitting and inputting the error signal into two separate channels of the multichannel device. Additional advantages of using a multichannel AO cell in the error path of the correlator include the elimination of the beam splitter/mirror assembly, the reduction of optical path differences between correlator paths and between correlator channels, and co-planar diffracted beams from the AO cell for each channel utilized (reducing alignment requirements of channels in the error path). It is important that the transducer/channel spacing is the same for both the multichannel cells, since it is very difficult to adjust the individual channel overlap in the correlation/acoustic image plane. Thus, it is desirable to procure an additional matched (in terms of device specifications and operational parameters) multichannel AO cell to be used as the error signal AO cell.



(a) Acoustic Aperture and Propagation Orientations



(b) Fringe Rotation (given a constant fringe separation)
Due to Moving Optical Beam in $\pm \hat{y}$ Direction

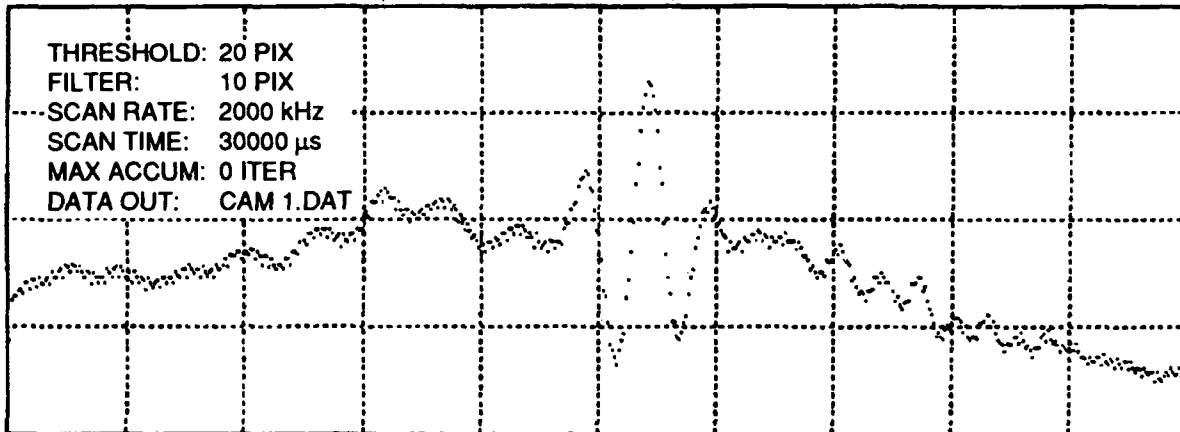


(c) Fringe Separation (given a constant angular tilt)
Due to Moving Optical Beam in $\pm \hat{x}$ Direction

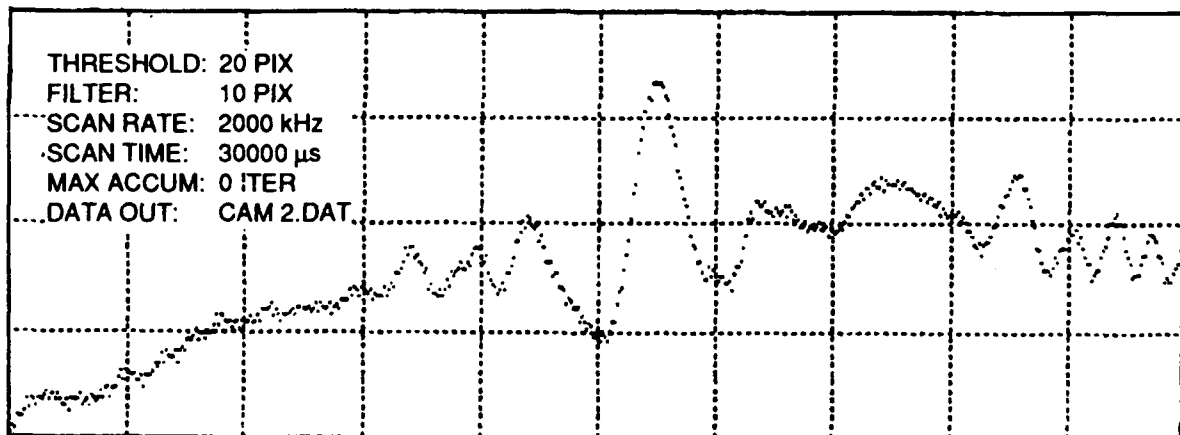
TR-92-SI01-0015

**Figure 4-14. Spatial Fringe Frequency/Orientation as Function
of Acoustic Beam Image Overlap Positions**

CAMERA 1 - GRAY SCALE



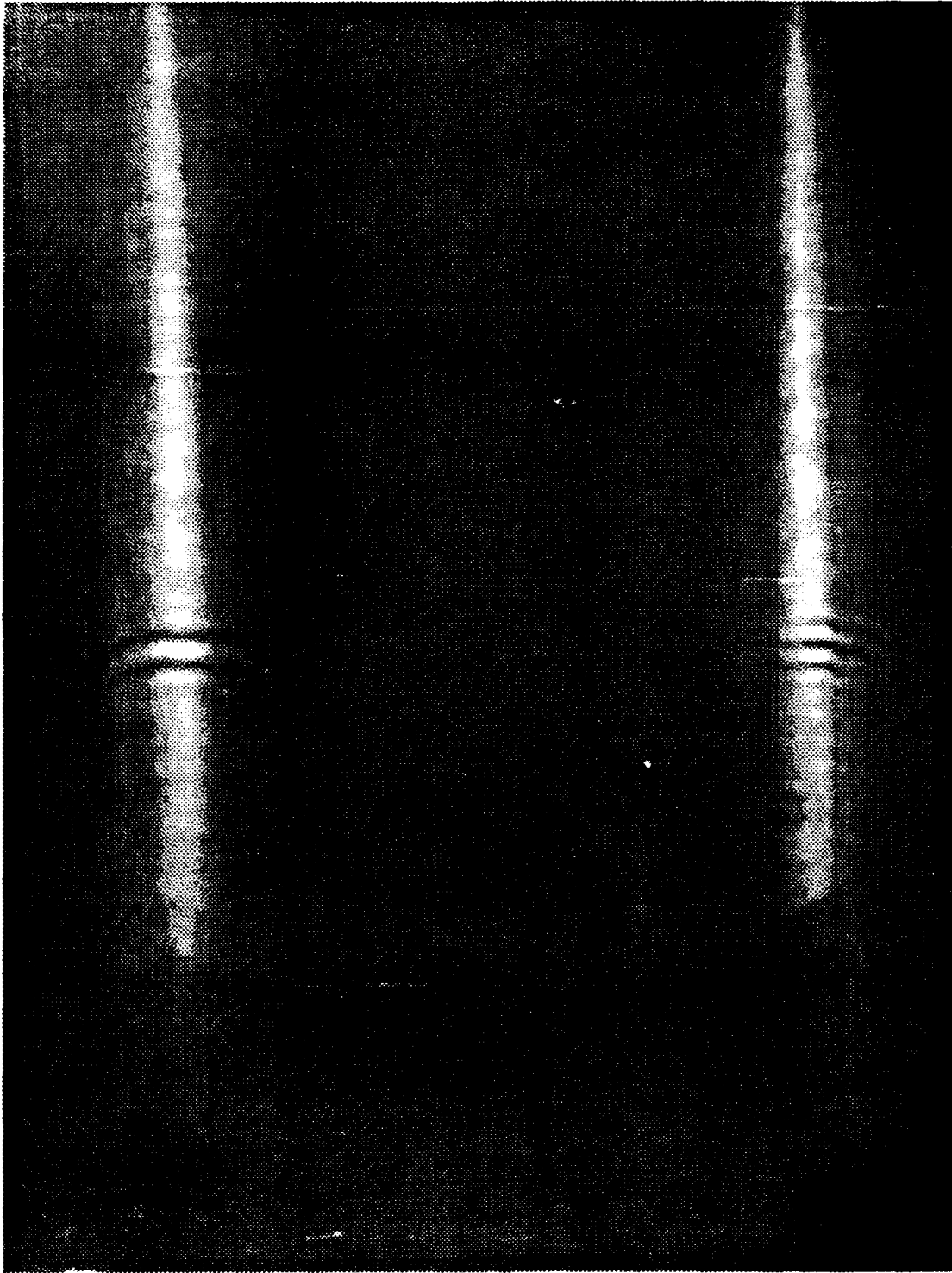
CAMERA 2 - GRAY SCALE



(a) Linear CCD Array Output

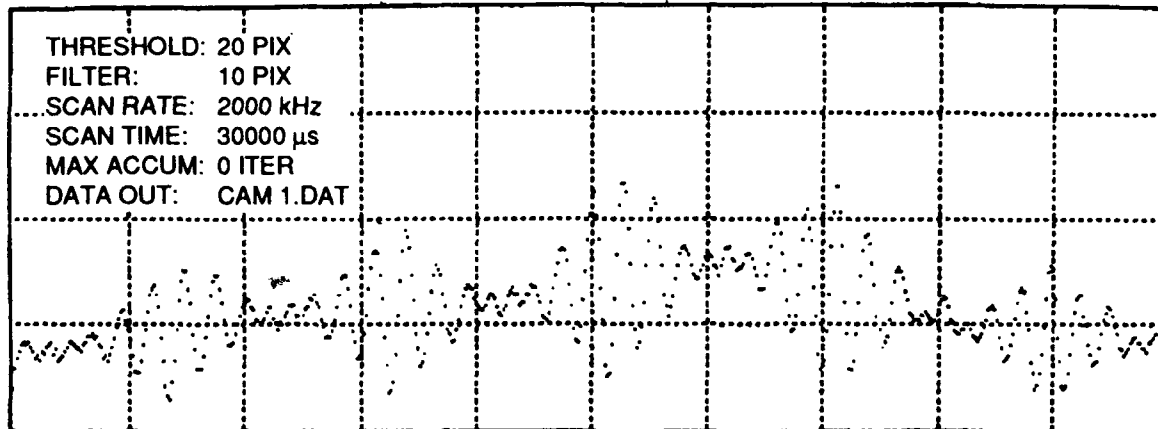
TR-92-S101-0411

Figure 4-15. Multichannel Correlation of 5 MHz Noise Source Input

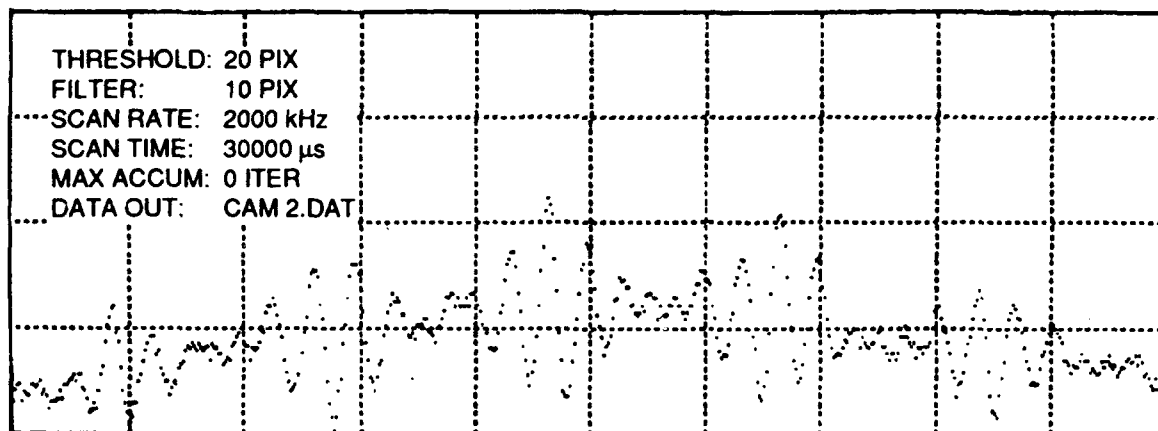


(b) 2-D CCD Output
Figure 4-15. Multichannel Correlation of 5 MHz Noise Source Input (Concluded)

CAMERA 1 - GRAY SCALE



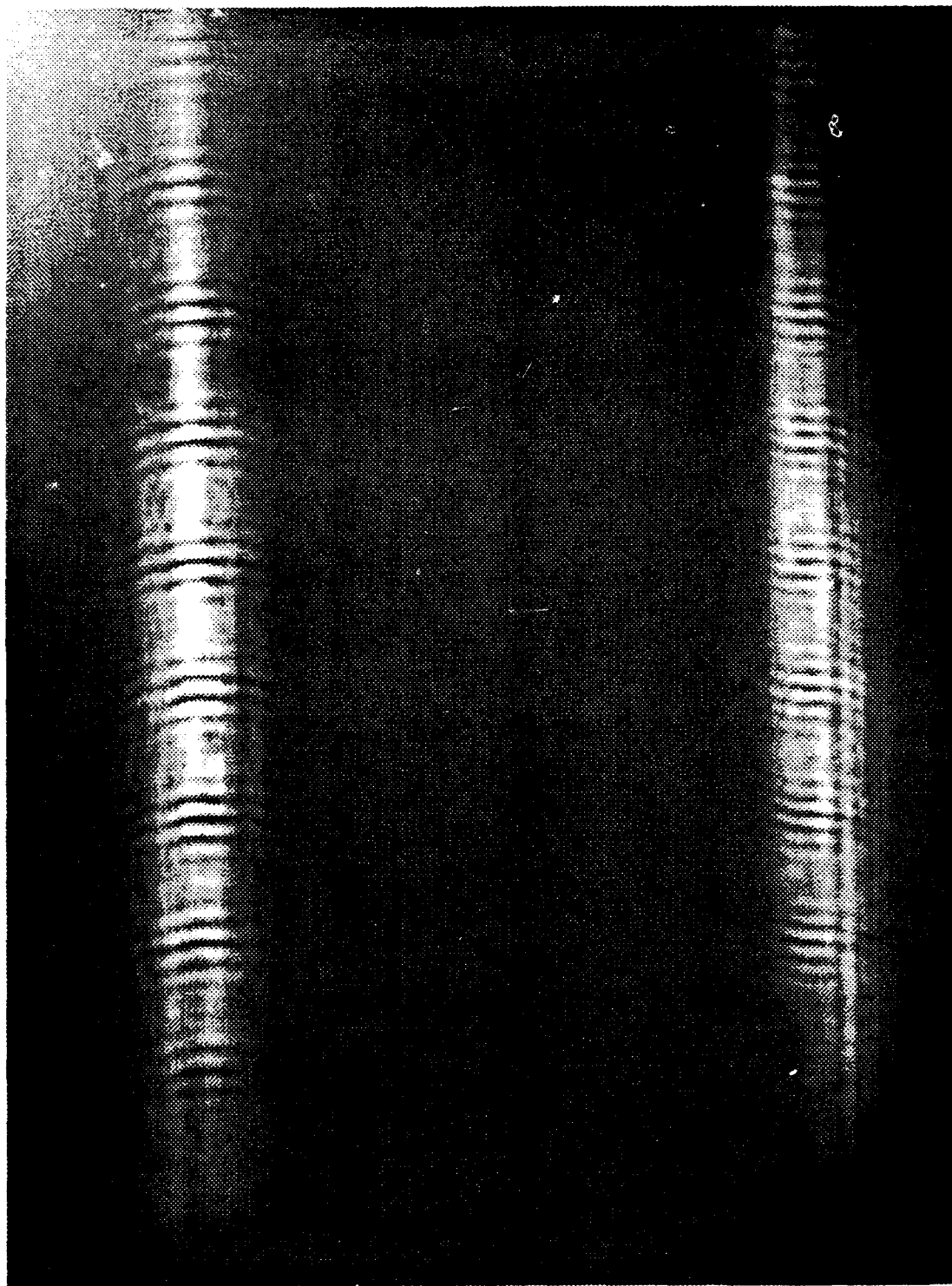
CAMERA 2 - GRAY SCALE



(a) Linear CCD Array Output

TR-92-SI01-0412

Figure 4-16. Multichannel Correlation of 1 MHz Square Wave Input



(b) 2-D CCD Output
Figure 4-16. Multichannel Correlation of 1 MHz Square Wave Input (Concluded)

A redesign of the two-path correlator optical layout was performed due to the insertion of the Brimrose multichannel AO cell (in the auxiliary antenna path) and the use of the EG&G CCD arrays. **Figure 4-17** shows a top-view optical layout of the interferometric paths of the two-path correlator. L1 and a second lens L2 (not shown), placed after BS2, are used to image the appropriate AO cell apertures back onto the CCD arrays. The magnification of the imaging system is given by the ratio of the focal lengths of L1 and L2. **Figure 4-17** illustrates how path differences due to different AO cell materials and thicknesses were taken into consideration during component layout and correlator alignment. In the figure, the two optical paths of the Mach-Zehnder interferometer are laid out without path folding. The top path is the one with the interaction AO cell (AO1) and the bottom path is the Brimrose AO cell (AO2) path. BS1 and BS2 refer to the first and second beam splitters, respectively; t_1 and t_2 refer to the thicknesses of the AO cells; n_1 and n_2 are the indices of refraction of the AO cells; SF refers to the spatial filters; Δ is a set separation between SF and BS2; and Δ_1 and Δ_2 refer to the distance between BS1 and the respective AO cell. As indicated, L2 is located after the second beam splitter (BS2). For the optical component layout calculations, the center of the acoustic column location was assumed to be located at $t/2$. This gives rise to the $n_i t/2$ location of the object plane from the front face of the AO cell. The total path length in each path is given by the following equation:

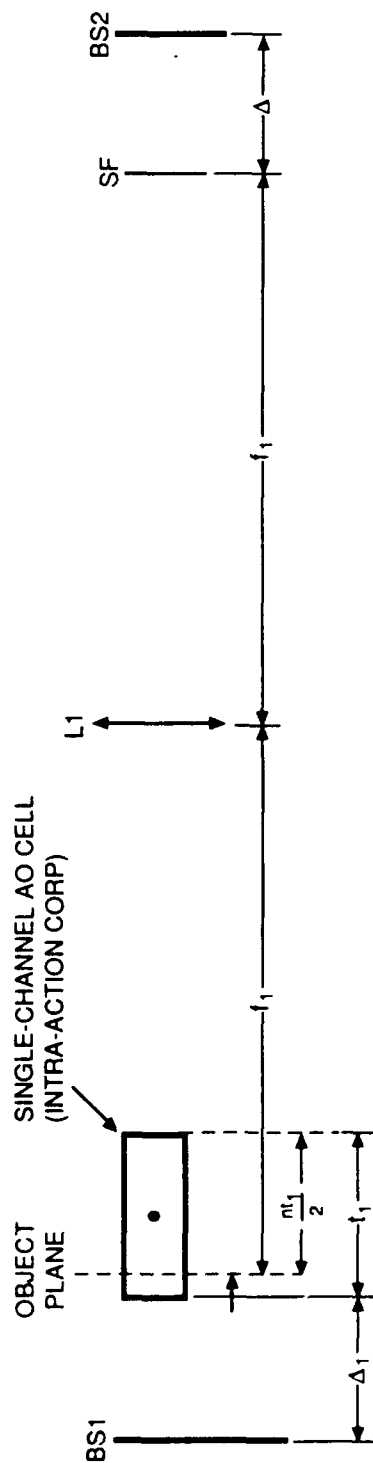
$$L(1) = 2f_1 + \Delta + \Delta_1 + \left[t_1 \left(1 - \frac{n_1}{2} \right) \right]_{AO1}$$

$$L(2) = 2f_1 + \Delta + \Delta_2 + \left[t_2 \left(1 - \frac{n_2}{2} \right) \right]_{AO2}$$
(4-13)

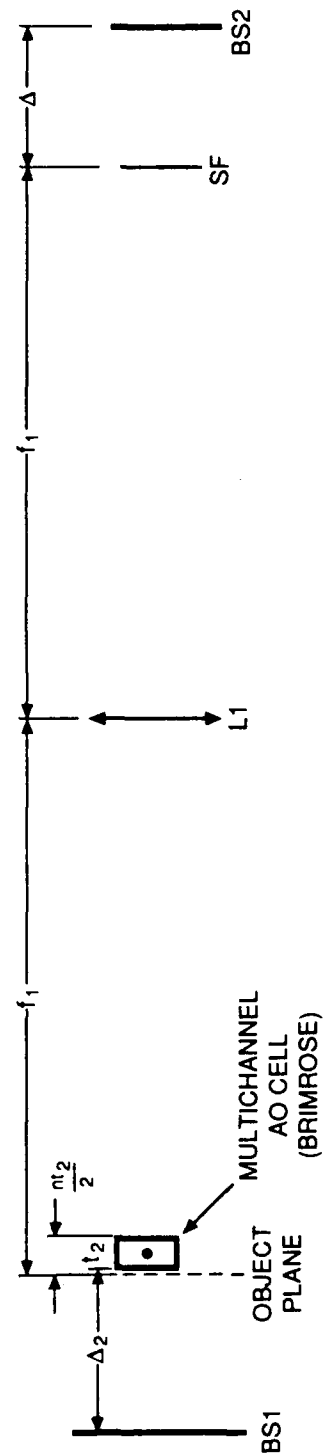
where $L(i)$ is the total path length in path i from BS1 to BS2, and f_1 is the focal length of L1.

The requirement for optical system magnification was calculated in the following manner. The Brimrose AO cell is TeO_2 [L] and has an acoustic velocity of 4.2×10^3 m/s. Thus, a $2.5 \mu\text{s}$ time aperture in the AO cell corresponds to approximately 10.5 mm. In the IntraAction AO cell, this aperture dimension was calculated to be 10.05 mm. Note that with the two-path, Mach-Zehnder, time-integrating correlator architecture, the correlation time window is twice that of the imaged AO cell apertures if equal acoustic apertures are imaged (see Equation 4-12). Given a 6.656-mm detector array length for the EG&G CCD arrays, a magnification of $M = 0.634$ was calculated to image 10.5 mm of each AO cell. Using a two-lens imaging system and the available lenses, a magnification of $M = 0.625$ was achieved using $f_1 = 200$ mm and $f_2 = 125$ mm. With these focal lengths, the path length for each leg of the interferometer was selected to be $L(1) = L(2) = 488$ mm.

Figure 4-18 illustrates the design of the electronics used to generate the input signals to the AO cells. The electronics were designed to generate DSB-SC signals at the system IF (80 MHz). Test signals



(a) Path 1 - Error Channel Path (Single)

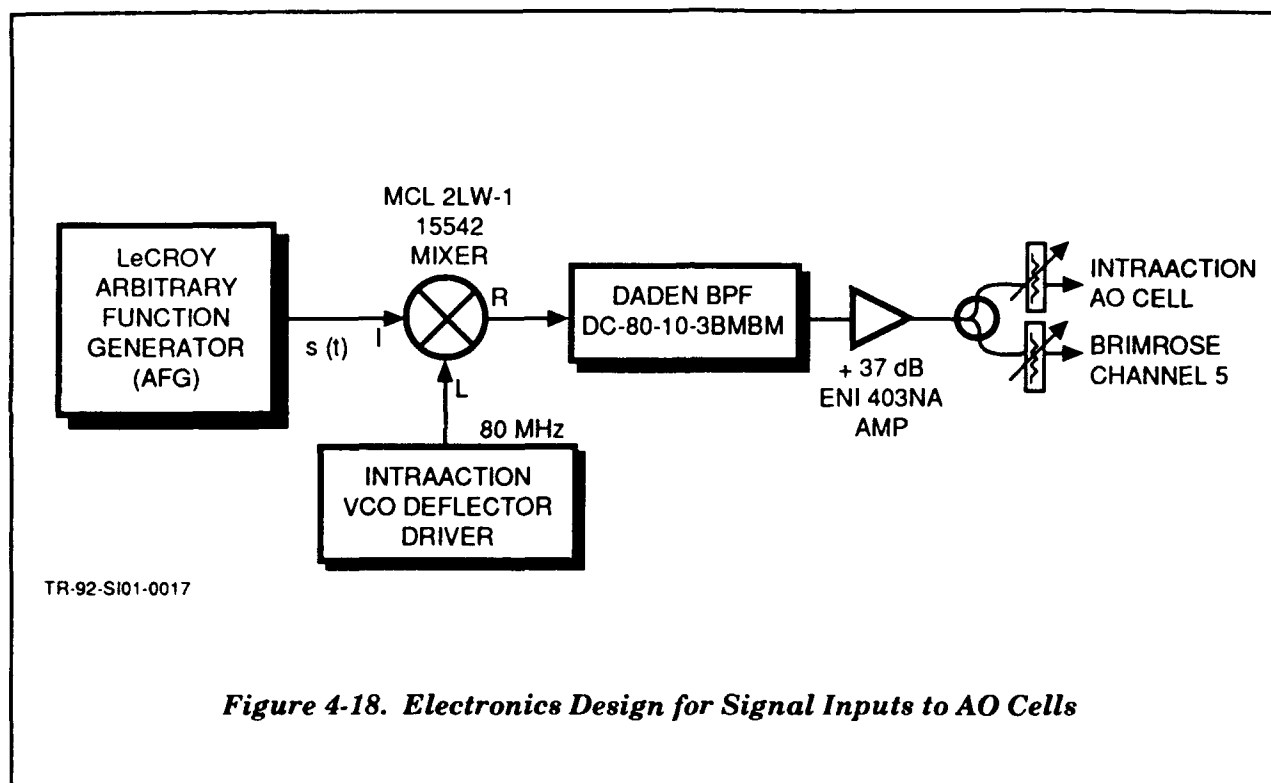


(b) Path 2 - Multichannel AO Cell Path

Figure 4-17. Interferometric Path Optical Layout

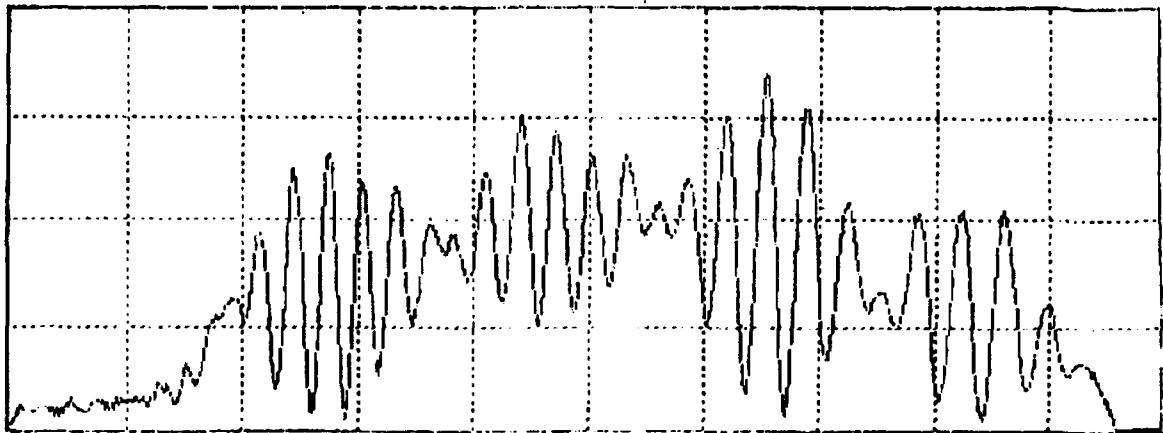
TR-92-SIO1-0016

were generated at base band and mixed with a carrier tone of 80 MHz. In the figure, I, L, and R refer to the input/output nomenclature on the Mini Circuits Labs (MCL) mixer. It should be noted here for reference that when using MCL mixer P/N ZP-10514, DSB-SC could not be achieved. Switching to an MCL mixer P/N 15542 (as noted in the figure) enabled DSB-SC signal modulations to be accomplished. In addition to using band limited (at base band) noise signal inputs, the LeCroy Arbitrary Function Generator (AFG) was used to generate some base band test signals which were DSB-SC modulated prior to system input. **Figure 4-19 (a) and (b)** illustrates the autocorrelation of a 500 kHz sinusoid as viewed by the EG&G linear CCD array and by the COHU 2-D CCD arrays, respectively.



Enhancements to the PC display software, implemented by 1LT Andrews, increased the capabilities of the real-time EG&G array displays. For example, menu-driven options exist for the subtraction of array backgrounds. This option, along with the addition of a positive bias, was utilized for the subtraction of beam nonuniformities due to the illumination source and due to the AO cell diffraction pattern. Implementation of this was performed in the following manner. The signals were input to the AO cells in the regular manner for detection of autocorrelation. This included adjusting the power level into the AO cells so, on the average, the diffracted intensities from the two cells were equal. With one of the optical paths blocked, the intensity pattern incident on the CCD array showed the nonuniformities described above. After subtracting the background pattern (from a preset positive bias), the above step was repeated for the other

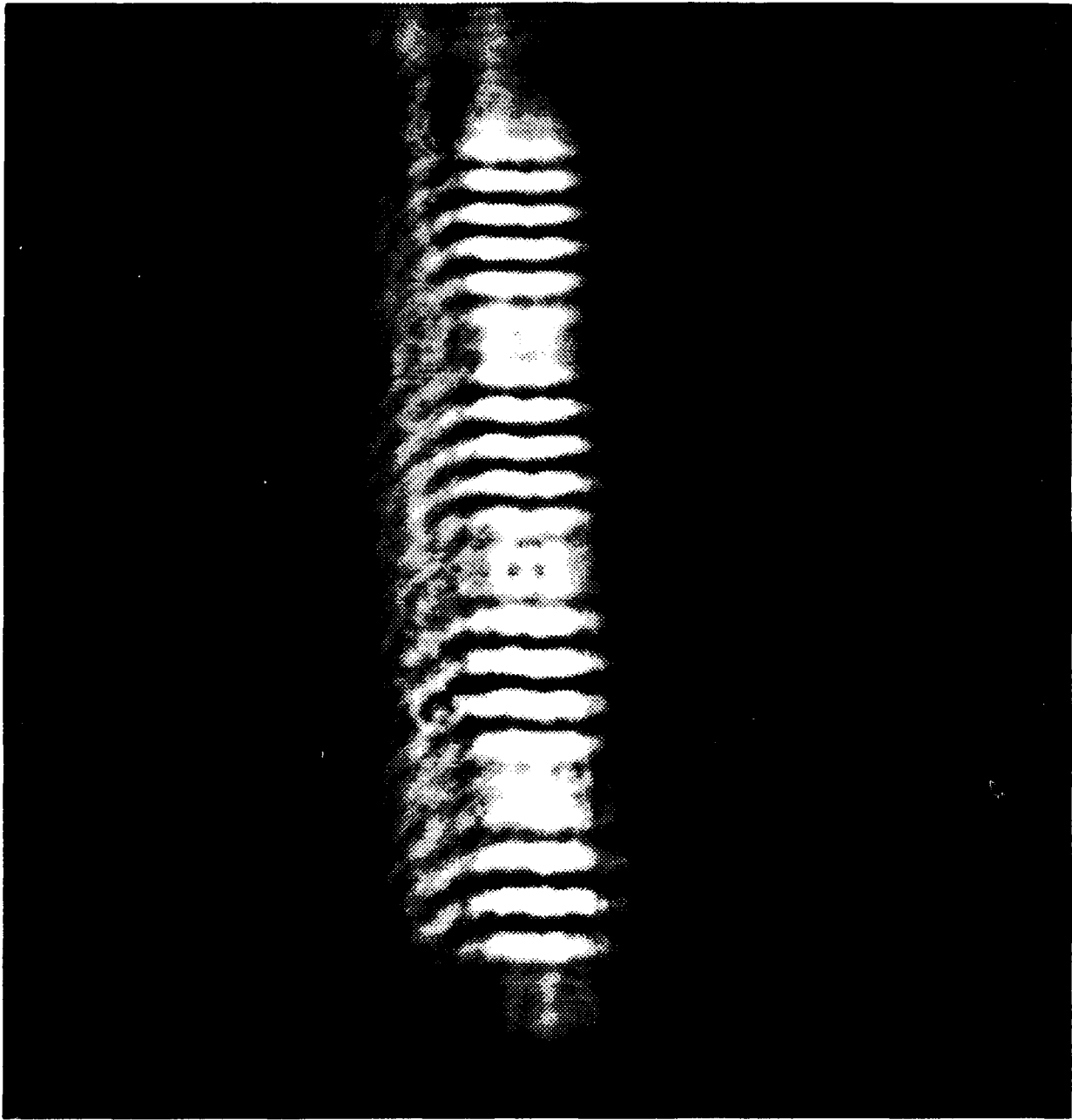
CAMERA 2 - GRAY SCALE



(a) Linear CCD Array Output

TR-92-SI01-0413

Figure 4-19. Correlation Results: $s(t) = 500 \text{ kHz Sinusoid}$



(b) COHU CCD Array Output

Figure 4-19. Correlation Results; $s(t) = 500$ kHz Sinusoid (Concluded)

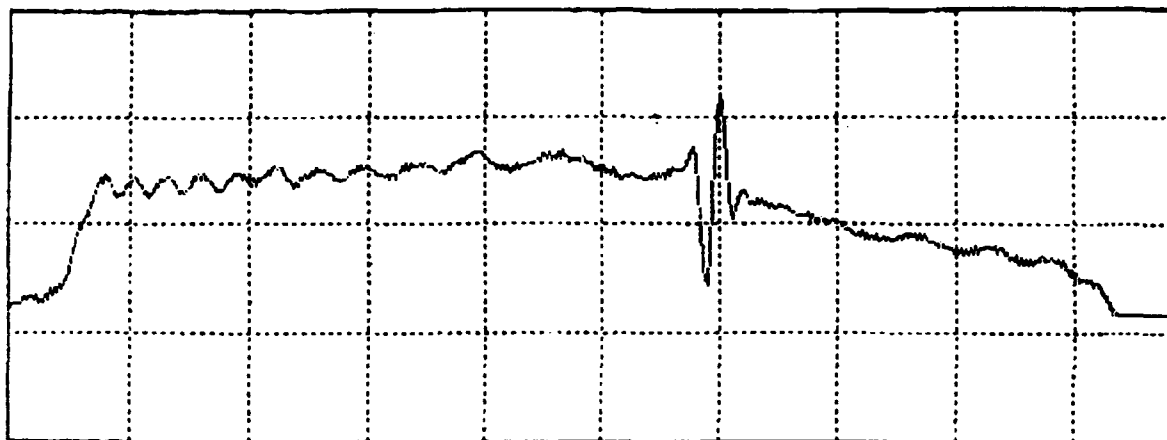
optical path. This resulted in a uniform bias about which the correlation signal was positioned. **Figure 4-20 (a)** illustrates the correlation output for wide band noise input to the AO cells. The overlapping 3 dB bandwidth of the signal, set by the AO cell pass bands, was 25 MHz. As shown in the figure, there is a nonuniform background/bias. **Figure 4-20 (b)** illustrates the same correlation output after bias addition and subtraction of the background in the manner described above. Note the improvement in the background signal and the increased correlation peak modulation depth. There are other methods for performing this sort of "post-processing" technique, such as bi-phase subtraction and bandpass filtering, but for the current stage of correlation testing, the current near-real-time technique is adequate.

A preliminary test of the dynamic range of the two-path correlator was performed. A pulse train ($t = 0.1 \mu s$, $T = 5.0 \mu s$), shown in **Figure 4-21 (a)**, was DSB-SC modulated at 80 MHz and input into both AO cells. Note that there is no bias on the pulse train. As mentioned earlier, if the bias is part of the signal being autocorrelated, the autocorrelation of the bias will also be modulated by the carrier. With the bias removed from the pulse signal, fringes will only be present across the autocorrelation of the pulse. **Figure 4-21 (b)** illustrates the input spectrum to the AO cells and **Figure 4-21 (c)** shows the output correlation pattern after performing the post-processing operation described above. The error channel input was attenuated and the correlation was viewed on the PC monitor. Due to the changing input RF power levels in the error channel, the background subtraction technique was repeated after each attenuation step. The autocorrelation of $s(t)$ after 30 and 35 dB attenuation of the error channel input is shown in **Figure 4-21 (d) and 4-21 (e)**. Incorporation of additional or alternative post-processing techniques may increase this dynamic range. Another method for increasing the dynamic range would incorporate the use of automatic gain control (AGC) to the error signal prior to insertion into the AO cell.

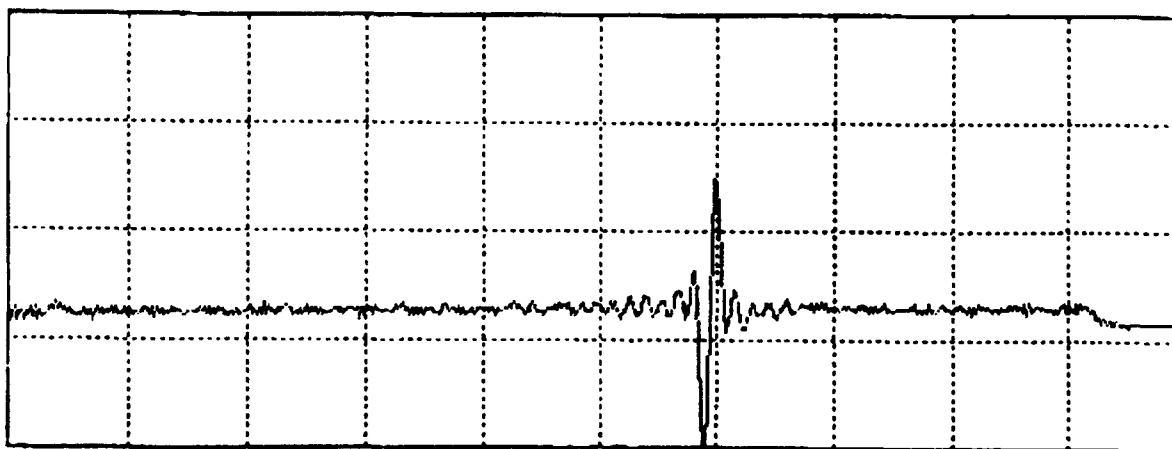
4.2.3 Time-Integrating Correlator Architectural Considerations

It is desirable to select and emphasize one of the time-integrating correlator architectures with respect to hardware fabrication and signal testing. To assist in the architectural evaluations, **Table 4-2** lists the features associated with each of the architectures. One of the in-line architecture drawbacks that should be pointed out is that a long time-delay (on the order of half the desired time aperture) is required prior to signal insertion into the laser diode. This is necessary to center the correlation in the delay window as illustrated in **Figure 4-22**. Consider a signal, $s(t)$, simultaneously input to a laser diode and an AO cell. Due to the nature of the AO cell, the signal representation as it propagates through the crystal (neglecting propagation losses) is given by:

$$s(t, x) = s\left(t - \frac{T}{2} - \frac{x}{v_a}\right) \quad (4-14)$$



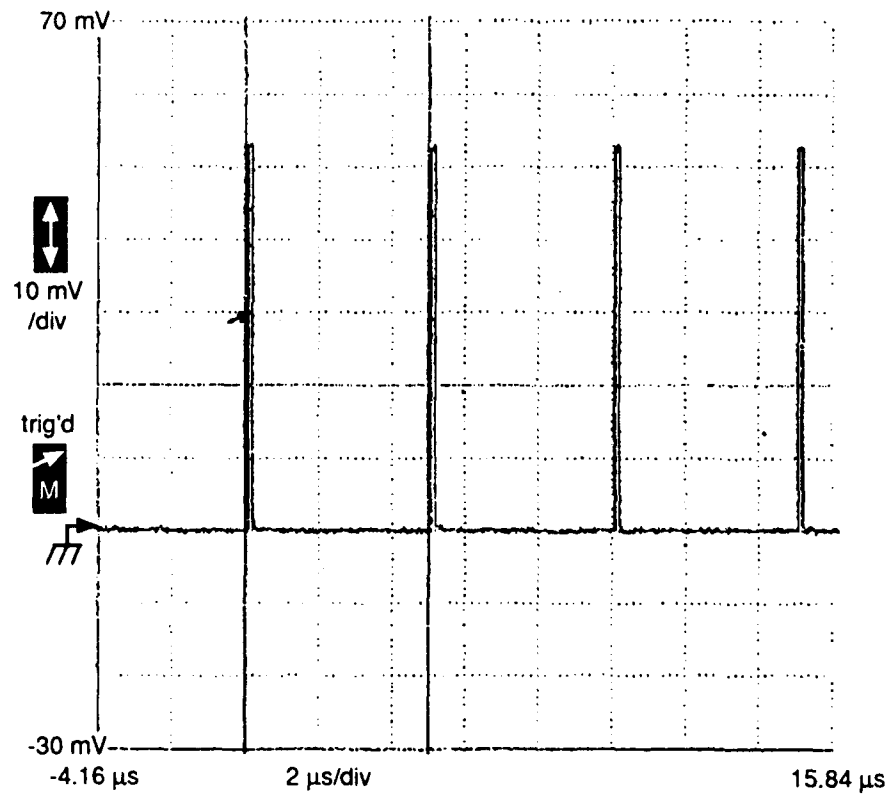
(a) Linear CCD Array Output



(b) Linear CCD Array Output After Background Subtraction

TR-92-SI01-0414

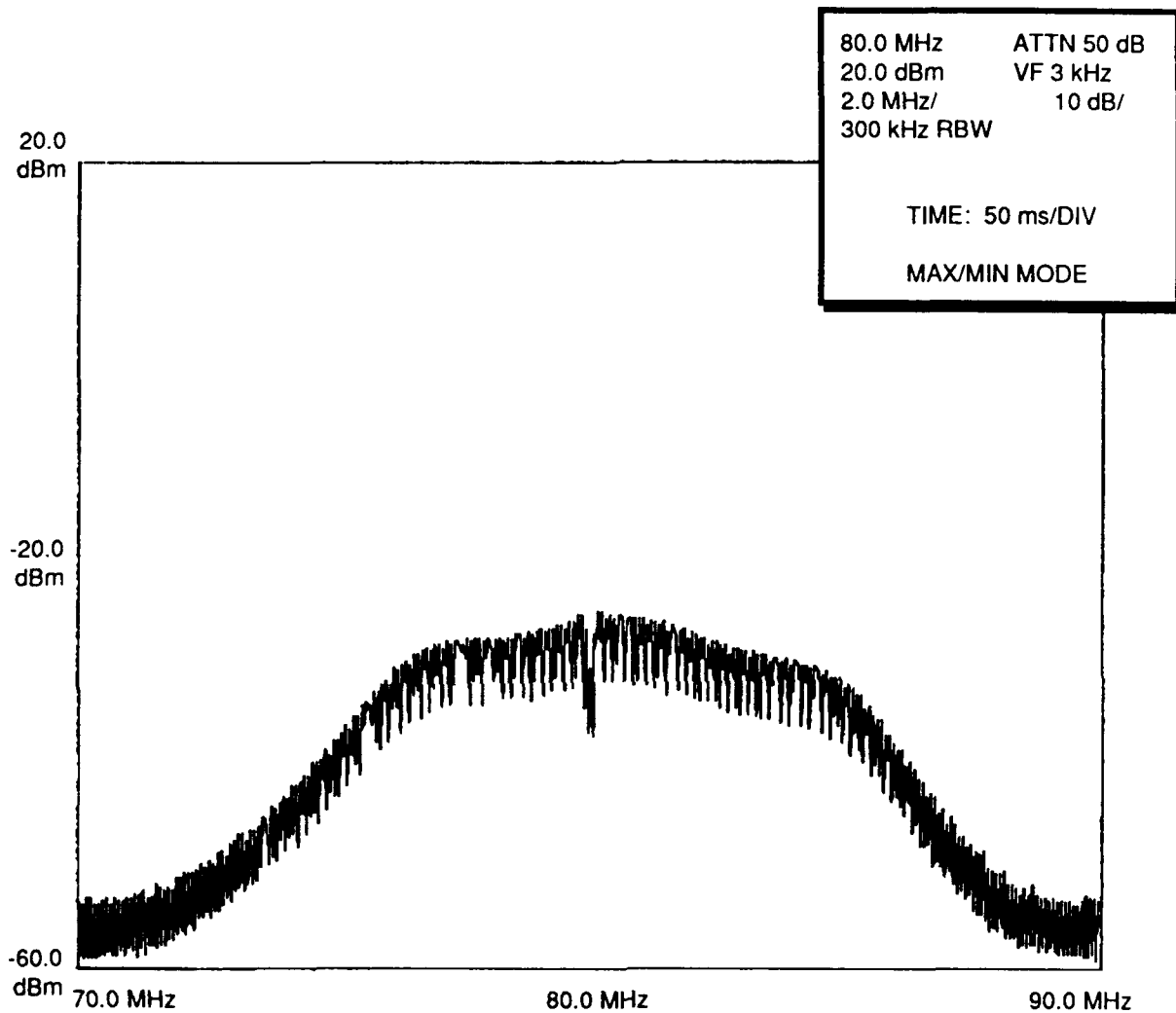
Figure 4-20. Noise Autocorrelation



(a) $s(t) = \text{Pulse}, \tau = 0.1 \mu\text{s}, T = 5 \mu\text{s}$

TR-92-S101-0415

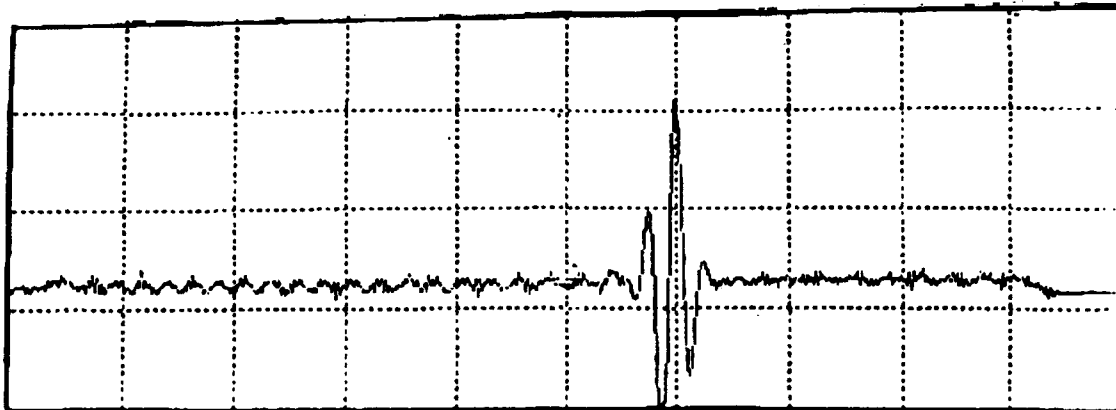
Figure 4-21. Two-Path Correlator Dynamic Range Measurements



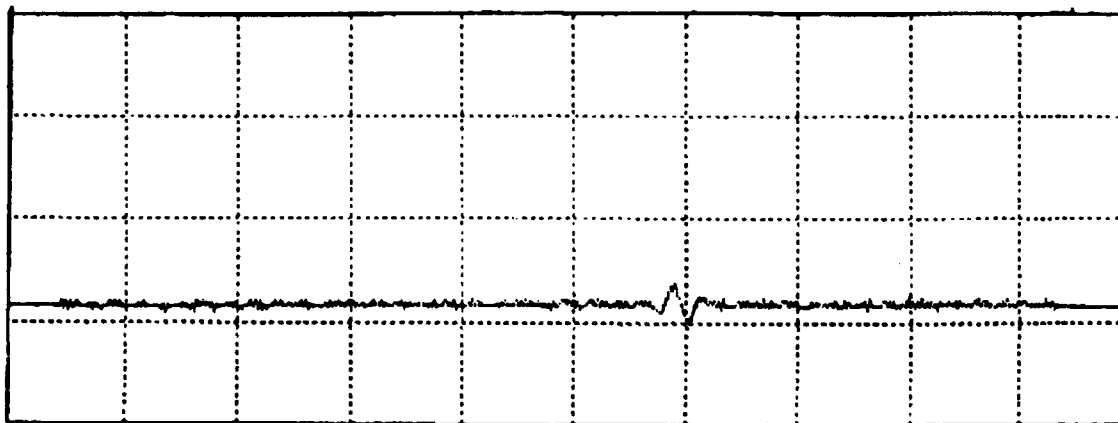
(b) Spectrum of $s(t)$ on 80-MHz Carrier

TR-92-SI01-0416

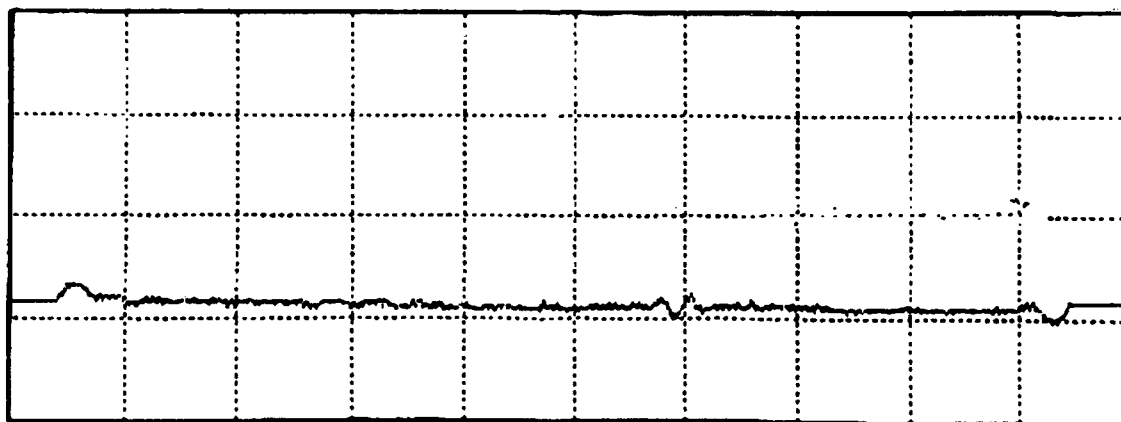
Figure 4-21. Two-Path Correlator Dynamic Range Measurements (Continued)



(c) Autocorrelation of S (t)



(d) Autocorrelation After 30-dB Attenuation of Error Channel



(e) Autocorrelation After 35-dB Attenuation of Error Channel

TR-92-S101-0417

Figure 4-21. Two-Path Correlator Dynamic Range Measurements (Concluded)

where T is the time aperture of the AO cell, x is the dimension in the direction of the acoustic propagation (referenced to the center of the aperture), and v_a is the acoustic velocity of the AO crystal. The term $[T/2 + x/v_a]$ is commonly referred to as the delay. When a wide band signal is input to the *in-line correlator* and there is no delay between the signal inputs to the AO cell and the laser diode, the correlation occurs at the zero delay point. As noted in the figure, the zero delay point corresponds to:

$$x = -\frac{v_a T}{2} \quad (4-15)$$

which is at the transducer side of the acoustic aperture. To center the correlation peak at the center of the aperture, it is necessary to time-delay the input to the laser diode by an amount equal to $T/2$. For the time apertures necessary for the MADOP, these time-delay differences can be easily achieved through the use of the BAW delay lines being procured. Another possible solution to this issue involves using an AO point modulator to provide the necessary intensity modulation. Selection of different delays can then be accomplished through selecting different locations in the modulator to illuminate.

Table 4-2. Time-Integrating Correlator Architecture Features

Two Path (Additive)	In-Line (Multiplicative)
Signal inputs at system IF	Signal inputs to laser not at system IF
Sensitive to vibration/thermal gradients	Stability inherent in common-path architecture
Manual spatial carrier adjustment	Electronic control of spatial carrier
CW illumination of AO cells	Modulated illumination source required (laser diode or point modulator)
Range window is twice AO time aperture	Range window is AO cell time aperture
Cell bandwidth = processing bandwidth	Cell bandwidth ≥ 1.5 processing bandwidth
	Signal generation of reference tones required
	Vertical fringes
	Laser diode stability issues
	Large RF time delay required in laser diode path (half of time aperture). Needed to achieve center correlation

With all the architectural considerations presented above and in **Table 4-2**, it was decided that the emphasis for hardware implementation and testing would be the two-path correlator architecture. It is recommended that work on the in-line correlator hardware implementation proceed on an as-needed basis.

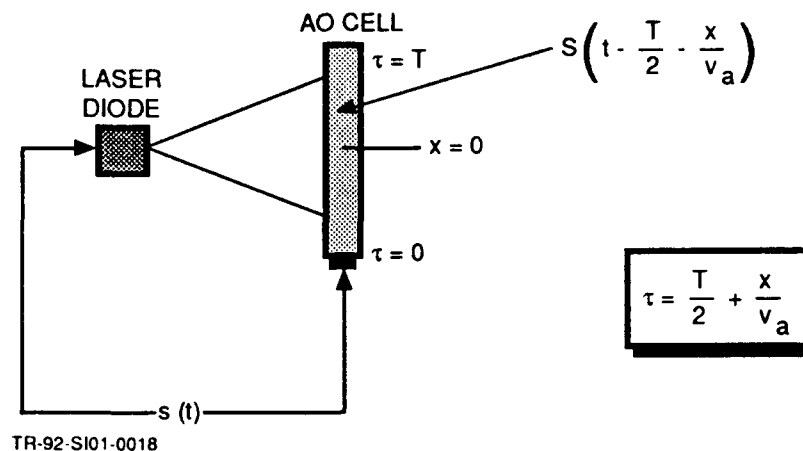


Figure 4-22. In-Line Schematic Illustrating Additional Delay Required in LD Path

4.3 AOTDL FILTER

Much of the analysis, design, and hardware implementations during the current effort was directed at the tapped delay line portion of the system. The previous architecture (Reference 1) provided effective tapped delay line filtering, but required DSB waveform modulation together with a strong tone at the carrier frequency. The architectures described in this subsection are evolutions of this prior system to realize filtering of arbitrary signal modulations at the system IF. Subsection 4.3.1 describes in mathematical detail a Mach-Zehnder architecture for creating a tapped delay-line that outputs the desired signal at the system 80-MHz IF. This architecture was found to be deficient in generating true time-delay due to very subtle properties of AO cells and interferometric architectures. This deficiency will be fully described in Subsection 4.3.1.7.

A noninterferometric architecture for generating the desired tapped delay-line properties was a natural outgrowth of the increased insight into the limitations of the Mach-Zehnder approach. The development of a two-channel version of this architecture is reviewed in Subsection 4.3.2. Included are characterization results that point to the need for several improvements, most notably in the stabilization of the system and the optical lens design.

4.3.1 AOTDL Interferometric Architecture Design and Limitations

The Mach-Zehnder architecture for implementing the tapped delay line is shown in **Figure 4-23**. The key to this architecture is the addition of a reference path that is initiated after the AO spatial light modulator (AOSLM). This path is Doppler-shifted by the input tap frequency information in an identical fashion to the Doppler-shifted light that illuminates the AOTDL. After recombination on the photodetector, this effectively cancels the tap-dependent Doppler frequency shift contribution of the AOSLM, provides the output at the same IF as the signal input to the AOTDL, and reduces the impact of cross-terms in this output.

Referring again to **Figure 4-23**, the operation can be described as follows. The AOSLM is illuminated with an unmodulated "sheet" beam that is collimated in the direction of acoustic propagation and focused using cylindrical lenses in the orthogonal direction (not shown). The output of the AOSLM is deflected in angle proportional to the input frequencies, is Doppler-shifted by an amount equal to these input frequencies, and has an amplitude proportional to the amplitude of the input frequency components. Lens L1 then forms the spatial Fourier transform of this information at plane P1, where an aperture allows only the +1 order of diffraction to pass. Lens L1 has a long focal length, f_1 , to provide a large Fourier transform where the frequency coordinate, τ , is given as:

$$\tau = \lambda f_1 f_x = \lambda f_1 \frac{f}{v_a} \quad (4-16)$$

where λ is the optical wavelength, f_x is the spatial frequency of the input acoustic wave ($f_x = f/v_a$), f is the input frequency and v_a is the acoustic velocity (4200 m/s for longitudinal TeO₂). Lenses L2 and L3 then serve as a telescope to image this Fourier plane, with magnification f_3/f_2 , to the plane of the AOTDL. Thus, a single frequency at the input to the AOSLM acts to tap the AOTDL at a given position:

$$\tau = \lambda \frac{f_1 f_3}{f_2} \frac{f}{v_a} \quad (4-17)$$

and with an optical frequency that is Doppler-shifted by an amount equal to f . Lens L4 then takes a final Fourier transform of this output to convert the tap positions into tilted plane waves that are incident on the detector with an angle proportional to tap position. The combination of lenses L1 and L2 (a telescope) images the AOSLM aperture to plane P2, then the combination of lenses L3 and L4 images plane P2 to the plane of the detector. Therefore, the combination of AO cells and lenses serves to:

1. Image the AOSLM aperture onto the detector with magnification

$$M = \frac{f_2 f_4}{f_1 f_3} \quad (4-18)$$

2. Transform the AOTDL to create plane waves incident on the detector for each tap position at an angle proportional to the tap position, and
3. Transform the AOTDL to create images of the AOSLM at positions corresponding to each of the frequencies input into the AOTDL.

The reference path is created by a beam splitter at the input to the AOTDL and is made to be coincident with the diffracted information from the AOTDL for each tap position and for a given input frequency (the AOTDL center frequency). The reference beam then interferes temporally (heterodynes) with the beam from the signal path to form the desired output at the system IF. The Doppler shift, due to the AOSLM, will cancel out when the two paths are heterodyned.

The following interpretations of the math will be useful in working through the equations to follow:

1. Tilted plane wave: $\exp[j\alpha x]$ or $\exp[j\alpha\tau]$, where x and τ are spatial coordinates,
2. Magnified and shifted image: $M^{-1}g(x/M - dx/M)$, where dx is the positional shift, and
3. Time delay as a linear-in-frequency phase shift for a tone:

$$\exp[j2\pi f(t - \tau)] = \exp[j2\pi f t] \exp[-j2\pi f \tau].$$

4.3.1.1 AOSLM Mathematical Description

We first consider the tap function input to the AOSLM given by:

$$f(t) = \sum_{i=1}^N a_i \cos 2\pi f_i t \quad (4-19)$$

where a_i and f_i are the tap amplitude and frequency, respectively. The term a_i^2 has units of power. Note that the phase of the AOSLM input will not affect the processor output since it will cancel during heterodyne detection. This signal results in the acoustic wave diffracted output for +1 diffraction (ignoring the undiffracted beam blocked at plane P1) given by:

$$f\left(t - \frac{T}{2} - \frac{x}{v_a}\right) = A\eta_f^{1/2} w(x) \sum_{i=1}^N a_i \exp\left[j2\pi f_i \left(t - \frac{T}{2} - \frac{x}{v_a}\right)\right] \quad (4-20)$$

where A is the incident plane-wave amplitude, η_f is the AO cell diffraction efficiency in percentage per RF watt, and $w(x)$ is the apodization function due to beam shape, acoustic aperture, acoustic attenuation, lens aberrations, etc. The nonuniform frequency response of the AOSLM is included for convenience in the coefficients a_i . The frequency response can be electronically equalized by use of a pre-multiplication look-up table that is a function of f_i .

As described above, lenses L1, L2 and L3 form the Fourier transform of Equation 4-20 and display this on the aperture of the AOTDL with frequency coordinates given by Equation 4-17. Mathematically, this signal is given at Plane P1 as (Reference 19):

$$F(t, \tau) = A \sqrt{\frac{1}{\lambda f_1}} \eta_f^{1/2} \int_{-\infty}^{\infty} w(x) \sum_{i=1}^N a_i \exp \left[j2\pi f_i \left(t - \frac{\tau}{2} - \frac{x}{v_a} \right) \right] \exp \left[-j2\pi x \frac{\tau}{\lambda f_1} \right] dx \quad (4-21)$$

where the π phase shift ($1/j$) is neglected. Using substitutions and Fourier transform properties, we arrive at the transform:

$$F(t, \tau) = A \sqrt{\frac{1}{\lambda f_1}} \eta_f^{1/2} \sum_{i=1}^N a_i W \left(\frac{\tau}{\lambda f_1} + \frac{f_i}{v_a} \right) \exp \left[j2\pi f_i \left(t - \frac{\tau}{2} \right) \right]. \quad (4-22)$$

After lenses L2 and L3, Equation 4-22 can be modified to include the telescope magnification to yield the resultant illumination of the AOTDL given by:

$$F(t, \tau) = A \sqrt{\frac{f_2}{\lambda f_1 f_3}} \eta_f^{1/2} \sum_{i=1}^N a_i W \left(\frac{\tau f_2}{\lambda f_1 f_3} + \frac{f_i}{v_a} \right) \exp \left[j2\pi f_i \left(t - \frac{\tau}{2} \right) \right]. \quad (4-23)$$

4.3.1.2 Reference Beam Path

The pattern $F(t, \tau)$ passes through two legs of a Mach-Zehnder interferometer, one of which contains the AOTDL and one of which will be referred to as the reference path. The input to the AOTDL consists of individual beams for $i=1, 2, \dots, N$, all of which are parallel to each other and individually diverging. This is a consequence of the Fourier transform properties, where points on the input map to plane waves on the output, and plane waves on the input map to diverging parallel beams on the output. The final lens, L4, then transforms the AOTDL diffracted and undiffracted beams onto the detector to form a magnified version of the beams at plane P2, i.e., lenses L3 and L4 act as another telescope with magnification. This is also effectively the image of the AOSLM aperture, consisting of overlapped plane wave beams at various incident angles corresponding to the various AOSLM input frequencies. Therefore, the reference beam at the detector is:

$$f(t, x) = A \sqrt{\frac{f_1 f_3}{f_2 f_4}} \eta_f^{1/2} w \left(\frac{x f_1 f_3}{f_2 f_4} \right) \sum_{i=1}^N a_i \exp \left[-j2\pi f_i \frac{f_1 f_3 x}{f_2 f_4 v_a} \right] \exp \left[j2\pi f_i \left(t - \frac{\tau}{2} \right) \right]. \quad (4-24)$$

4.3.1.3 Signal Beam Path: Signal Carrying Beam

Now consider the signal path of the Mach-Zehnder interferometer. Consider an input signal to the AOTDL given by:

$$s(t) = a(t) \cos [2\pi \mathcal{F} t + \phi(t)] \quad (4-25)$$

which is a complex modulation of a carrier, \mathcal{F} . For a better understanding of the equations to follow, this signal is represented:

$$s(t) = \sum_{j=1}^M b_j \cos [2\pi \mathcal{F}_j t + \phi_j]. \quad (4-26)$$

Referring back to Equation 4-17, the AOTDL is tapped at positions:

$$\tau_i = \lambda f_1 f_3 f_i / f_2 v_a \quad (4-27)$$

resulting in the diffracted signal outputs (recall that propagation is in the $-\tau$ direction):

$$S\left(t - \frac{T}{2} + \frac{\tau}{v_a}\right) = A \sqrt{\frac{f_2}{\lambda f_1 f_3}} \eta_f^{1/2} \eta_f^{1/2} \sum_{i=1}^N \sum_{j=1}^M a_i W\left(\frac{\tau f_2}{\lambda f_1 f_3} + \frac{f_i}{v_a}\right) b_j \exp[j\phi_j] \\ \cdot \exp\left[j2\pi \mathcal{F}_j \left(t - \frac{T}{2} + \frac{\tau}{v_a}\right)\right] \exp\left[j2\pi f_i \left(t - \frac{T}{2}\right)\right]. \quad (4-28)$$

The next-to-last term contains a component $\exp[j2\pi \mathcal{F}_j \tau / v_a]$, which is the resulting angular offset of the diffracted beam with respect to the undiffracted beam. The offset at the input center frequency is removed relative to the reference beam of Equation 4-24 by tilting the mirror in the signal path and aligning the beam combiner cube so that the signal and reference paths superimpose after recombination, as shown in **Figure 4-23**. We then define the signal frequencies relative to the center frequency as $\Delta \mathcal{F}_j$ ($\Delta \mathcal{F}_j = 0$ for the center frequency). Therefore, after removing this offset,

$$S(t, \tau) = A \sqrt{\frac{f_2}{\lambda f_1 f_3}} \eta_f \sum_{i=1}^N \sum_{j=1}^M a_i W\left(\frac{\tau f_2}{\lambda f_1 f_3} + \frac{f_i}{v_a}\right) b_j \exp[j\phi_j] \\ \cdot \exp\left[j2\pi (\mathcal{F}_j + f_i) \left(t - \frac{T}{2}\right)\right] \exp\left[j2\pi \Delta \mathcal{F}_j \frac{\tau}{v_a}\right]. \quad (4-29)$$

Lens L4 then takes the Fourier transform of this signal as was done in Equations 4-21 through 4-23 (the exponential in the Fourier integral is now positive). Therefore, the signal beam at the detector is:

$$s(t,x) = A \sqrt{\frac{f_2}{\lambda f_1 f_3}} \sqrt{\frac{1}{\lambda f_4}} \eta_f \int_{-\infty}^{\infty} \sum_{i=1}^N \sum_{j=1}^M a_i w \left(\frac{\tau f_2}{\lambda f_1 f_3} + \frac{f_i}{v_a} \right) b_j \exp[j\phi_j] \cdot \exp \left[j2\pi (\mathcal{F}_j + f_i) \left(t - \frac{T}{2} \right) \right] \exp \left[j2\pi \Delta \mathcal{F}_j \frac{\tau}{v_a} \right] \exp \left[j2\pi \tau \frac{x}{\lambda f_4} \right] d\tau. \quad (4-30)$$

This can be simplified by using the Fourier transform properties to yield:

$$s(t,x) = A \sqrt{\frac{f_1 f_3}{f_2 f_4}} \eta_f \sum_{i=1}^N \sum_{j=1}^M a_i w \left(\frac{x f_1 f_3}{f_2 f_4} + \lambda \Delta \mathcal{F}_j \frac{f_1 f_3}{f_2 v_a} \right) \exp \left[-j2\pi f_i \frac{f_1 f_3 x}{f_2 f_4 v_a} \right] \cdot b_j \exp[j\phi_j] \exp \left[-j2\pi f_i \frac{\lambda \Delta \mathcal{F}_j f_1 f_3}{f_2 v_a^2} \right] \exp \left[j2\pi (\mathcal{F}_j + f_i) \left(t - \frac{T}{2} \right) \right]. \quad (4-31)$$

To simplify this notation, we define a position independent phase offset given as:

$$\Delta \Phi_{ij} = -2\pi f_i \frac{\lambda \Delta \mathcal{F}_j f_1 f_3}{f_2 v_a^2} \quad (4-32)$$

which is dependent on both tap position and signal frequency. This phase term, which is linear in tap position and linear in offset signal frequency (relative to the signal center frequency), is apparently the relative time delay of the signal for a given tap position, as was shown in Item 3 immediately preceding Subsection 4.3.1.1. This apparent time delay is the source of the limitation of this architecture, as will be described in Subsection 4.3.1.7. The signal beam at the detector is:

$$s(t,x) = A \sqrt{\frac{f_1 f_3}{f_2 f_4}} \eta_f \sum_{i=1}^N \sum_{j=1}^M a_i w \left(\frac{x f_1 f_3}{f_2 f_4} + \lambda \Delta \mathcal{F}_j \frac{f_1 f_3}{f_2 v_a} \right) \exp \left[-j2\pi f_i \frac{f_1 f_3 x}{f_2 f_4 v_a} \right] \cdot b_j \exp[j(\phi_j + \Delta \Phi_{ij})] \exp \left[j2\pi (\mathcal{F}_j + f_i) \left(t - \frac{T}{2} \right) \right]. \quad (4-33)$$

It is instructive at this point to compare Equations 4-33 and 4-24. We see that these two detector illuminations:

1. Differ in position by an amount $\lambda \Delta \mathcal{F}_j \frac{f_4}{v_a}$,
2. Differ in temporal modulation by the signal modulation given in Equation 4-26, and
3. Have a tap position and signal frequency offset dependent phase shift of the temporal modulation.

Number 3 above is key to the delay line properties of the system. Note that if $\Delta\mathcal{T}_i$ is fixed, the phase delay is a linear function offset of tap position, as it should be. Also, a constant delay will result in a phase shift that is linear with signal frequency. Therefore, it appears that the linear phase given in Equation 4-32 corresponds to the time delay of the signal. This does not actually occur, as will be described in Subsection 4.3.1.7.

4.3.1.4 Signal Beam Path: Undiffracted Beam

The undiffracted beam from the AOTDL will be identical to the reference beam in the other path except for the positional offset introduced by the tilted mirror. This is equivalent to the signal beam mathematics with $\Delta\mathcal{T}_i$ replaced by \mathcal{T}_c . The undiffracted beam is therefore written as:

$$u(t, x) = A \sqrt{\frac{f_1 f_3}{f_2 f_4}} \eta^{1/2} \left(1 - \eta_f^2 \sum_{j=1}^M b_j^2 \right)^{1/2} w \left(\frac{x f_1 f_3}{f_2 f_4} + \lambda \mathcal{T}_c \frac{f_1 f_3}{f_2 v_a} \right) \cdot \sum_{i=1}^N a_i \exp \left[-j 2 \pi f_i \frac{f_1 f_3 x}{f_2 f_4 v_a} \right] \exp [j \Delta \Phi'_{ij}] \exp \left[j 2 \pi f_i \left(t - \frac{T}{2} \right) \right] \quad (4-34)$$

where $\Delta \Phi'_{ij}$ is given by Equation 4-33 with $\Delta\mathcal{T}_i$ replaced by \mathcal{T}_c .

4.3.1.5 The Detected Heterodyned Signal

The detected signal for the three incident amplitude waves is given by the square-law summation:

$$d(t) = \int_{-L/2}^{L/2} |f(t, x) + s(t, x) + u(t, x)|^2 dx \quad (4-35)$$

where L is the size of the detector, and the three signals are given in Equations 4-24, 4-33, and 4-34. This signal can be expanded as:

$$d(t) = \int_{-L/2}^{L/2} [|f(t, x)|^2 + |s(t, x)|^2 + |u(t, x)|^2 + 2 \operatorname{Re} \{ f^*(t, x) s(t, x) \} + 2 \operatorname{Re} \{ f^*(t, x) u(t, x) \} + 2 \operatorname{Re} \{ s^*(t, x) u(t, x) \}] dx. \quad (4-36)$$

The fourth term contains the desired output information at the IF, \mathcal{T}_c . Note that the first, second, third, and fifth terms all represent biases that are temporally at dc, and thus can be filtered out after detection using a BPF centered at the signal IF. The form of the desired signal output is first derived and then used to calculate the form of the sixth term.

The term containing the desired output signal is written as:

$$\begin{aligned}
 d_4(t) &= \int_{-L/2}^{L/2} 2\text{Re} \{ f^*(t,x) s(t,x) \} dx \\
 &= 2A^2 \frac{f_1 f_3}{f_2 f_4} \eta_f^{3/2} \int_{-L/2}^{L/2} \text{Re} \left\{ w \left(\frac{x f_1 f_3}{f_2 f_4} \right) \sum_{i=1}^N a_i \exp \left[j 2 \pi f_i \frac{f_1 f_3 x}{f_2 f_4 v_a} \right] \exp \left[-j 2 \pi f_i \left(t - \frac{T}{2} \right) \right] \right. \\
 &\quad \cdot \sum_{k=1}^N \sum_{j=1}^M a_k w \left(\frac{x f_1 f_3}{f_2 f_4} + \lambda \Delta \mathcal{F}_i \frac{f_1 f_3}{f_2 v_a} \right) \exp \left[-j 2 \pi f_k \frac{f_1 f_3 x}{f_2 f_4 v_a} \right] b_j \\
 &\quad \left. \cdot \exp [j (\phi_j + \Delta \Phi_{kj})] \exp [j 2 \pi (\mathcal{F}_j + f_k) (t - \frac{T}{2})] dx \right\}.
 \end{aligned} \tag{4-37}$$

This equation consists of the product of two summations, one over tap position i and the other over both tap position k and signal frequency component j . This will result in products for which i in the first sum equals i in the second sum, and for which i is not the same as k in either sum. The case for which $i=k$ is the desired case, whereas the cross-terms result in undesired harmonics of the input signal offset in frequency.

Consider $i = k$ in both summations written as:

$$\begin{aligned}
 d_4(t; i=k) &= 2A^2 \frac{f_1 f_3}{f_2 f_4} \eta_f^{3/2} \int_{-L/2}^{L/2} \text{Re} \left\{ \sum_{i=1}^N \sum_{j=1}^M w \left(x \frac{f_1 f_3}{f_2 f_4} \right) w \left(x \frac{f_1 f_3}{f_2 f_4} + \lambda \Delta \mathcal{F}_i \frac{f_1 f_3}{f_2 v_a} \right) \right. \\
 &\quad \left. \cdot a_i^2 b_j \exp [j (\phi_j + \Delta \Phi_{ij})] \exp [j 2 \pi \mathcal{F}_j (t - \frac{T}{2})] dx \right\}.
 \end{aligned} \tag{4-38}$$

From linearity, the integral of the real part of a signal is equal to the real part of the integral, and the integral of the sum is equal to the sum of the integral. Therefore Equation 4-38 can be rewritten to yield the desired signal output:

$$\begin{aligned}
 d_4(t; i=k) &= 2A^2 \frac{f_1 f_3}{f_2 f_4} \eta_f^{3/2} \text{Re} \left\{ \eta_f \sum_{i=1}^N \sum_{j=1}^M (a_i)^2 b_j \exp [j (\phi_j + \Delta \Phi_{ij})] \right. \\
 &\quad \left. \cdot \exp [j 2 \pi \mathcal{F}_j (t - \frac{T}{2})] \int_{-L/2}^{L/2} w \left(\frac{x f_1 f_3}{f_2 f_4} \right) w \left(x \frac{f_1 f_3}{f_2 f_4} + \lambda \Delta \mathcal{F}_i \frac{f_1 f_3}{f_2 v_a} \right) dx \right\}.
 \end{aligned} \tag{4-39}$$

For each tap position i , the appropriate delayed version of the signal (the delay is due to the phase term $\Delta\Phi_{ij}$), can be reconstructed multiplied by the square of the tap amplitude, and weighted with the integral shown, which is dependent on the signal frequency.

The term for which the i 's are not equal is given by the general form in Equation 4-37. These cross- terms are due to the interference of one tapped signal output with the undiffracted beam for a neighboring tap. For this case, the equation can be written to express the undesired cross terms as:

$$d_4(t; i \neq k) = 2A^2 \frac{f_1 f_3}{f_2 f_4} \eta_i^{3/2} \operatorname{Re} \left\{ \sum_{i=1}^N \sum_{j=1}^M \sum_{k=1}^N a_i a_k b_j \exp[j(\phi_j + \Delta\Phi_{kj})] \right. \\ \cdot \exp \left[j2\pi (\mathcal{F}_j + f_k - f_i) \left(t - \frac{T}{2} \right) \right] \int_{-L/2}^{L/2} w \left(\frac{x f_1 f_3}{f_2 f_4} \right) w \left(\frac{x f_1 f_3}{f_2 f_4} + \lambda \Delta \mathcal{F}_j \frac{f_1 f_3}{f_2 v_a} \right) \\ \cdot \exp \left[j2\pi (f_i - f_k) \frac{f_1 f_3 x}{f_2 f_4 v_a} \right] dx \Bigg\}. \quad (4-40)$$

The undesired signal output is at a carrier frequency offset from the input signal carrier frequency by an amount equal to the difference of the tap Doppler offsets. Therefore, this carrier frequency will fall within the system pass band if the taps are closely spaced. This term is weighted by the integral, which can be viewed as the integral over a limited detector extent of the product of offset AOSLM imaged apertures. Assume for simplicity that the product of the weighting functions windowed by the detector aperture is a rect function, which assumes total overlap on the detector which is most likely not the case. Then Equation 4-40 can be expressed as (Reference 20):

$$d_4(t; i \neq k) = 2A^2 \frac{f_1 f_3}{f_2 f_4} \eta_i^{3/2} \operatorname{Re} \left\{ \sum_{i=1}^N \sum_{j=1}^M \sum_{k=1}^N a_i a_k b_j \exp[j(\phi_j + \Delta\Phi_{kj})] \exp \left[j2\pi (\mathcal{F}_j + f_k - f_i) \left(t - \frac{T}{2} \right) \right] \right. \\ \cdot \int_{-\infty}^{\infty} \operatorname{rect} \left(\frac{x}{L} \right) \exp \left[j2\pi (f_i - f_k) \frac{f_1 f_3 x}{f_2 f_4 v_a} \right] dx \Bigg\} \quad (4-41)$$

which reduces to

$$d_4(t; i \neq k) = 2A^2 \frac{f_1 f_3}{f_2 f_4} \eta_i^{3/2} \operatorname{Re} \left\{ \sum_{i=1}^N \sum_{j=1}^M \sum_{k=1}^N a_i a_k b_j \exp[j(\phi_j + \Delta\Phi_{kj})] \exp \left[j2\pi (\mathcal{F}_j + f_k - f_i) \left(t - \frac{T}{2} \right) \right] \right. \\ \cdot L \operatorname{sinc} \left[L (f_i - f_k) \frac{f_1 f_3}{f_2 f_4 v_a} \right] \Bigg\} \quad (4-42)$$

where $\text{sinc}(\beta) = \sin\pi\beta/\pi\beta$. As an example of the effect of this equation, the frequency separation required to reach the first null of the sinc function, which occurs for $\beta=1$, is calculated. For representative focal lengths $(f_1, f_2, f_3, f_4) = (.5, .05, .3, .3)$, detector size $L=1$ mm, and $v_a = 4200$ m/s, then $f_i - f_k = 420$ kHz. Observe that the larger the detector, the closer the tap frequencies.

These cross-terms are due to the interference of different tap positions with each other, and are due in part to the spatial coherence of the tap input (all the light comes from a single laser). CPT Keefer's investigation of laser diode array inputs to the AOTDL would be a potential solution to this problem. If the independently modulated lasers in this array are spatially incoherent, then adjacent taps will not interfere with each other. The possibility of driving such a laser diode array with the output of a photodiode array/integrator would potentially be a very attractive alternative to the AOSLM approach when considering the cross-terms.

Now consider term six in Equation 3-36 due to the interference of the undiffracted and diffracted beams from the signal path. This term can be written as:

$$\begin{aligned}
 d_6(t) &= \int_{-L/2}^{L/2} 2\text{Re} \{ s^*(t, x) u(t, x) \} dx \\
 &= 2A^2 \frac{f_1 f_3}{f_2 f_4} \eta_i^{3/2} \left(1 - \eta_i^2 \sum_{j=1}^M b_j^2 \right)^{1/2} \int_{-L/2}^{L/2} \text{Re} \left\{ \sum_{i=1}^N \sum_{j=1}^M a_i w \left(\frac{x f_1 f_3}{f_2 f_4} + \lambda \Delta \mathcal{T}_i \frac{f_1 f_3}{f_2 v_a} \right) \right. \\
 &\quad \cdot \exp \left[j 2 \pi f_i \frac{f_1 f_3 x}{f_2 f_4 v_a} \right] b_j \exp [-j (\phi_j + \Delta \Phi_{ij})] \exp \left[-j 2 \pi (\mathcal{T}_j + f_j) \left(t - \frac{T}{2} \right) \right] \sum_{k=1}^N \\
 &\quad \cdot a_k w \left(\frac{x f_1 f_3}{f_2 f_4} + \lambda \mathcal{T}_c \frac{f_1 f_3}{f_2 v_a} \right) \exp \left[-j 2 \pi f_k \frac{f_1 f_3 x}{f_2 f_4 v_a} \right] \exp [j \Delta \Phi'_{kj}] \exp \left[j 2 \pi f_k \left(t - \frac{T}{2} \right) \right] dx \Big\}.
 \end{aligned} \tag{4-43}$$

Once again, there are two cases depending on whether $i = k$ or $i \neq k$. Consider only the general case, which includes the special case of $i=k$, for which:

$$\begin{aligned}
 d_6(t) &= 2A^2 \frac{f_1 f_3}{f_2 f_4} \eta_i^{3/2} \left(1 - \eta_i^2 \sum_{j=1}^M b_j^2 \right)^{1/2} \text{Re} \left\{ \sum_{i=1}^N \sum_{j=1}^M \sum_{k=1}^N a_i a_k b_j \exp [-j (\phi_j + \Delta \Phi_{ij})] \right. \\
 &\quad \cdot \exp \left[-j 2 \pi (\mathcal{T}_j + f_i - f_k) \left(t - \frac{T}{2} \right) \right] \int_{-L/2}^{L/2} w \left(\frac{x f_1 f_3}{f_2 f_4} + \lambda \Delta \mathcal{T}_i \frac{f_1 f_3}{f_2 v_a} \right) w \left(\frac{x f_1 f_3}{f_2 f_4} + \lambda \mathcal{T}_c \frac{f_1 f_3}{f_2 v_a} \right) \\
 &\quad \cdot \exp \left[j 2 \pi (f_i - f_k) \frac{f_1 f_3 x}{f_2 f_4 v_a} \right] dx \Big\}.
 \end{aligned} \tag{4-44}$$

For the system parameters of our hardware implementation, the physical separation between the two weighting functions in the integral is larger than their width, i.e., the two terms appear separated at the detector. As an example, for the focal lengths and velocity above, $(\Delta f_i, f_c) = (5\text{MHz}, 40\text{MHz})$ and a wavelength of 532 nm, the separation is given as 13.3 mm. Thus, no interference occurs for this term.

In summary, the only terms that impact the output of the tapped delay line filter are the signal term and cross-terms in Equations 4-39 and 4-40. The detected cross-terms will be suppressed as the tap frequency separation increases and as the detector size is reduced.

4.3.1.6 Interferometric Architecture Experimental Results

A single-channel AOTDL architecture was fabricated according to the theory described above. This system operated with the existing AO cells and at a 40-MHz IF. Initial detector outputs were very noisy, and had low-frequency modulation imposed on the desired output at 40-MHz. This low-frequency modulation was due to the interference of the high-frequency terms with each other to induce baseband modulations. A 40-MHz BPF with a bandwidth of 3 MHz was inserted after amplification to greatly improve the output signal. There was no noticeable difference when this filter was placed before the amplifier.

Previous implementations were not set up to achieve the imaging and Fourier transform operations described above for lenses L1 through L4, although they approximated this condition. The system was carefully realigned to achieve this operation, with new lenses being inserted where appropriate. A 1-in. aperture collimation tester was employed to accurately collimate the system. It was recommended that a cemented doublet be employed after the pinhole in the initial filtering and beam expanding stage to reduce aberrations. This greatly improved the collimation performance. All plano-convex lenses were oriented so their planar side faced the converging or diverging part of the beam. Under these conditions, an image of the AOSLM was formed on the detector. The size of this image was changed by adjusting the aperture at the AOSLM input. A small spot was formed in the AOTDL, although this spot was often distorted, most likely due to aberrations primarily induced by the short focal length lens L2. No attempt was made to modify the apodization function of the AOSLM as described above in the mathematical development. This apodization would result in smaller tap spots in the AOTDL and generally improve the performance of the system.

The alignment of the Mach-Zehnder interferometer was critical. Initially, the noncommon path included the lens and spatial filter slit after the AOTDL, used previously to remove the undiffracted beam, and lens L3. These components were set outside the interferometer, and it was realized at this time that filtering the undiffracted beam was unnecessary. Every attempt was made to reduce the size of the interferometer, greatly enhancing the stability, which was quite good for a system employing tilt tables and adjustable mirrors. However, during testing of the system's operation, it was discovered that the phase of

the output signal did not follow the tap position (as selected by the AOTDL) as expected. Although many modifications were attempted in the geometry of the interferometer, the desired phase behavior was not achieved. We suggested the addition of a holographic grating in the same location as the AOTDL but in the reference path, allowing a symmetric geometry to be obtained and eliminating the change in path length difference. Two holographic gratings were made at the Photonics Center by Stephen Kupiak of the University of Alabama in Huntsville, but efficiency was not very high and time did not permit a full evaluation of the system after insertion of these gratings. Subsection 4.3.1.7 develops the source of this anomalous phase behavior, and a modified architecture that overcomes this limitation is the subject of Subsection 4.3.2.

The output at the 40-MHz IF was qualitatively compared to the AOTDL input, and it was found that there was very little distortion of the input signal. *Figure 4-24* shows such an output for a DSB-SC modulation of the 40-MHz carrier with a 1-MHz tone. Although this plot, created on 1 August 1991, shows a 2-mV/div scale for the optical signal, outputs of greater than 100 mV were typically achieved in the following weeks. The canceled signal is also shown in this figure. The cancellation of the signal at the IF is critical to meeting the needs of the radar system, but this requirement introduces other real-world complications not present with the previous base-band implementations. Because the signals are being subtracted on the carrier, the carriers must be aligned in phase, in addition to the alignment of the envelope modulations. If the tap position is moved to achieve a 180° phase shift of the carrier, no noticeable change in the position of the envelope will result, but the cancellation will go from good cancellation depth to constructive interference (a doubling of the signal amplitude). Therefore, it is clear that precise control of the tap position is required. It also becomes clear why the phase is important in the cancellation. If the auxiliary channel of a single-channel system is phase shifted (a phase shift of the carrier but no time shift of the envelope) relative to the main channel, then to get the best cancellation, the envelopes must be aligned and the phase shift must be compensated.

Although the frequency response (magnitude and phase) of the system was not fully characterized, the magnitude of the output was measured as a function of tap position (as selected by the AOSLM) for a given alignment condition and a single-tone input to the AOTDL. The results of this are shown in *Table 4-3*, where it is seen that the magnitude response is very flat over the span of AOSLM input frequencies. This is especially surprising considering the composite effects of the AOSLM frequency response, the AOTDL attenuation properties, and the heterodyne efficiency of the process. Although this result is very promising, this measurement was made for one condition of system alignment, and may be different when the system is optimally aligned for magnitude and phase response.

Finally, the generation of the undesired cross-terms (described by Equation 4-40) was qualitatively examined and found to adhere approximately to theory. The AOSLM input consisted of a DSB-SC modulation of a 40-MHz carrier with a tone. This tone was decreased in frequency from greater than

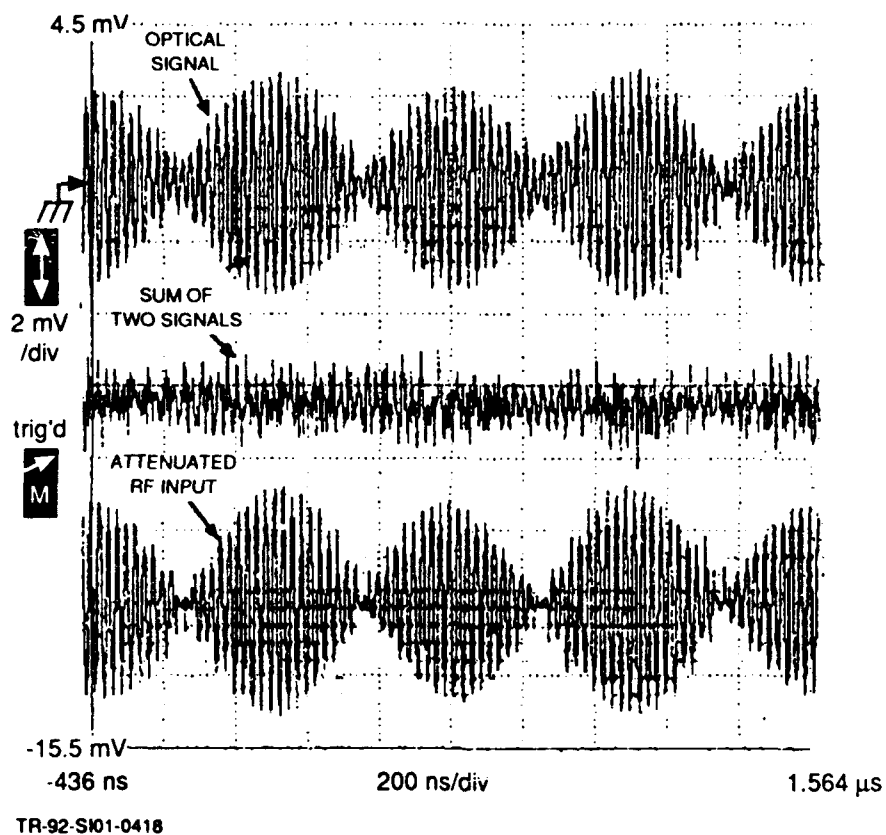


Figure 4-24. Representative Tapped Delay Line Signals

Table 4-3. Amplitude Response Versus Tap Position

f_{tap} (MHz)	P_{detected} (dBm) (Measured by Oscilloscope)
52.0	-17.2
51.5	-13.1
51.0	-12.1
50.5	-11.0
50.0	-10.7
49.5	-10.3
49.0	-9.9
48.5	-9.9
48.0	-9.6
47.5	-9.2
47.0	-8.9
46.5	-8.9
46.0	-8.5
45.5	-8.5
45.0	-8.5
44.5	-8.5
44.0	-8.1
43.5	-8.1
43.0	-8.1
42.5	-8.1
42.0	-8.1
41.5	-8.1
41.0	-8.5
40.5	-8.5
40.0	-8.5
39.5	-8.5
39.0	-8.5
38.5	-8.5
38.0	-8.5
37.5	-8.9
37.0	-8.9
36.5	-9.2
36.0	-9.2
35.5	-9.2
35.0	-9.6
34.5	-9.6
34.0	-9.6
33.5	-9.9
33.0	-9.9
32.5	-10.3
32.0	-10.7
31.5	-11.0
31.0	-11.0
30.5	-11.4
30.0	-11.7
29.5	-12.1
29.0	-12.4
28.5	-12.8
28.0	-13.1

5 MHz as the detector output was examined on the spectrum analyzer. As the tone approached 0.5 to 1.0 MHz, terms at the difference frequencies $f_j + f_k - f_i$ in Equation 4-40 were apparent. These terms grew in magnitude as the tone was further decreased, as expected. No characterization of the effect of detector size on cross-term suppression was performed.

4.3.1.7 Interferometric Architecture Limitations

When this Mach-Zehnder architecture was developed, it was experimentally observed that it was very difficult to make the signal information delay the appropriate amount when the tap position was adjusted by tuning the input to the AOSLM. In fact, it appeared that when the system was in its best state of alignment, the carrier was stationary even when the modulation envelope moved at the appropriate rate relative to the reference signal (RF input to the AOTDL). When the AOTDL was moved relative to the tap position, true time delay was consistently observed. This implied that moving the AOTDL relative to the tap was significantly different from moving the tap relative to the AOTDL.

The arrangement shown in **Figure 4-25** is first considered. In this figure, a single frequency is input to the AOTDL and a plane wave illumination is provided. A reference beam is made to be coincident with the diffracted beam, in a similar fashion to the reference beam shown in **Figure 4-23**. The diffracted beam and a small reference beam in this case are collimated and colinear, therefore having a constant phase front across the overlapping beams. Placing a small detector in the beam and moving this detector orthogonal to the propagation direction (while at the same time moving the reference beam to overlap on the detector) results in no relative position-dependent phase shift of the heterodyned signal. This is equivalent to tapping the AOTDL at different positions and observing the output of the heterodyne process relative to the RF input to the AOTDL.

Next, an identical geometry was considered and the AOTDL was moved, but the detector position and reference beam position were fixed. As for a moving grating, the phase of the output will change relative to the input as the AOTDL is moved. One conceptual way of observing this phase shift is to consider the imaging of a grating. As the grating is moved, the image will move; therefore, a small detector will see the light go from dark to bright as the fringes pass by. For a heterodyne system, this is equivalent to seeing the phase of the heterodyned output change linearly with AOTDL position.

The case of concern (moving tap position) can be mathematically described with a simple example of a pulsed carrier. The pulse input is described as:

$$s(t) = p_\tau(t) \exp[j2\pi f_c t] \quad (4-45)$$

where τ denotes the pulsewidth and f_c is the carrier frequency. Assuming that $t=0$ corresponds to the center of the AOTDL ($x=0$), and T is the AOTDL time aperture, the pulse can be written as:

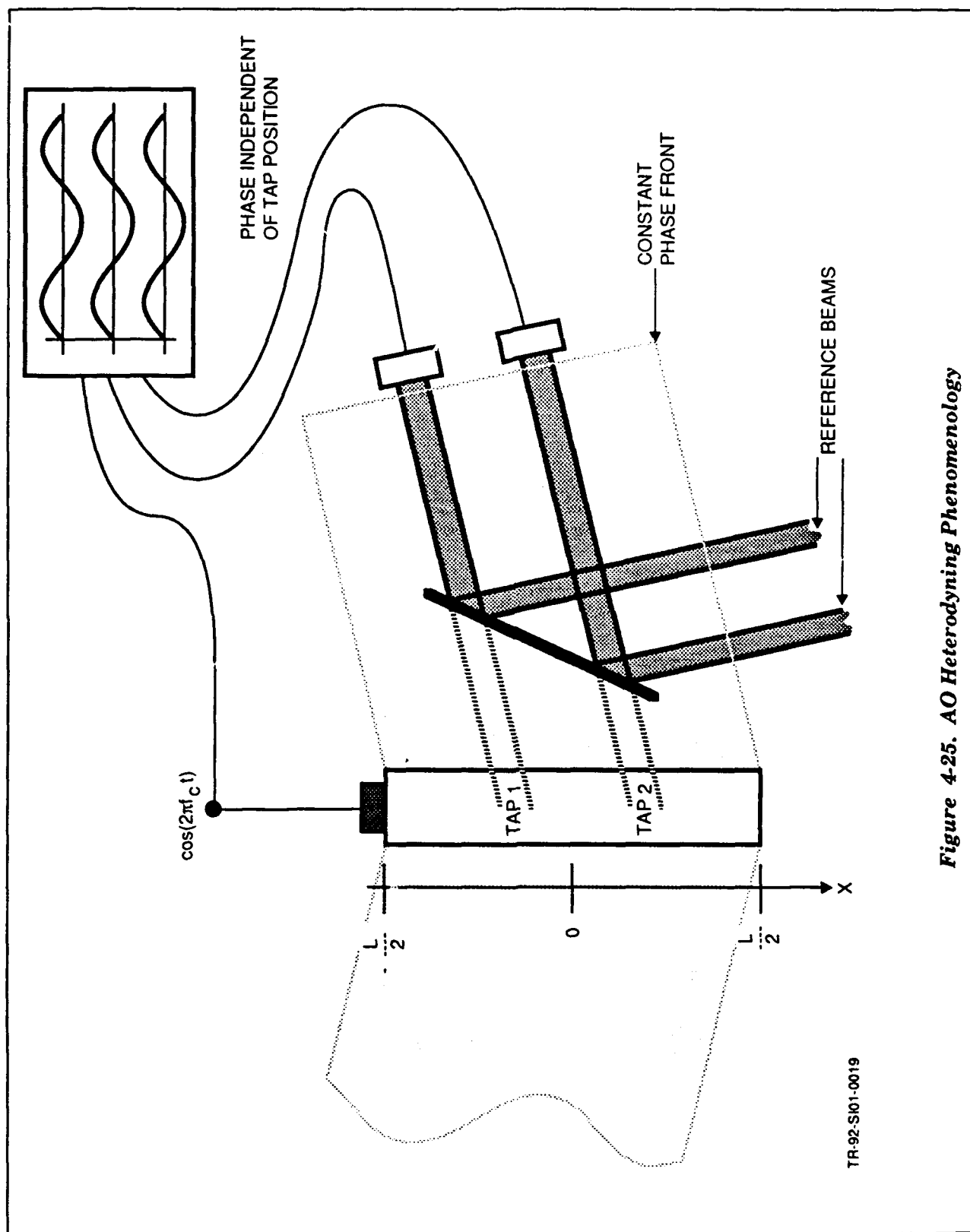


Figure 4-25. AO Heterodyning Phenomenology

$$s\left(t - \frac{T}{2} - \frac{x}{v_a}\right) = p_\tau\left(t - \frac{T}{2} - \frac{x}{v_a}\right) \exp\left[j2\pi f_c\left(t - \frac{T}{2} - \frac{x}{v_a}\right)\right]. \quad (4-46)$$

Adding the reference beam that travels in the same direction as the center frequency to this signal, and heterodyne detecting, an output signal was obtained, given as a function of time and tap position by:

$$\begin{aligned} I(t, x) &= \left| p_\tau\left(t - \frac{T}{2} - \frac{x}{v_a}\right) \exp\left[j2\pi f_c\left(t - \frac{T}{2} - \frac{x}{v_a}\right)\right] + \exp\left[-j2\pi f_c \frac{x}{v_a}\right] \right|^2 \\ &= \text{biases} + 2\text{Re} \left\{ p_\tau\left(t - \frac{T}{2} - \frac{x}{v_a}\right) \exp\left[j2\pi f_c\left(t - \frac{T}{2}\right)\right] \right\}. \end{aligned} \quad (4-47)$$

Now, for $x=0$ (a tap position at the center of the AOTDL), the output is given by:

$$I(t, 0) = \text{biases} + 2\text{Re} \left\{ p_\tau\left(t - \frac{T}{2}\right) \exp\left[j2\pi f_c\left(t - \frac{T}{2}\right)\right] \right\} \quad (4-48)$$

and for $x = -\frac{L}{2}$ (note that $L = v_a T$), the output is given by:

$$I\left(t, \frac{T}{2}\right) = \text{biases} + 2\text{Re} \left\{ p_\tau(t) \exp\left[j2\pi f_c\left(t - \frac{T}{2}\right)\right] \right\}. \quad (4-49)$$

Therefore, two tap positions see the envelope of the waveform at the different times but the carrier phase relationship to the pulse is not constant. This resolves the apparent paradox observed in the hardware implementation, namely that the envelope of the signal moved appropriately but the carrier moved relative to the envelope and even appeared stationary.

It is interesting at this point to refer back to the mathematics of the Mach-Zehnder architecture. A key term to be analyzed is the tap position and AOTDL frequency-dependent phase shift of the heterodyned signal. This is defined in Equation 4-32 as:

$$\Delta\Phi_{ij} = -2\pi f_i \frac{\lambda \Delta f_j f_1 f_3}{f_2 v_a^2} \quad (4-50)$$

where f_i and Δf_j are the AOSLM input frequency (defining the tap position) and frequency offset of the signal from the AOTDL center frequency. Note that the AOTDL center frequency is defined for this case as the frequency that exactly aligns with the reference beam of the Mach-Zehnder interferometer. This was initially interpreted as the desired phase shift, which is linear in frequency (thought to result in true time delay) and linear in tap position. The key problem with this interpretation is that the phase shift is a function of the

difference frequency, Δf_i , and not the AOTDL input frequency. For an input equal to the center frequency, the phase shift is completely independent of tap position (note the similarity to the argument in reference to **Figure 4-25**). Equation 4-50 above preserves the true time-delay of the envelope of the modulation but does not time-delay the carrier.

A straightforward way to mathematically understand this phenomenon is to consider a signal on a carrier:

$$s(t) = a(t) \exp[j2\pi f_c t] \quad (4-51)$$

which has a Fourier transform:

$$S(f) = A(f - f_c). \quad (4-52)$$

A true time-delay of $s(t)$ is written as:

$$s(t - \tau) = a(t - \tau) \exp[j2\pi f_c (t - \tau)] \quad (4-53)$$

which has a Fourier transform:

$$S(f, \tau) = \exp[-j2\pi f \tau] A(f - f_c) \quad (4-54)$$

By imposing a linear phase as a function of difference of frequency, as in Equation 4-50, it can now be written:

$$S'(f, \tau) = \exp[-j2\pi \tau (f - f_c)] A(f - f_c) \quad (4-55)$$

which is in the time domain given by:

$$s'(t - \tau) = \exp[j2\pi f_c \tau] a(t - \tau) \exp[j2\pi f_c (t - \tau)] = a(t - \tau) \exp[j2\pi f_c t]. \quad (4-56)$$

The carrier for this case is seen to be stationary with a time-shifted envelope.

To remedy the situation, it can be observed that to convert Δf_i to the AOTDL input frequency a reference beam must be employed that appears to emanate from the tap at an angle equivalent to the undiffracted beam. This is equivalent to shifting the position of the reference beam to align with the undiffracted beam rather than to align with the center frequency beam. Because of this realization, it is apparent that the reference beam is no longer needed and the undiffracted beam can be used instead. This forms the basis of the noninterferometric architecture described in Subsection 4.3.2.

4.3.2 Noninterferometric Architecture Design and Implementation

Several practical issues relate to the use of the undiffracted beam as a reference beam in the AOTDL filter. First, the degree of overlap of the two beams at the detector is very small since the angles at the AOTDL are very large. To remedy this situation, the tap must be made very small, resulting in a larger beam on the detector for better overlap (refer back to Equation 4-44). Secondly, the amplitudes of the diffracted and undiffracted beams are coupled, thus the process is not linear. A technique for achieving both better overlap and less coupling of power between the reference and signal beams is to use an electronic reference. This architecture, which was designed, fabricated, and tested during this effort will now be described. The resulting architecture is similar in layout to prior architectures reported in Reference 1.

The noninterferometric tapped delay line architecture is shown in **Figure 4-26**. The system is equivalent to the interferometric approach shown in **Figure 4-23** with the reference path removed and an electronic reference added. Observe that this architecture is effectively an AO point modulator with a moving tap position.

The mathematics for the noninterferometric architecture closely parallels that of the interferometric architecture.

4.3.2.1 Signal-Carrying Beam and Undiffracted Beam

For the noninterferometric architecture, the signal-carrying beam and the undiffracted beam are identical to those for the interferometric case except that the frequencies are relative to dc and not \mathcal{F}_c . Therefore, the signal-carrying beam can be written as (see Equation 4-33):

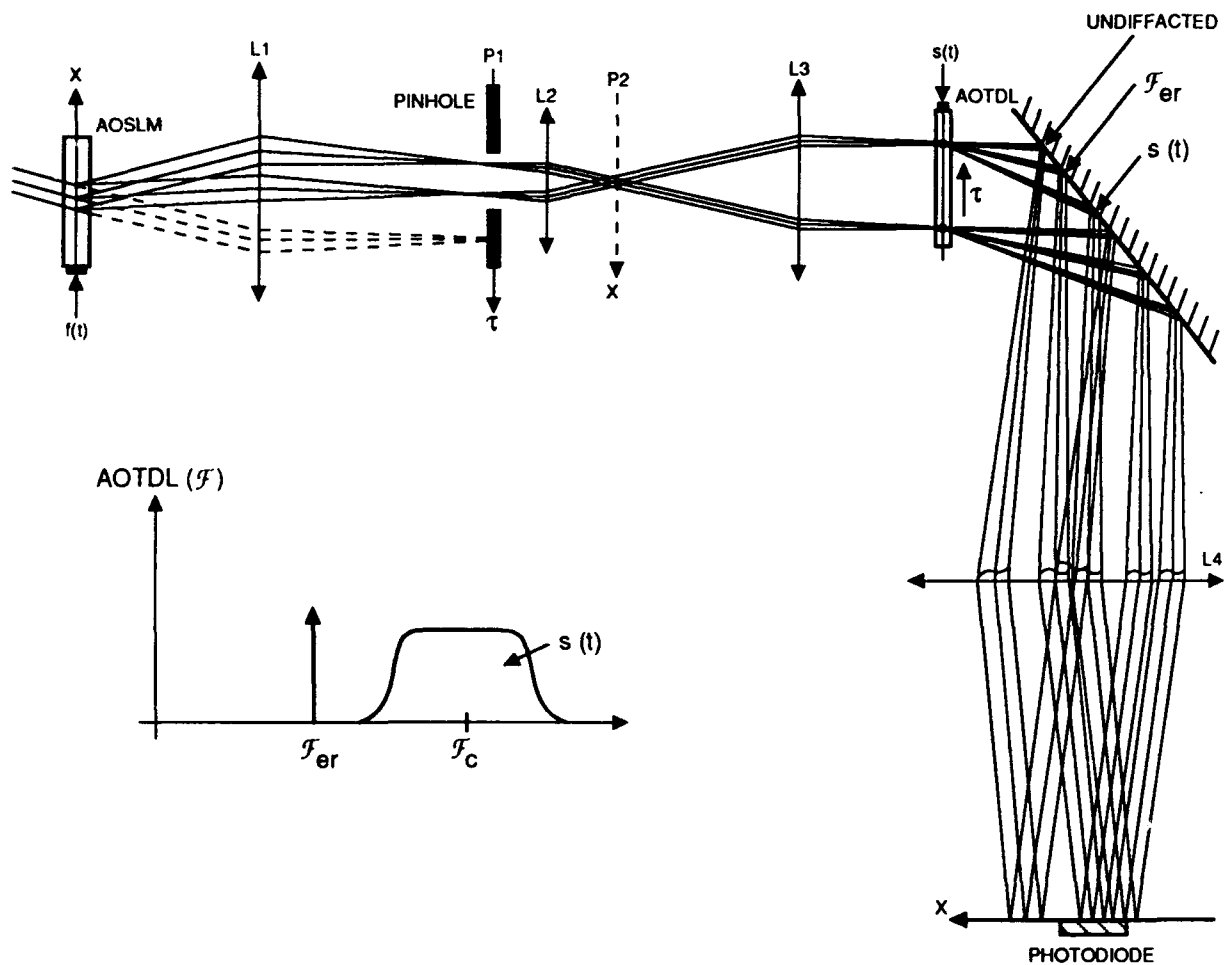
$$s(t, x) = A \sqrt{\frac{f_1 f_3}{f_2 f_4}} \eta_f \sum_{i=1}^N \sum_{j=1}^M a_i w \left(\frac{x f_1 f_3}{f_2 f_4} + \lambda \mathcal{F}_j \frac{f_1 f_3}{f_2 v_a} \right) \exp \left[-j 2 \pi f_i \frac{f_1 f_3 x}{f_2 f_4 v_a} \right] \quad (4-57)$$

$$\bullet b_j \exp [j (\phi_j + \Delta \Phi_{ij})] \exp \left[j 2 \pi (\mathcal{F}_j + f_i) \left(t - \frac{T}{2} \right) \right]$$

where $\Delta \Phi_{ij}$ is now given as:

$$\Delta \Phi_{ij} = -2 \pi f_i \frac{\lambda \mathcal{F}_j f_1 f_3}{f_2 v_a^2} \quad (4-58)$$

Likewise, the undiffracted beam can be written as:



TR-91-PROP-1703A

Figure 4-26. Noninterferometric Tapped Delay Line Architecture

$$u(t,x) = A \sqrt{\frac{f_1 f_3}{f_2 f_4}} \eta_f^{1/2} \left(1 - \eta_f^2 \alpha^2 - \eta_f^2 \sum_{j=1}^M b_j^2 \right)^{1/2} w\left(\frac{x f_1 f_3}{f_2 f_4}\right) \sum_{i=1}^N a_i \cdot \exp\left[-j2\pi f_i \frac{f_1 f_3 x}{f_2 f_4 v_a}\right] \exp\left[j2\pi f_i \left(t - \frac{T}{2}\right)\right] \quad (4-59)$$

where $\Delta\Phi'_{ij} = \mathcal{F}_c = 0$ in Equation 4-34 and α will be defined later. Note that this beam is almost identical to the reference path beam given by Equation 4-24, as it should be.

4.3.2.2 Addition of a Diffracted Electronic Reference Beam

For reasons to be explained below, related to the position offset of the diffracted and undiffracted beams at the photodetector, an electronic reference is applied and given by:

$$r(t) = \alpha \cos[2\pi \mathcal{F}_{er} t] \quad (4-60)$$

This electronic reference beam behaves as the diffracted signal beam given in Equation 4-34; therefore, the electronic reference beam can be written as:

$$r(t,x) = A \sqrt{\frac{f_1 f_3}{f_2 f_4}} \eta_f \sum_{i=1}^N a_i w\left(\frac{x f_1 f_3}{f_2 f_4} + \lambda \mathcal{F}_{er} \frac{f_1 f_3}{f_2 v_a}\right) \exp\left[-j2\pi f_i \frac{f_1 f_3 x}{f_2 f_4 v_a}\right] \cdot \alpha \exp[j\Delta\Phi_{ier}] \exp\left[j2\pi (\mathcal{F}_{er} + f_i) \left(t - \frac{T}{2}\right)\right] \quad (4-61)$$

where $\Delta\Phi_{ier}$ is given by Equation 4-58 with \mathcal{F}_j replaced by \mathcal{F}_{er} .

4.3.2.3 The Detected Heterodyned Signal

The detected signal for the three incident amplitude waves is given by the square-law summation:

$$d(t) = \int_{-L/2}^{L/2} |u(t,x) + s(t,x) + r(t,x)|^2 dx \quad (4-62)$$

where L is the size of the detector and the three signals are given in Equations 4-57, 4-59, and 4-61. This signal can be expanded as:

$$d(t) = \int_{-L/2}^{L/2} [|u(t,x)|^2 + |s(t,x)|^2 + |r(t,x)|^2 + 2\operatorname{Re}\{u^*(t,x)s(t,x)\} + 2\operatorname{Re}\{u^*(t,x)r(t,x)\} + 2\operatorname{Re}\{s^*(t,x)r(t,x)\}] dx. \quad (4-63)$$

The fourth term comes out of the detector after heterodyning at the center frequency, \mathcal{F}_i , whereas the sixth term is at $\mathcal{F}_i - \mathcal{F}_{er}$. Both terms contain the desired output, but to generate the output at the processor IF, the sixth term must be mixed to the IF with the frequency \mathcal{F}_{er} . Note that the first, second, and third terms all represent biases that are temporally at dc, and can be filtered out after detection using a BPF. Likewise, the carrier that is generated by the fifth term at \mathcal{F}_{er} can be removed through filtering. The calculated form of the desired signal output for both the fourth and sixth terms is given below. The term containing the desired output signal at the processor IF is written as:

$$\begin{aligned} d_4(t) &= \int_{-L/2}^{L/2} 2\operatorname{Re}\{u^*(t,x)s(t,x)\} dx \\ &= 2A^2 \frac{f_1 f_3}{f_2 f_4} \eta_i^{3/2} \left(1 - \eta_i^2 \alpha^2 - \eta_i^2 \sum_{j=1}^M b_j^2\right)^{1/2} \int_{-L/2}^{L/2} \operatorname{Re}\left\{w\left(\frac{x f_1 f_3}{f_2 f_4}\right) \sum_{i=1}^N a_i \right. \\ &\quad \cdot \exp\left[j2\pi f_i \frac{f_1 f_3 x}{f_2 f_4 v_a}\right] \exp\left[-j2\pi f_i \left(t - \frac{T}{2}\right)\right] \\ &\quad \cdot \sum_{k=1}^N \sum_{j=1}^M a_k w\left(\frac{x f_1 f_3}{f_2 f_4} + \lambda \mathcal{F}_i \frac{f_1 f_3}{f_2 f_4 v_a}\right) \exp\left[-j2\pi f_k \frac{f_1 f_3 x}{f_2 f_4 v_a}\right] \\ &\quad \left. \cdot b_j \exp[j(\phi_j + \Delta\Phi_{kj})] \exp\left[j2\pi \mathcal{F}_j + f_k \left(t - \frac{T}{2}\right)\right] \right\} dx. \end{aligned} \quad (4-64)$$

This equation consists of the product of two summations, one over tap position i and the other over both a tap position k and signal frequency component j . This results in products for which i in the first sum equals k in the second sum, and for which i is not the same in either sum. The case of $i=k$ is the desired case, whereas the cross-terms result in undesired harmonics of the input signal are offset in frequency.

First consider $i=k$ in both summations:

$$\begin{aligned}
d_4(t; i=k) = & 2A^2 \frac{f_1 f_3}{f_2 f_4} \eta_f^{3/2} \left(1 - \eta_f^2 \alpha^2 - \eta_f^2 \sum_{j=1}^M b_j^2 \right)^{1/2} \int_{-L/2}^{L/2} \\
& \bullet \operatorname{Re} \left\{ \sum_{i=1}^N \sum_{j=1}^M w \left(\frac{x f_1 f_3}{f_2 f_4} \right) w \left(\frac{x f_1 f_3}{f_2 f_4} + \lambda \mathcal{F}_j \frac{f_1 f_3}{f_2 v_a} \right) \right. \\
& \left. \bullet a_i^2 b_j \exp [j(\phi_j + \Delta \Phi_{ij})] \exp \left[j 2 \pi \mathcal{F}_j \left(t - \frac{T}{2} \right) \right] \right\} dx.
\end{aligned} \tag{4-65}$$

From linearity, the integral of the real part of a signal is equal to the real part of the integral, and the integral of the sum is equal to the sum of the integral. Therefore, Equation 4-65 can be rewritten to yield the desired signal output at the processor IF:

$$\begin{aligned}
d_4(t; i=k) = & 2A^2 \frac{f_1 f_3}{f_2 f_4} \eta_f^{3/2} \left(1 - \eta_f^2 \alpha^2 - \eta_f^2 \sum_{j=1}^M b_j^2 \right)^{1/2} \\
& \bullet \operatorname{Re} \left\{ \sum_{i=1}^N \sum_{j=1}^M a_i^2 b_j \exp [j(\phi_j + \Delta \Phi_{ij})] \exp \left[j 2 \pi \mathcal{F}_j \left(t - \frac{T}{2} \right) \right] \right. \\
& \left. \bullet \int_{-L/2}^{L/2} w \left(\frac{x f_1 f_3}{f_2 f_4} \right) w \left(\frac{x f_1 f_3}{f_2 f_4} + \lambda \mathcal{F}_j \frac{f_1 f_3}{f_2 v_a} \right) dx \right\}.
\end{aligned} \tag{4-66}$$

It can be seen that for each tap position i , the appropriate delayed version of the signal has been reconstructed, (the delay is due to the phase term $\Delta \Phi_{ij}$), multiplied by the square of the tap amplitude, and weighted with the integral shown, which is dependent on the signal frequency.

The term for which the i is not equal to k is given by the general form in Equation 4-64. These cross-terms are due to the interference of one tapped signal output with the undiffracted beam for a neighboring tap. For this case, this equation can be rewritten to express the undesired cross-terms as:

$$\begin{aligned}
d_4(t; i \neq k) = & 2A^2 \frac{f_1 f_3}{f_2 f_4} \eta_i^{3/2} \left(1 - \eta_i^2 \alpha^2 - \eta_i^2 \sum_{j=1}^M b_j^2 \right)^{1/2} \operatorname{Re} \left\{ \sum_{i=1}^N \sum_{j=1}^M \sum_{k=1}^N a_i a_k b_j \exp [j(\phi_i + \Delta \Phi_{ki})] \right. \\
& \cdot \exp \left[j2\pi (\mathcal{F}_i + f_k - f_i) \left(t - \frac{T}{2} \right) \right] \int_{-L/2}^{L/2} w \left(\frac{x f_1 f_3}{f_2 f_4} \right) w \left(\frac{x f_1 f_3}{f_2 f_4} + \lambda \mathcal{F}_i \frac{f_1 f_3}{f_2 v_a} \right) \\
& \cdot \exp \left[j2\pi (f_i - f_k) \frac{f_1 f_3 x}{f_2 f_4 v_a} \right] dx \left. \right\}.
\end{aligned} \tag{4-67}$$

The undesired signal output is at a carrier frequency offset from the input signal carrier frequency by an amount equal to the difference of the tap Doppler offsets. Therefore, carrier frequency will fall within the system pass band if the taps are closely spaced in frequency input to the AOSLM. This term is weighted by the integral, which can be viewed as the integral over a limited detector extent of the product of AOSLM-imaged AOSLM apertures.

The sixth term in Equation 4-63, is due to the interference of the electronic reference beam and diffracted signal beam, and can be written as:

$$\begin{aligned}
d_6(t) = & \int_{-L/2}^{L/2} 2 \operatorname{Re} \{ s^*(t, x) r(t, x) \} dx = \int_{-L/2}^{L/2} 2 \operatorname{Re} \{ s(t, x) r^*(t, x) \} dx \\
= & 2A^2 \frac{f_1 f_3}{f_2 f_4} \eta_i^2 \int_{-L/2}^{L/2} \operatorname{Re} \left\{ \sum_{i=1}^N \sum_{j=1}^M a_i w \left(\frac{x f_1 f_3}{f_2 f_4} + \lambda \mathcal{F}_i \frac{f_1 f_3}{f_2 v_a} \right) \exp \left[-j2\pi f_i \frac{f_1 f_3 x}{f_2 f_4 v_a} \right] \right. \\
& \cdot b_j \exp [j(\phi_j + \Delta \Phi_{ij})] \exp \left[j2\pi (\mathcal{F}_j + f_i) \left(t - \frac{T}{2} \right) \right] \sum_{k=1}^N a_k w \left(\frac{x f_1 f_3}{f_2 f_4} + \lambda \mathcal{F}_{er} \frac{f_1 f_3}{f_2 v_a} \right) \\
& \cdot \exp \left[j2\pi f_k \frac{f_1 f_3 x}{f_2 f_4 v_a} \right] \alpha \exp [-j\Delta \Phi_{ker}] \exp \left[-j2\pi (\mathcal{F}_{er} + f_k) \left(t - \frac{T}{2} \right) \right] \left. \right\} dx.
\end{aligned} \tag{4-68}$$

Once again, There are two cases depending on whether $i = k$ or not. For $i=k$:

$$\begin{aligned}
d_6(t; i=k) = & 2A^2 \frac{f_1 f_3}{f_2 f_4} \eta_i^2 \alpha \operatorname{Re} \left\{ \sum_{i=1}^N \sum_{j=1}^M a_i^2 b_j \exp [j(\phi_j + \Delta \Phi_{ij} - \Delta \Phi_{ier})] \exp \left[j2\pi (\mathcal{F}_j - \mathcal{F}_{er}) \left(t - \frac{T}{2} \right) \right] \right. \\
& \cdot \int_{-L/2}^{L/2} w \left(\frac{x f_1 f_3}{f_2 f_4} + \lambda \mathcal{F}_i \frac{f_1 f_3}{f_2 v_a} \right) w \left(\frac{x f_1 f_3}{f_2 f_4} + \lambda \mathcal{F}_{er} \frac{f_1 f_3}{f_2 v_a} \right) dx \left. \right\}.
\end{aligned} \tag{4-69}$$

Differences between this term and Equation 4-65 are the more substantial overlap of the two window functions, providing more heterodyne efficiency (motivation for using an electronic reference), a carrier

frequency now equal to $f_j - f_{er}$ rather than the system IF, and an additional linear phase term, $\Delta\Phi_{ier}$. To obtain this desired term at the IF, mixing is done after detection with the electronic reference signal.

Next consider the general case of $i \neq k$ and write:

$$\begin{aligned}
 d_6(t; i \neq k) = & 2A^2 \frac{f_1 f_3}{f_2 f_4} \eta_i^2 \alpha \operatorname{Re} \left\{ \sum_{i=1}^N \sum_{j=1}^M \sum_{k=1}^N a_i a_k b_j \exp [j(\phi_j + \Delta\Phi_{ij} - \Delta\Phi_{ker})] \right. \\
 & \bullet \exp \left[j2\pi (f_j - f_{er} + f_i - f_k) \left(t - \frac{T}{2} \right) \right] \\
 & \bullet \int_{-L/2}^{L/2} w \left(\frac{x f_1 f_3}{f_2 f_4} + \lambda f_j \frac{f_1 f_3}{f_2 v_a} \right) w \left(\frac{x f_1 f_3}{f_2 f_4} + \lambda f_{er} \frac{f_1 f_3}{f_2 v_a} \right) \\
 & \bullet \exp \left[j2\pi (f_k - f_i) \frac{f_1 f_3 x}{f_2 f_4 v_a} \right] dx \left. \right\}.
 \end{aligned} \tag{4-70}$$

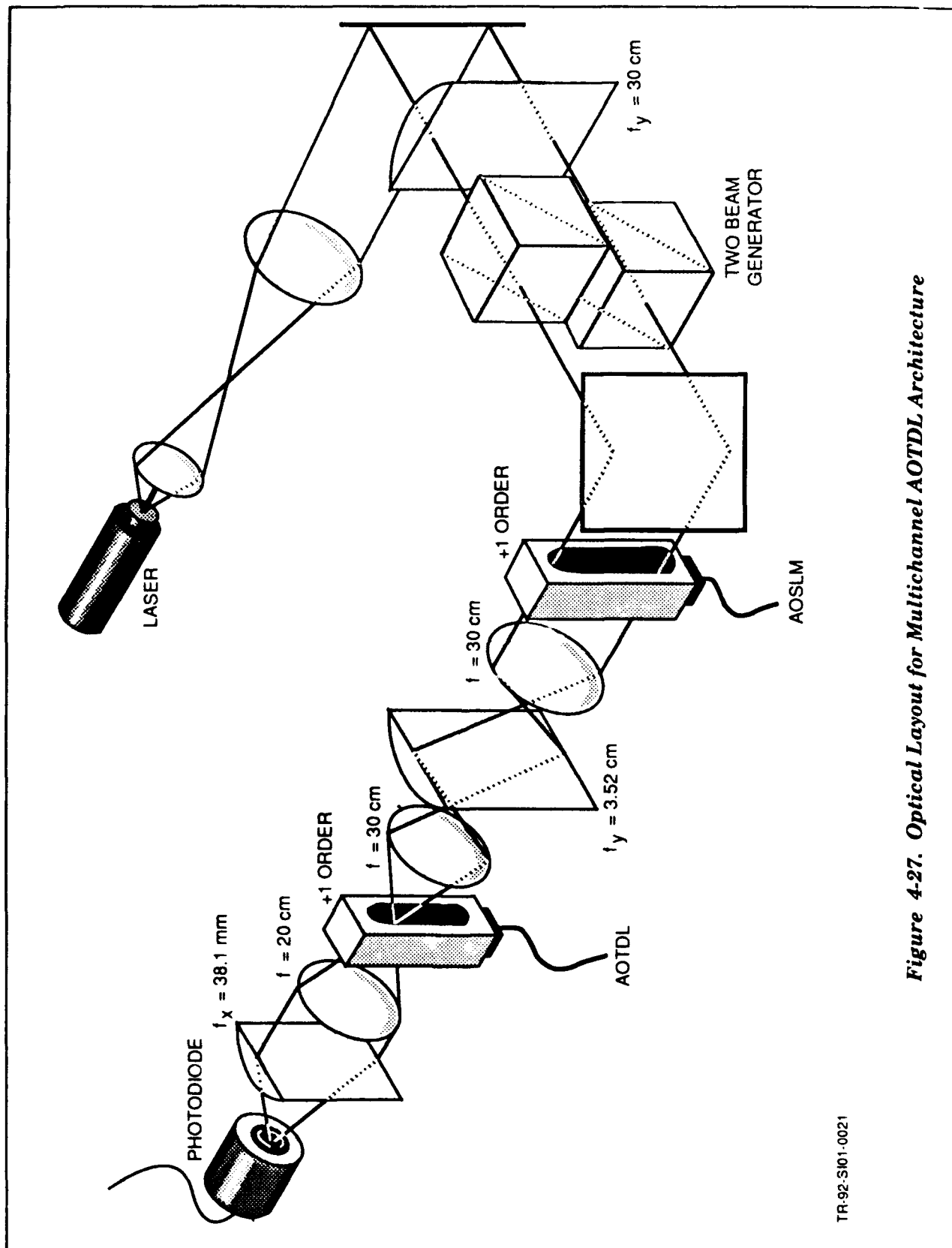
These terms result in undesired cross-terms as for the interferometric case.

4.3.2.4 Experimental Results and Characterization

On-site at the Photonics Laboratory, the interferometric architecture was modified to create the above-described noninterferometric architecture, and the electronic reference was inserted. This subsection documents the hardware measurements made. **Figures 4-27 and 4-28** show the optical and electronic systems as configured in the laboratory for 2-channel operation.

In addition to configuring the system for noninterferometric operation, multichannel AO cells were integrated into the system and the appropriate lenses were inserted between the AOSLM and the AOTDL. The use of multichannel devices requires that the output of the AOSLM be transformed, as before, in the direction of acoustic propagation, but in addition, the orthogonal direction must be imaged to provide multiple SLM channel illumination of the multiple channels of the AOTDL. A number of configurations were attempted for this case and the most desired approach will now be described. With equal spacing of acoustic channels for the two AO cells selected, the imaging must be 1:1 in the direction orthogonal to the acoustic propagation direction. For the direction of acoustic propagation, the system must Fourier transform the AOSLM output and display this across a 5- μ s aperture at the AOTDL. For the velocity of the AOTDL, $v_a = 4200$ m/s, this corresponds to an aperture, Δx , of 2.1 cm. The spread in frequencies in the AOSLM is nominally set at 40 MHz, resulting in a spatial frequency difference, Δf_x , of 9523.8 cycles/m. Using the equation:

$$\Delta x = \Delta f_x \lambda f \tag{4-71}$$



TR-92-S101-0021

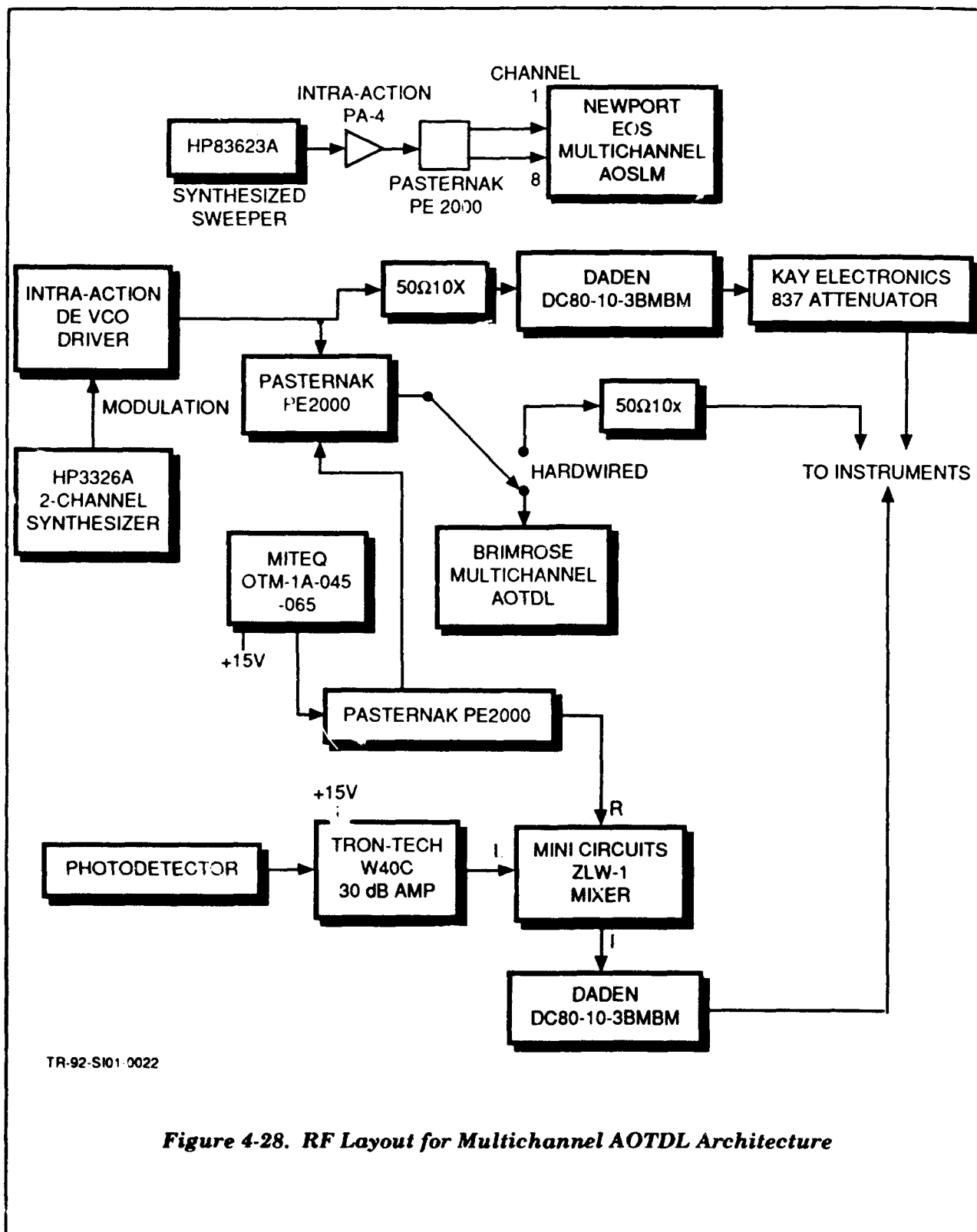


Figure 4-28. RF Layout for Multichannel AOTDL Architecture

it is determined that the focal length requirement is $f=4.145$ m. An intermediate Fourier transform can be formed and imaged this with magnification to satisfy the equation $M_x f = 4.145$ m. As an example, f_1 and f_3 can be made to equal 300 mm, with the cylindrical lens having a focal length, $f_y = 37.76$ mm, to achieve the desired results. For the system fabricated in the laboratory, this condition was approximated by having f_1 and f_3 equal to 300 mm, with the cylindrical lens having a focal length, $f_y = 35.2$ mm.

Three examples of spectrum analyzer outputs for the system are shown in **Figures 4-29 through 4-31**. In each of these figures, the RF input into the AOTDL and the optical output due to the beating of the electronic reference beam with the signal beam and subsequent mixing back to the system IF are shown with the cancelled output. The three input modulations consisted of a single tone, a two-tone waveform with separation of 3.2 MHz, and one with separation 10.0 MHz.

Figure 4-32 (a) through (f) shows the spectrum analyzer display of the AOTDL input (a tone at 77 MHz with an electronic reference at 63.6 MHz) and the output of the system for AOSLM tap frequencies of 60, 70, 79, 90, and 100 MHz. A second example is shown in **Figure 4-33 (a) through (c)**. It was of interest to trace the origin of the different spurious tones present in **Figure 4-33(b)** to isolate them and reduce their impact.

The output of the desired term from the photodiode is given by the difference frequency, $f_{\text{AOTDL}} - f_{\text{ER}}$, for a signal input consisting of a single tone, f_{AOTDL} . The output of the mixer, having f_{ER} as its input, is given by two tones at f_{AOTDL} (the desired output) and $2f_{\text{ER}} - f_{\text{AOTDL}}$. It was also found that a portion of the f_{AOTDL} signal reached the mixer through the two Pasternak PE 2000 splitters shown in **Figure 4-33(c)**. This resulted in the generation of mixer outputs at f_{ER} and $2f_{\text{AOTDL}} - f_{\text{ER}}$ and also results in the undesirable cross-talk that enters the photodetector output when no light is incident. All of these spurious signals have been minimized by careful shielding and the addition of a filter that blocks the feedthrough of the f_{AOTDL} signal to the mixer. The final measurements that were made utilized an HP network analyzer configured for S_{12} parameter measurement as shown in **Figure 4-34**. This source was swept across a wide bandwidth to measure the frequency response of the system across the 75 to 85 MHz pass band. Two examples of the response are shown in **Figures 4-35 and 4-36** for electronic reference frequencies of 69.4 and 7.28 MHz, respectively. It is observed in both cases that the response trails off as the AOTDL input separates further from the electronic reference. This is due to the overlap of the two beams on the photodetector as given in Equation 4-69. This frequency response can be improved by forming better spots on the AOTDL input (thereby increasing the AOSLM image size at the photodetector) and by using a compensating electronic filter after the mixer. The improvement of the optical system design should significantly level off at this frequency response. The phase response for a representative scenario is shown in **Figure 4-37**.

Finally, it was desired to measure the true time-delay properties of the noninterferometric tapped delay line architecture. For this measurement, the output of the system after mixing up to system IF was examined on an oscilloscope. A two-tone waveform with a 4-MHz tone separation on an 80-MHz carrier was used as the test waveform. The test waveform was used as a trigger reference and was input to the

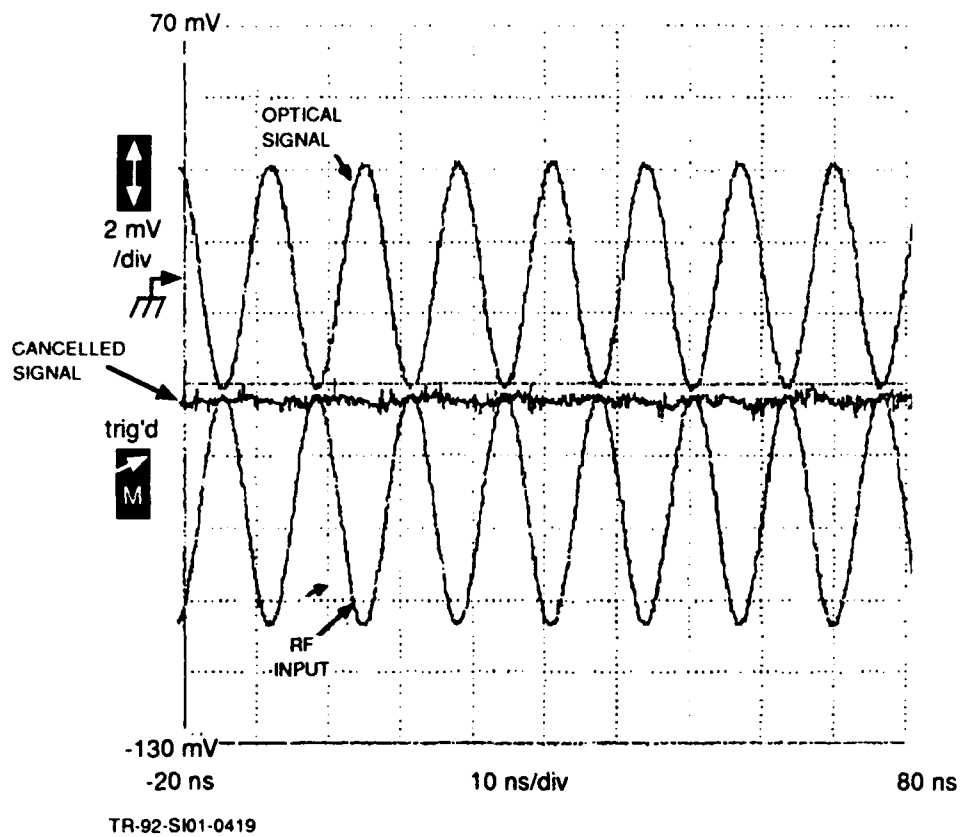


Figure 4-29. Cancellation of a Single Tone

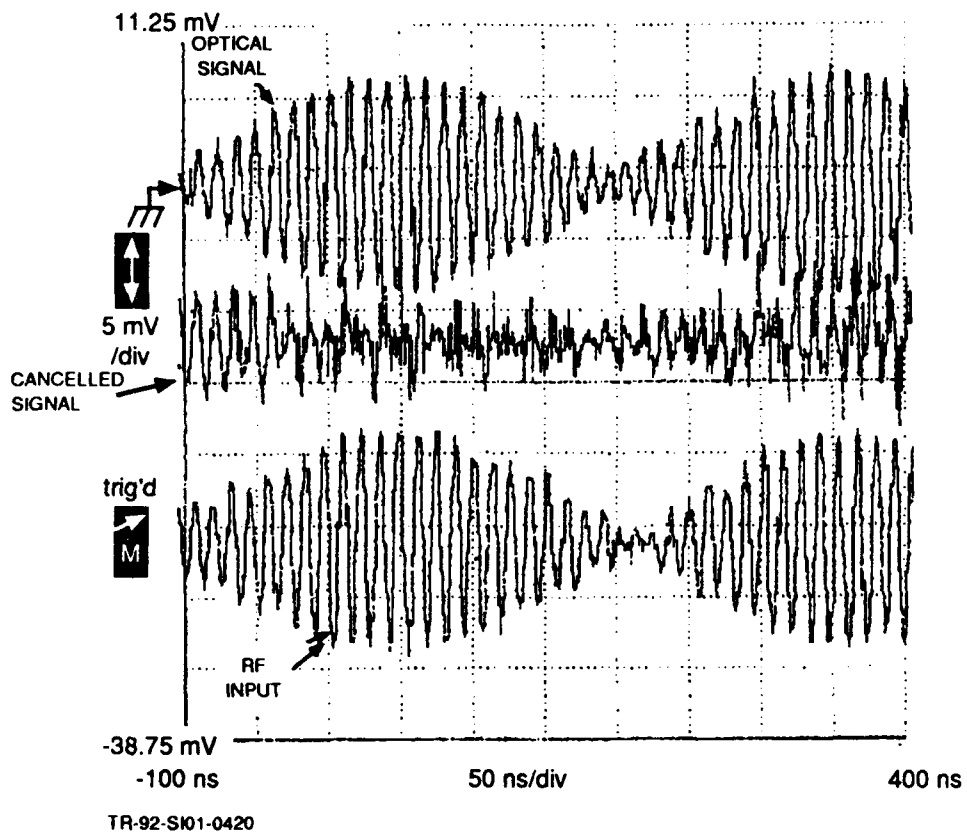


Figure 4-30. Cancellation of a 3.2-MHz Separation, Two-Tone Waveform

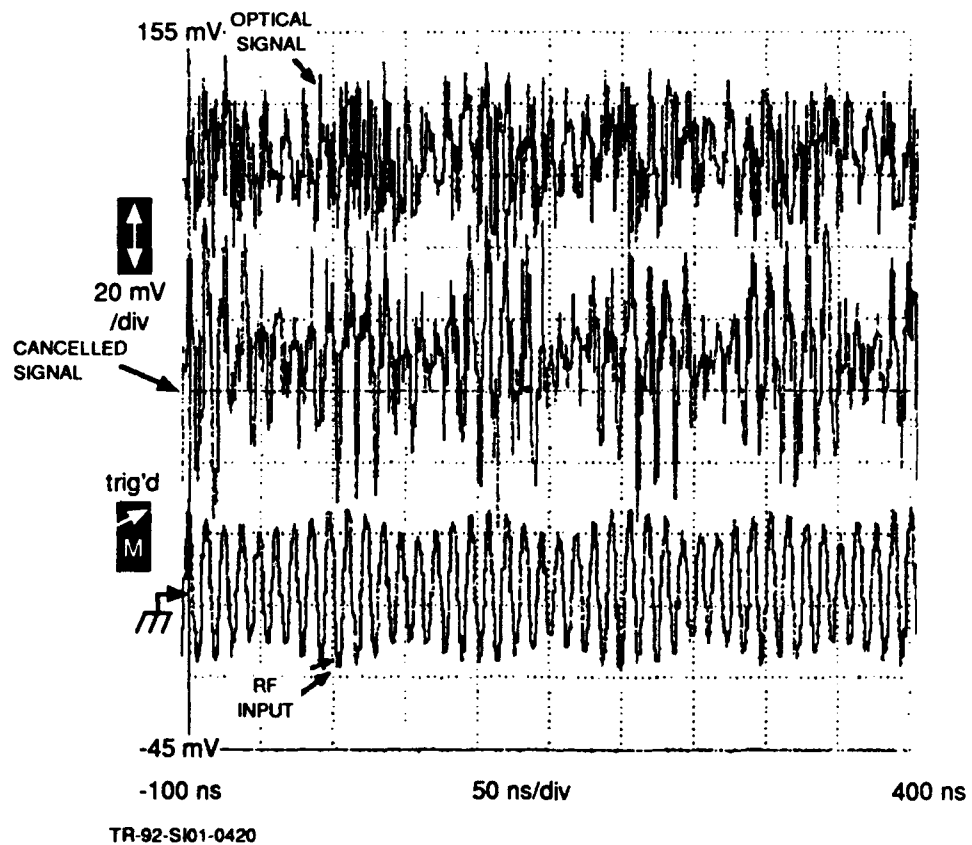
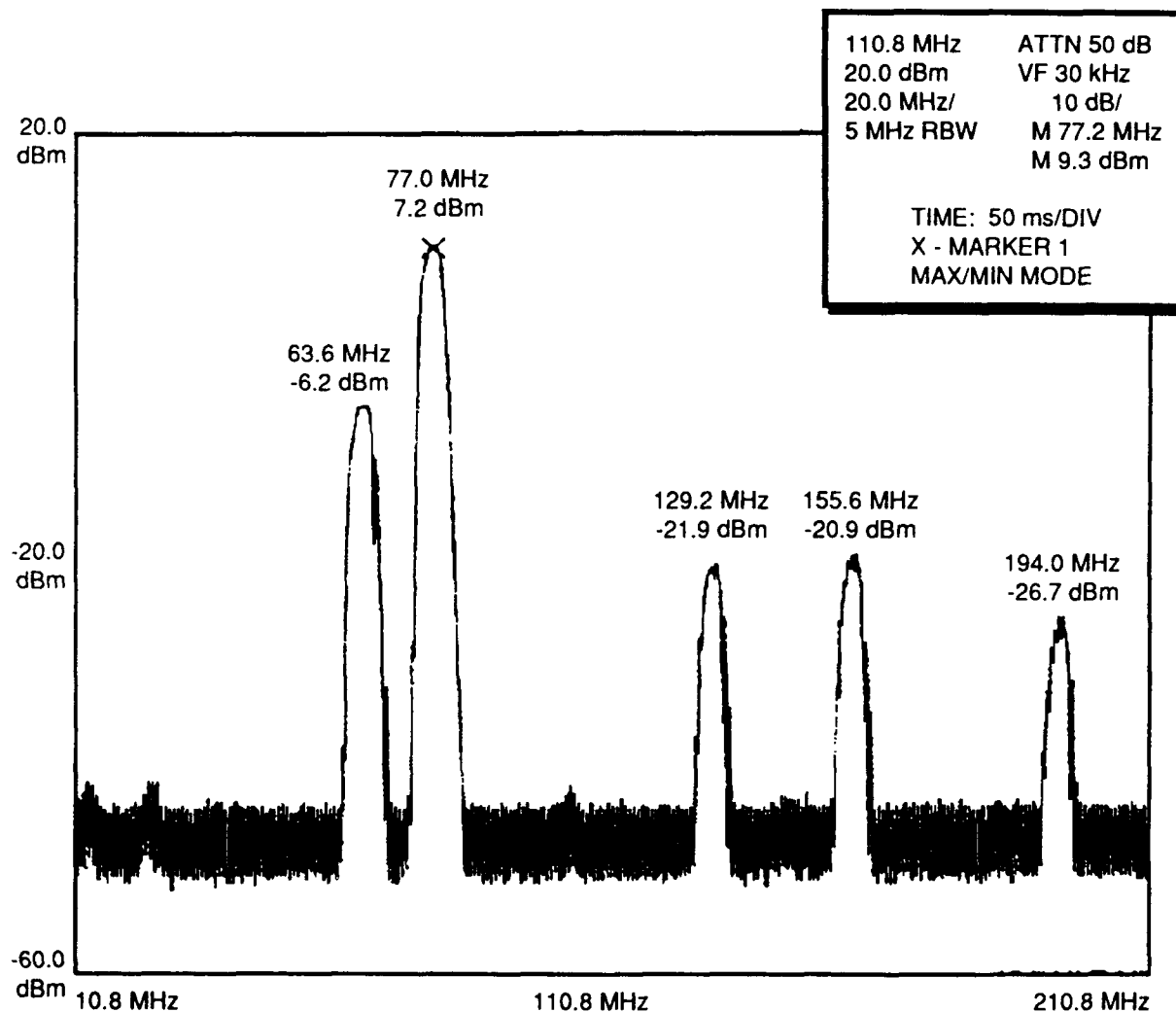


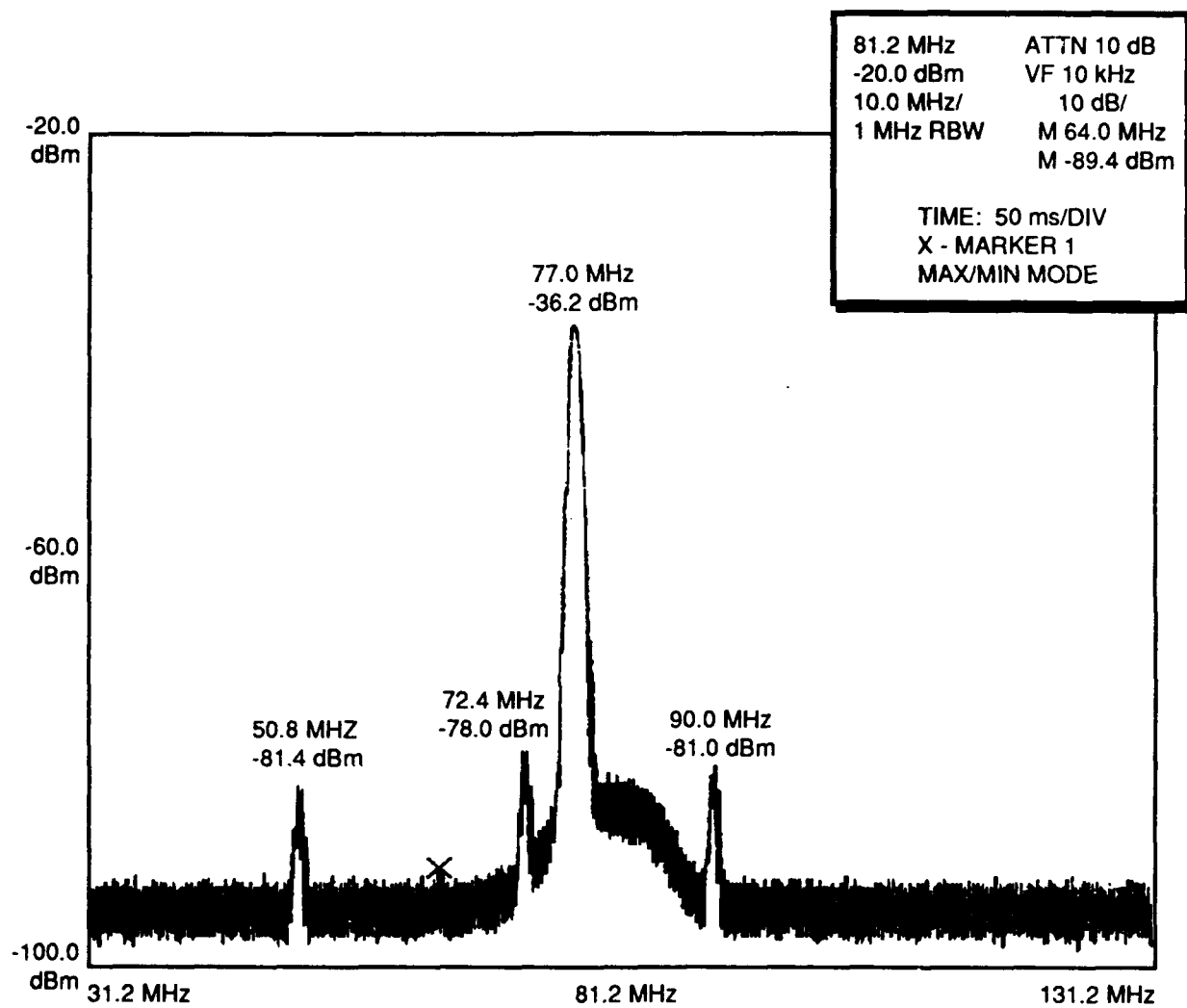
Figure 4-31. Cancellation of a 10-MHz Separation, Two-Tone Waveform



(a) RF Input to AOTDL

TR-92-SI01-0422

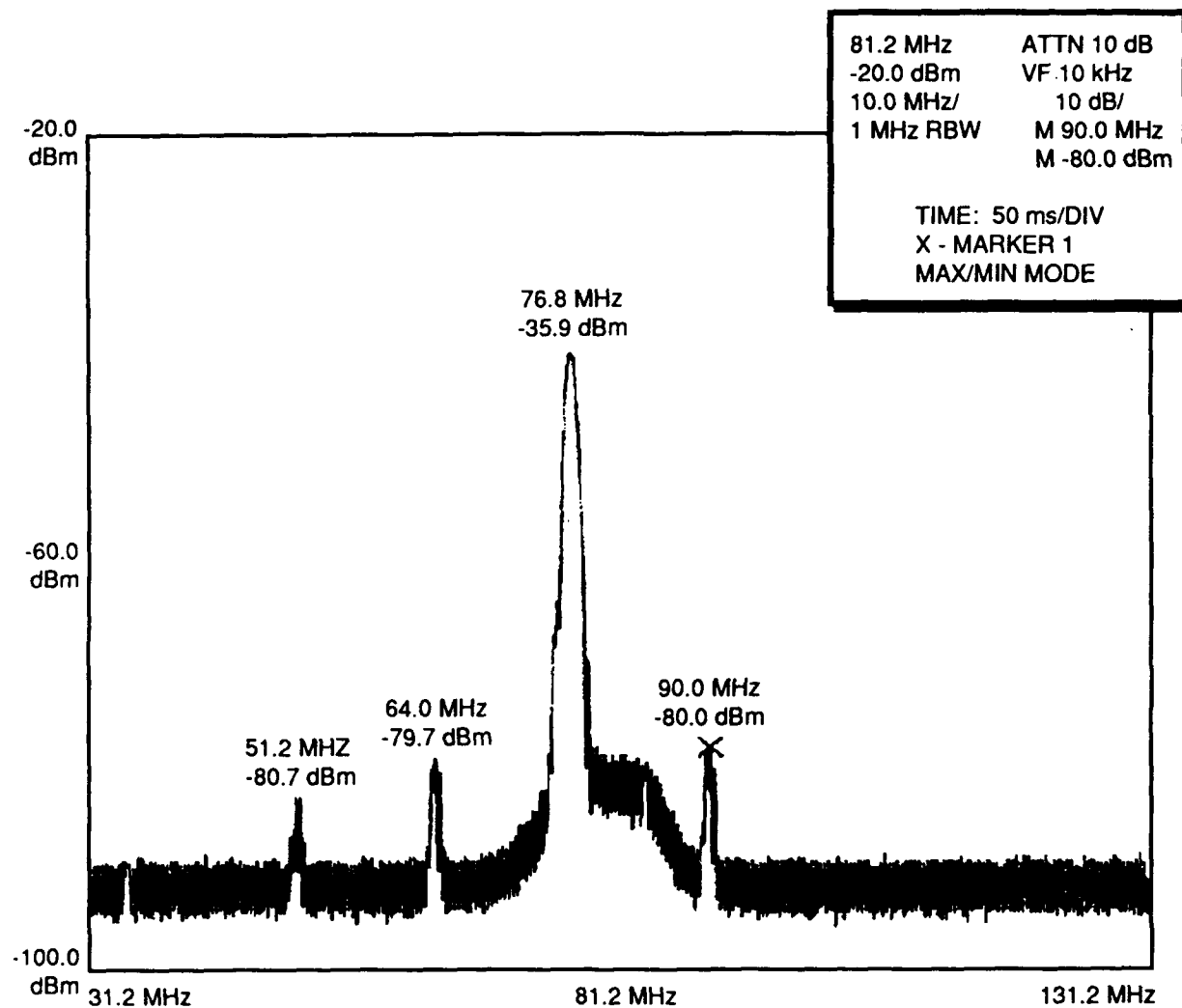
Figure 4-32. AOTDL System Test Measurements (Case 1)



(b) Optical Output for 60-MHz AOSLM Input

TR-92-S101-0423

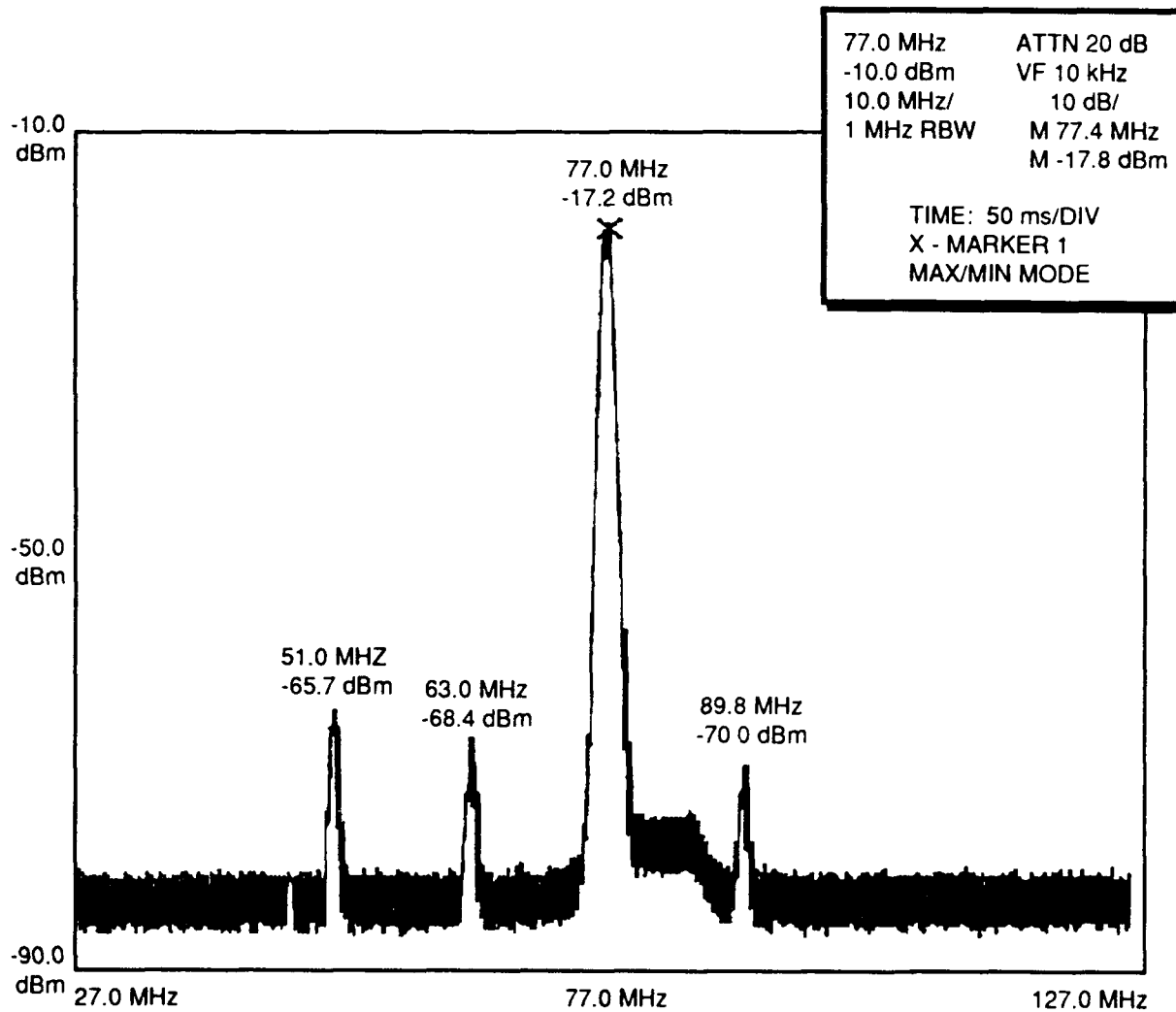
Figure 4-32. AODTL System Test Measurements (Case 1) (Continued)



(c) Optical Output for 70-MHz AOSLM Input

TR-92-S101-0424

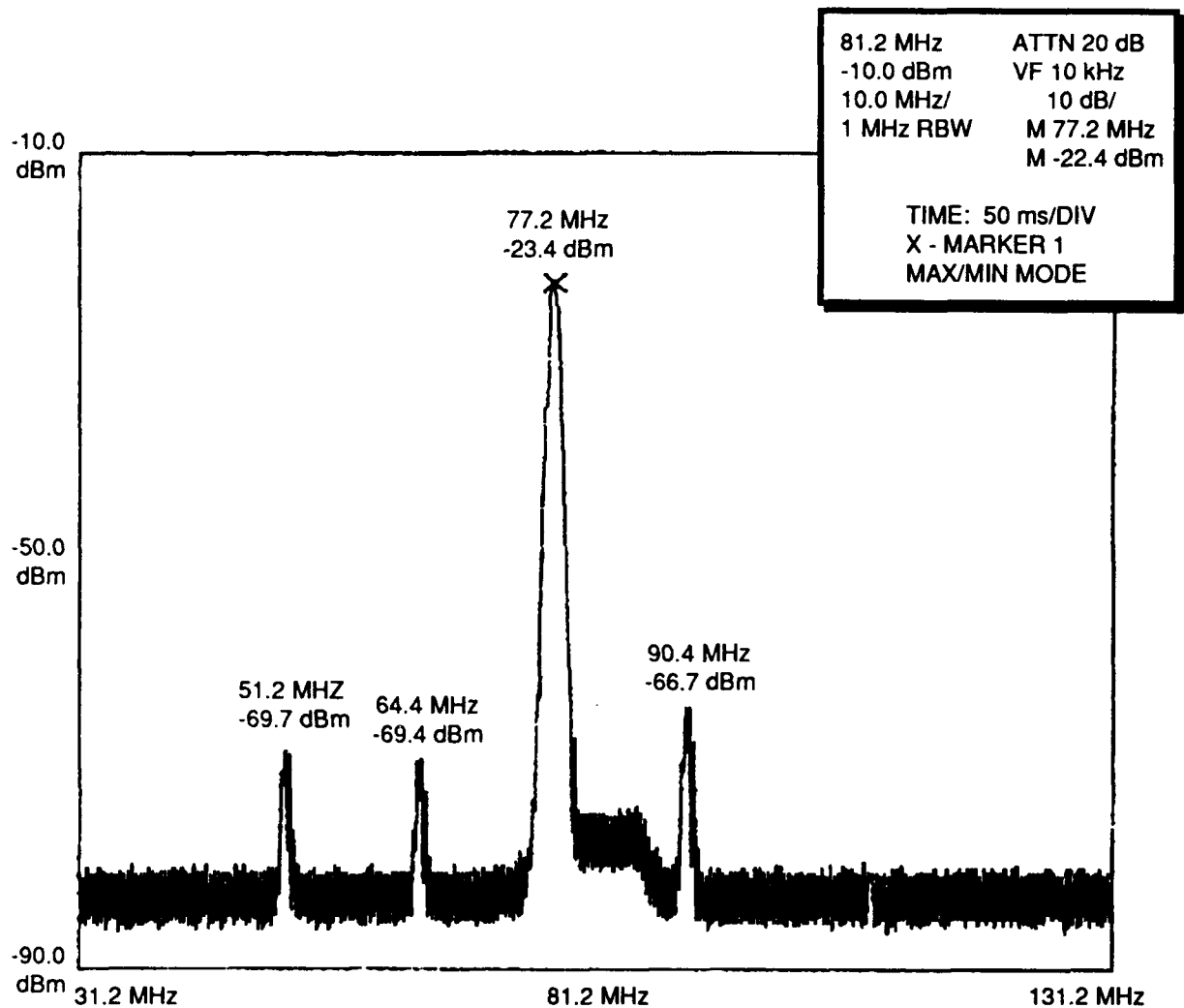
Figure 4-32. AODTL System Test Measurements (Case 1) (Continued)



(d) Optical Output for 79-MHz AOSLM Input

TR-92-S101-0425

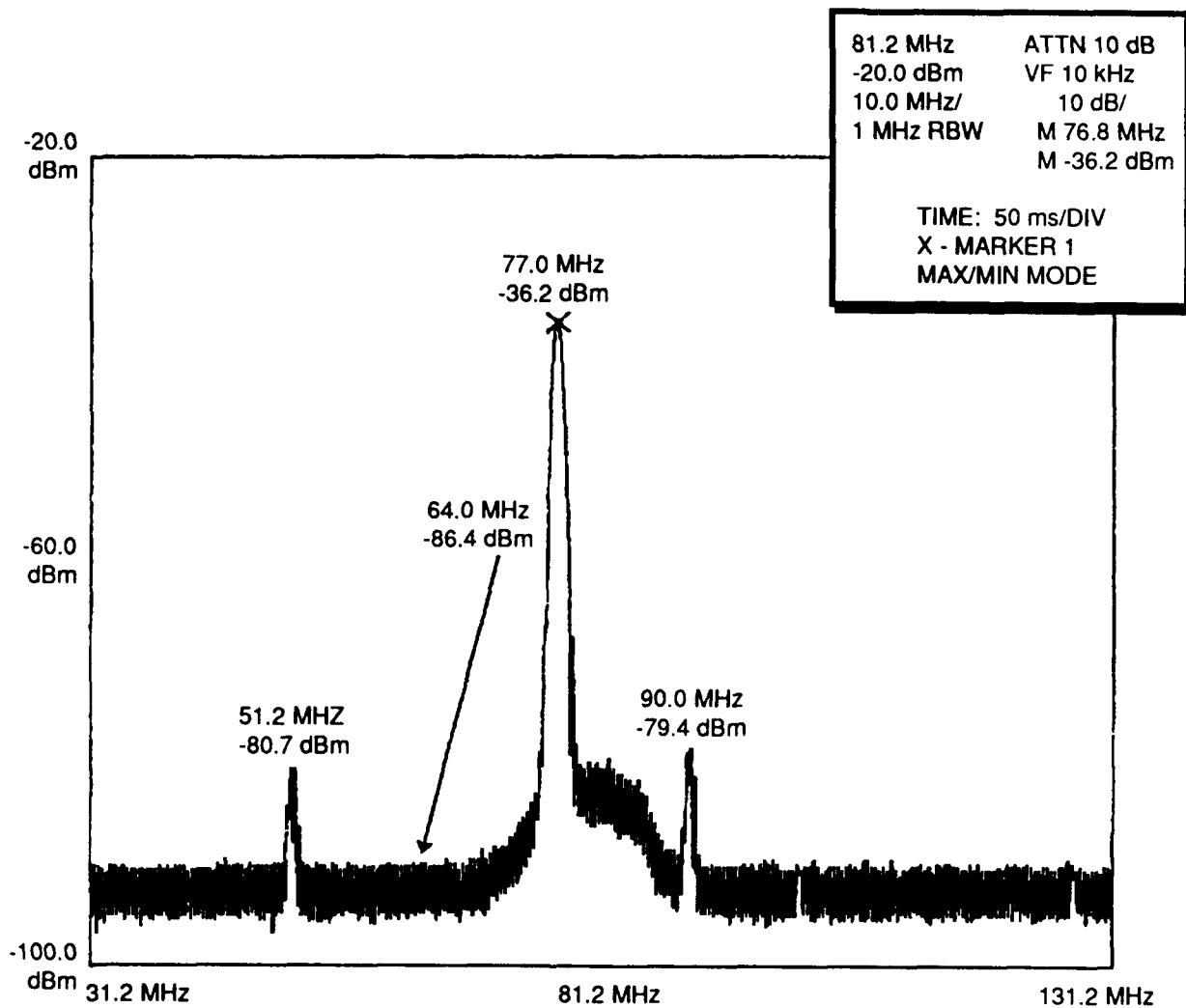
Figure 4-32. AODTL System Test Measurements (Case 1) (Continued)



(e) Optical Output for 90-MHz AOSLM Input

TR-92-SI01-0426

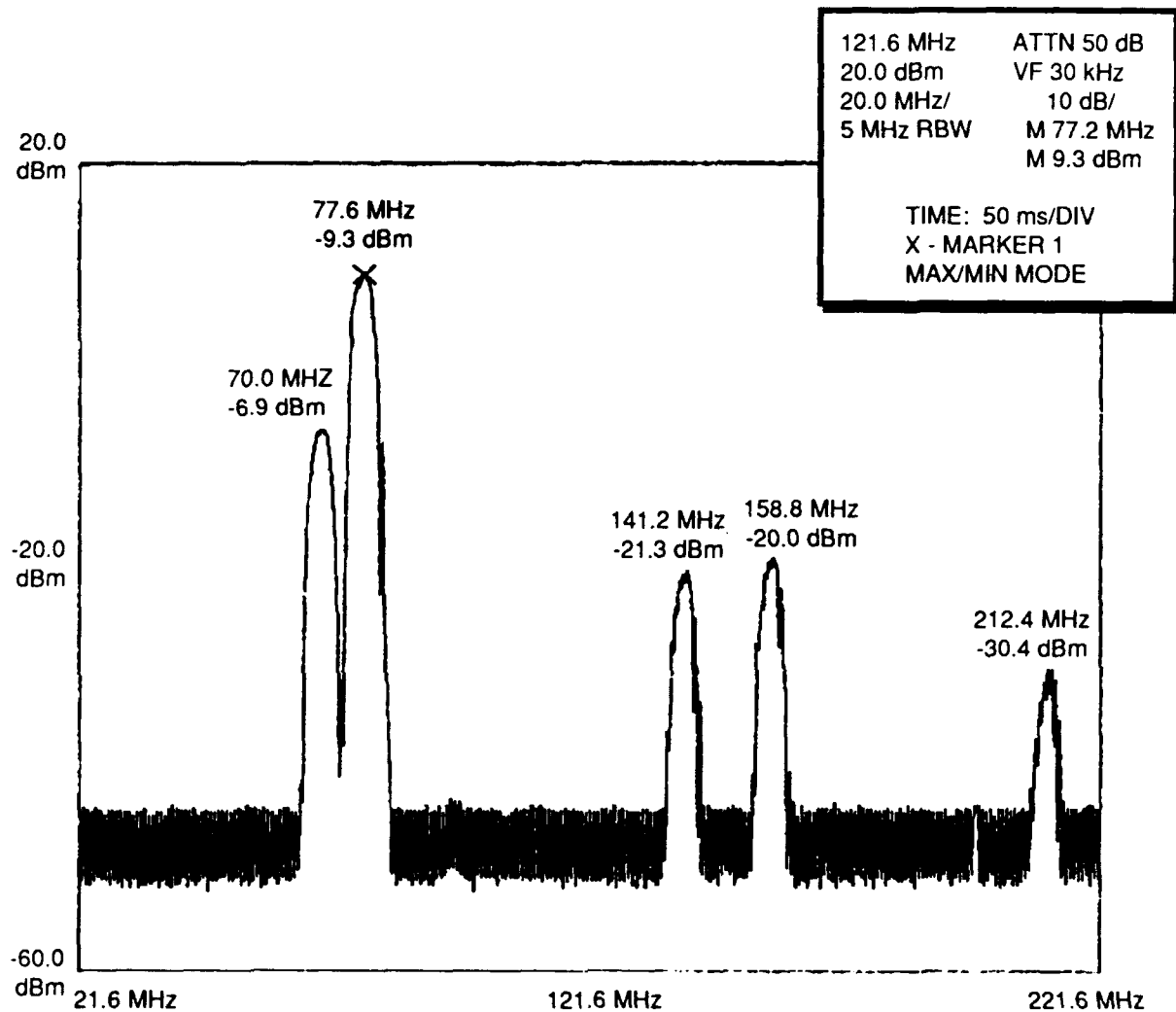
Figure 4-32. AODTL System Test Measurements (Case 1) (Continued)



(f) Optical Output for 100-MHz AOSLM Input

TR-92-S101-0427

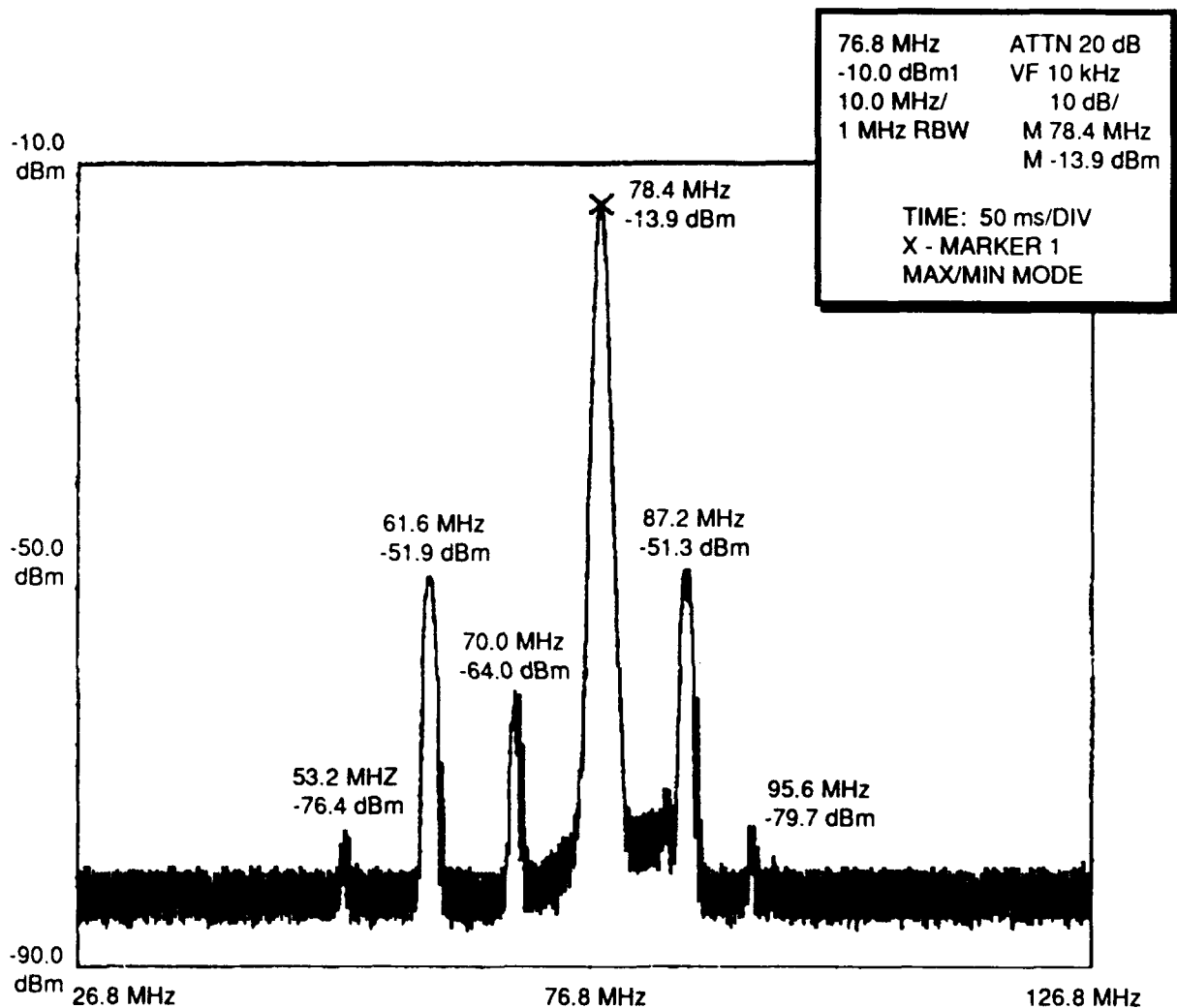
Figure 4-32. AODTL System Test Measurements (Case 1) (Concluded)



(a) RF Input to AODTL

TR-92-SI01-0428

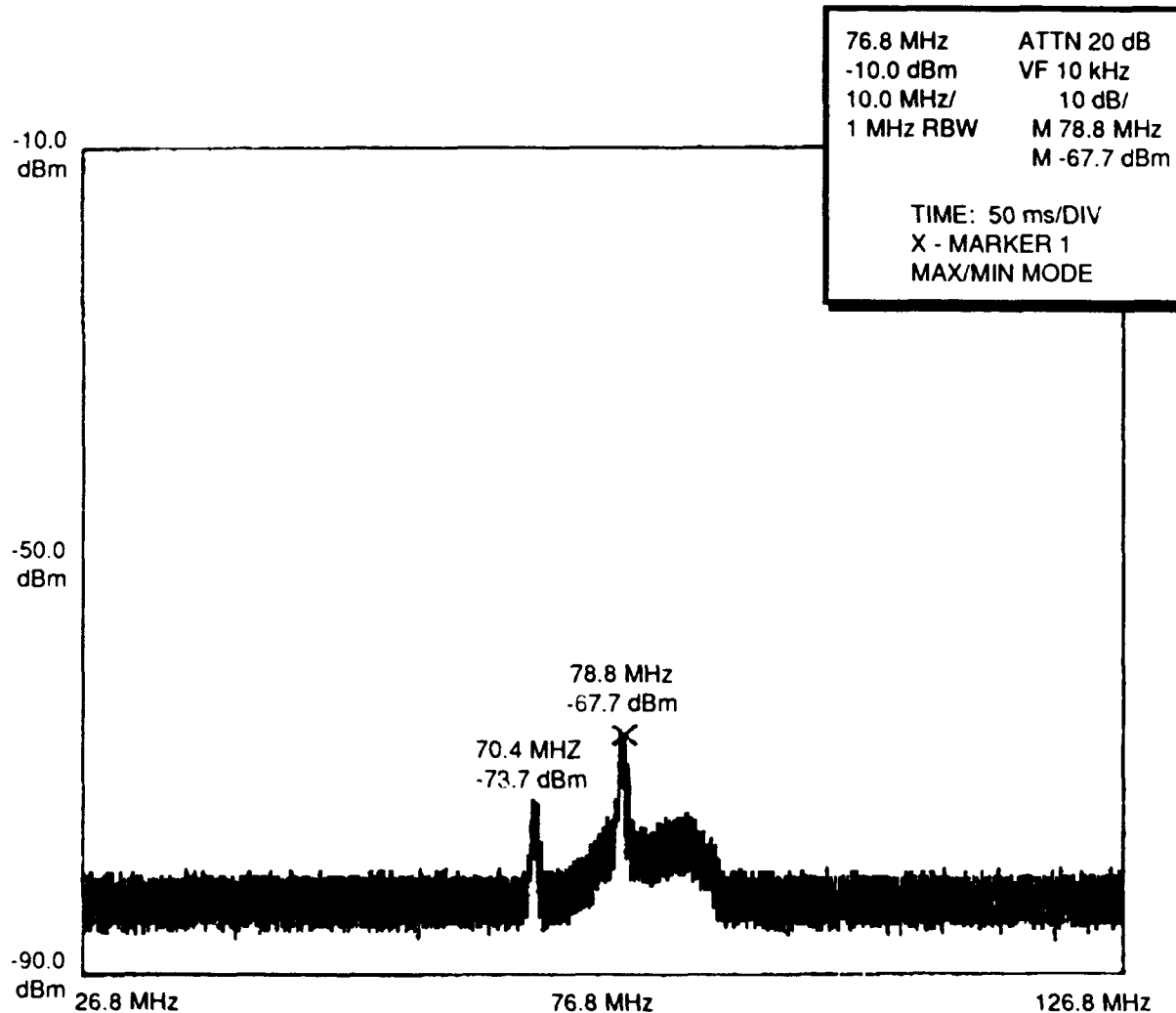
Figure 4-33. AODTL System Test Measurements (Case 2)



(b) Optical Output for 79-MHz AOSLM Input

TR-92-SI01-0429

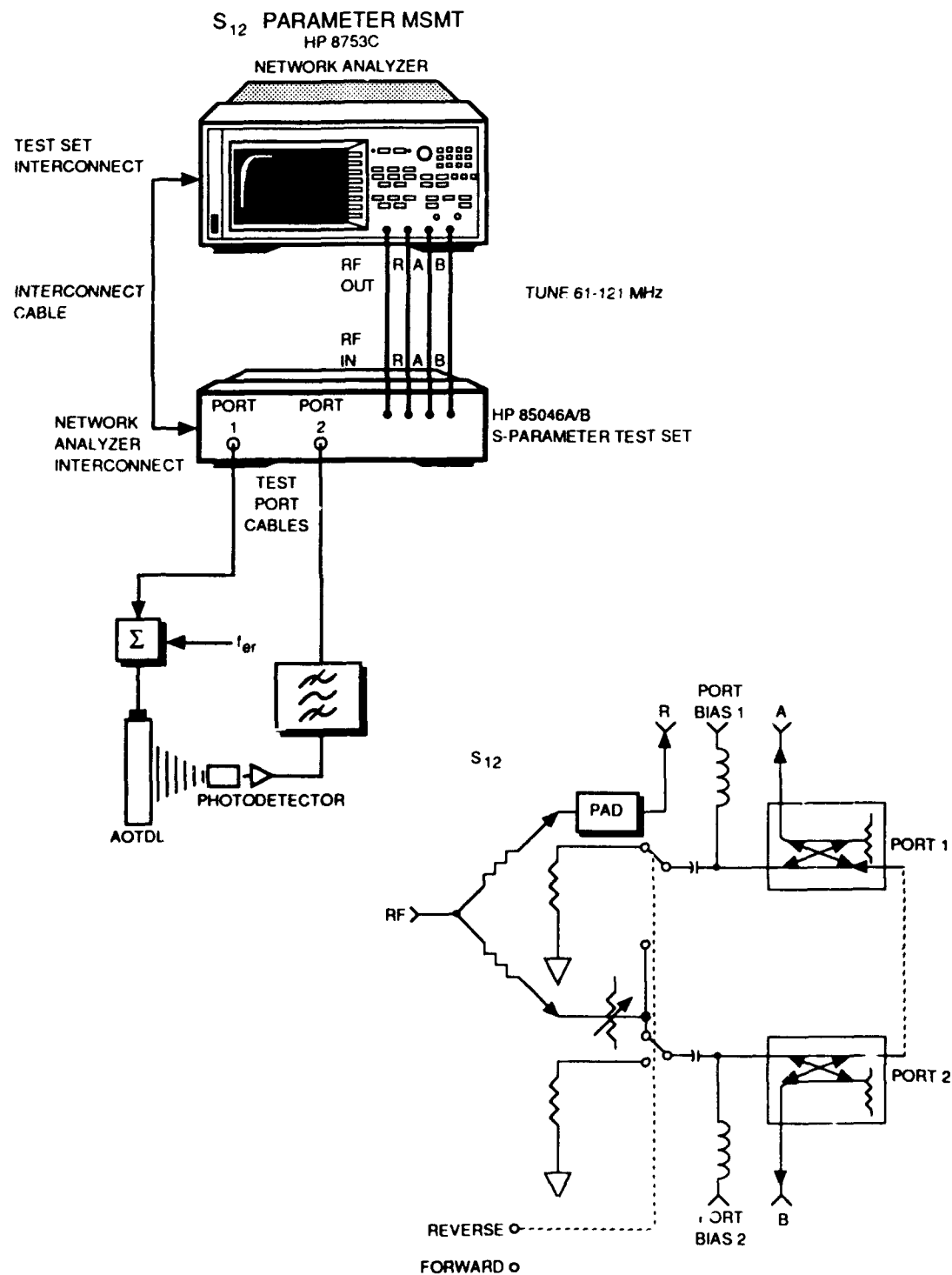
Figure 4-33. AOTDL System Test Measurements (Case 2) (Continued)



(c) RF Interface With No Detector Illumination

TR-92-SI01-0430

Figure 4-33. AOTDL System Test Measurements (Case 2) (Concluded)



TR-92-S101-0023

Figure 4-34. Network Analyzer Measurement Setup

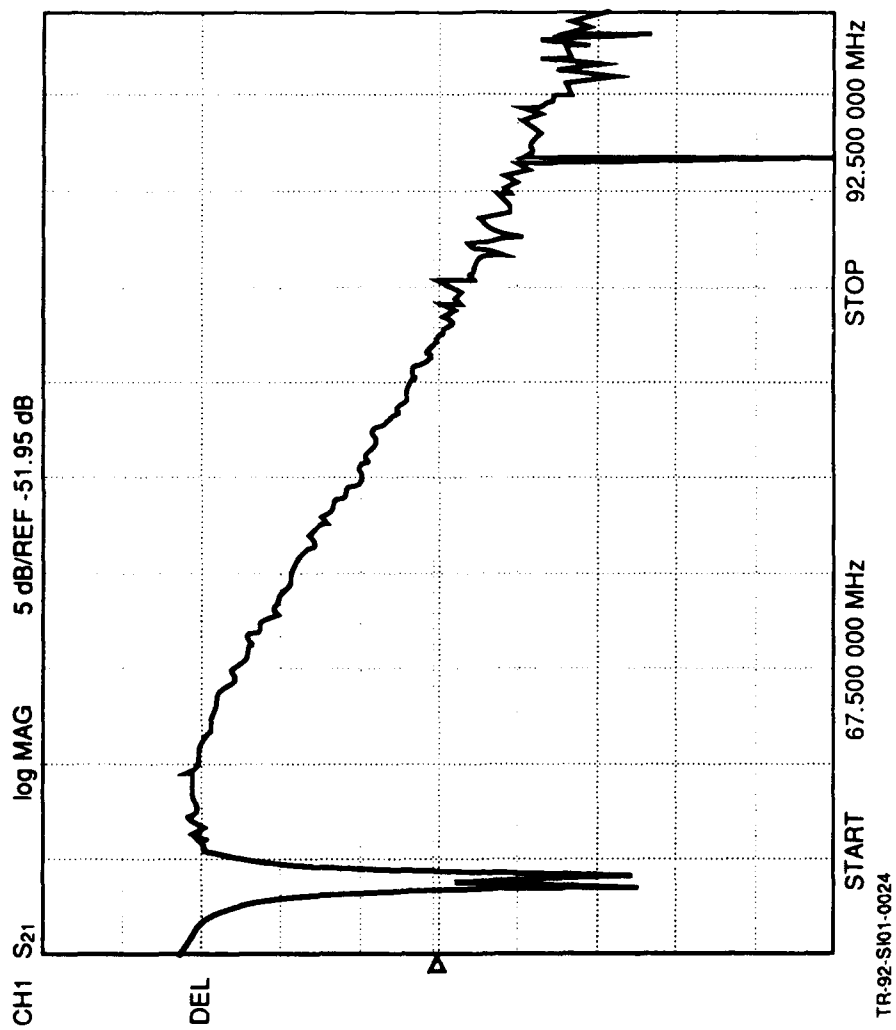


Figure 4-35. Tapped Delay Line Frequency Response for $f_{ER} = 69.4$ MHz

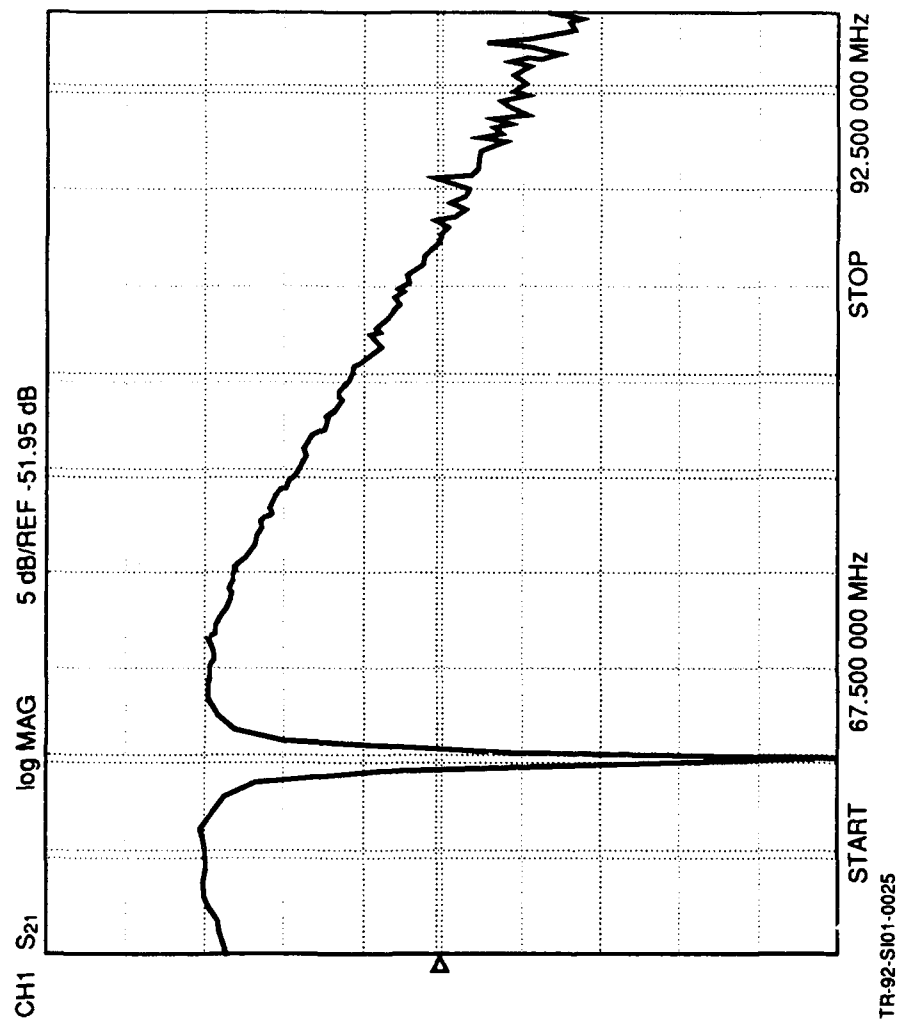


Figure 4-36. Tapped Delay Line Frequency Response for $f_{ER} = 72.8$ MHz

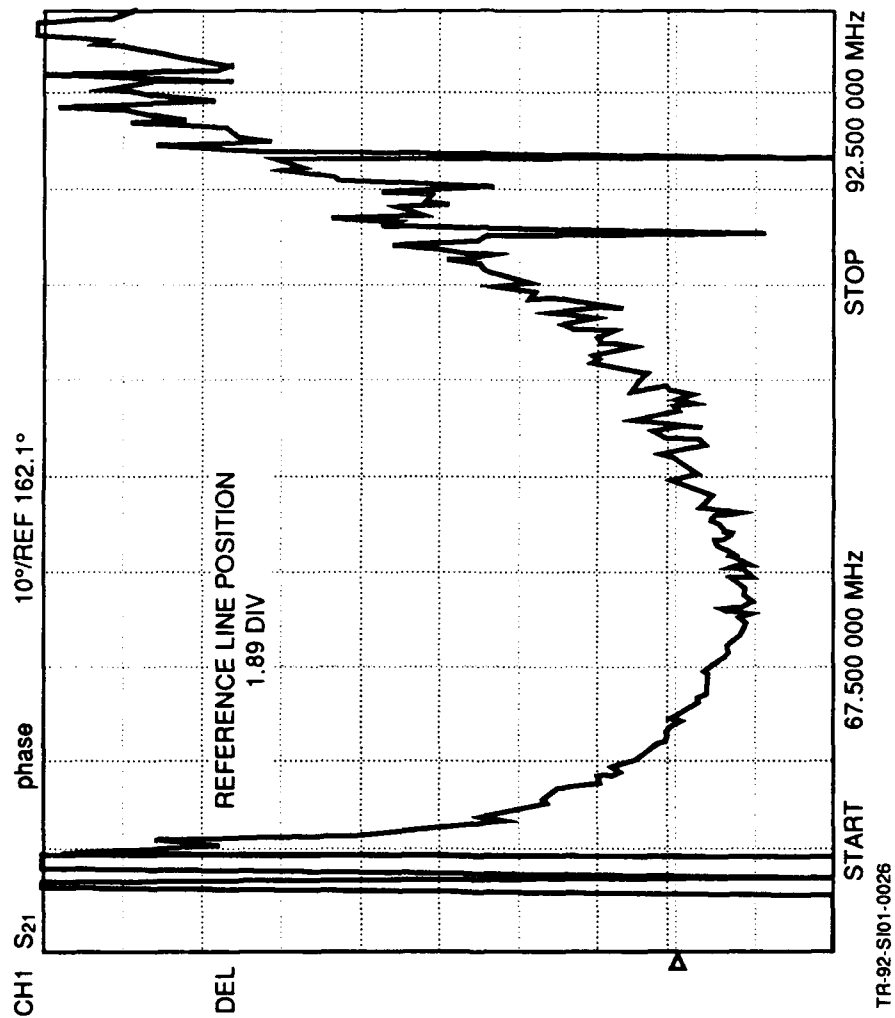


Figure 4-37. Tapped Delay Line Phase Response for $f_{ER} = 69.4$ MHz

oscilloscope's channel A while the system output was displayed on channel B. The AOSLM input was then tuned, thereby tuning the delay, and the output signal was observed to sweep by the trigger reference. For this waveform, 20 cycles of the carrier appear between nulls of the envelope. A delay sweep from null to null was generated and the carrier was seen to go through 20 cycles, thereby verifying the true time-delay behavior of the system. Further examination of Equation 4-69 is required to determine the effect of the term $\Delta\Phi_{ij} - \Delta\Phi_{ier}$, and how true time-delay is achieved. This further analysis should also include the post-detection mixing operation to achieve the output at the system IF.

4.3.3 AOSLM Intermodulation Products

A significant effect in this tapped delay line architecture is the generation of spurious signals from the AOSLM due to diffraction nonlinearities, known as intermodulation products. For two input frequencies, f_1 and f_2 , the diffracted output will correspond to these two frequencies, but two outputs in the pass band of the device at frequencies $2f_1 - f_2$ and $2f_2 - f_1$ are also present. This is shown schematically in **Figure 4-38**. These two spurious two-tone intermodulation products, I_s , are suppressed relative to the intensity of each desired frequency, I_1 and I_2 , by an amount equal to:

$$\frac{I_s}{I_2} = \frac{I_1 I_2}{36} \quad (4-72)$$

For $I_1 = I_2 = I_{\text{desired}}$, then:

$$\frac{I_s}{I_{\text{desired}}} = \frac{I_{\text{desired}}^2}{36} = \frac{\eta_f^2}{36} \quad (4-73)$$

where η_f is the diffraction efficiency of the AOSLM for the given tap frequency power. This ratio is known as the spur-free dynamic range of the system and defines the level of the spurious tones relative to the maximum two-tone input drive powers. This can be thought of as a crosstalk term or as a limitation on contrast ratio when multiple taps are selected. If the taps are normalized so that the sum of all the a_i^2 is equal to one, then this product is included in the equations developed above.

This can be used in the design to set a maximum drive power for adequate suppression of the two-tone intermodulation products. This drive power is such that the diffraction efficiency will be:

$$\eta_f = 6 \left[\frac{I_s}{I_{\text{desired}}} \right]^{1/2} \quad (4-74)$$

For example, if the spurious-free dynamic range of the system is required to be 40 dB, then I_s / I_{desired} must equal 0.0001, which results in a maximum diffraction efficiency of 0.06, or 6% per tap frequency. This

impacts the amplitude of the output signal since a large amount of the light into the system is lost when the undiffracted AOSLM output is filtered. This example is shown on the plot of **Figure 4-39**, which is for longitudinal TeO₂. A 0.06 light output level is squared and divided by 36 to find the two-tone intermodulation product which will be at 6×10^{-6} , as shown in the plot.

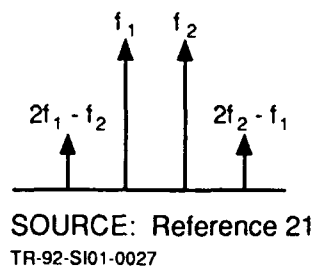
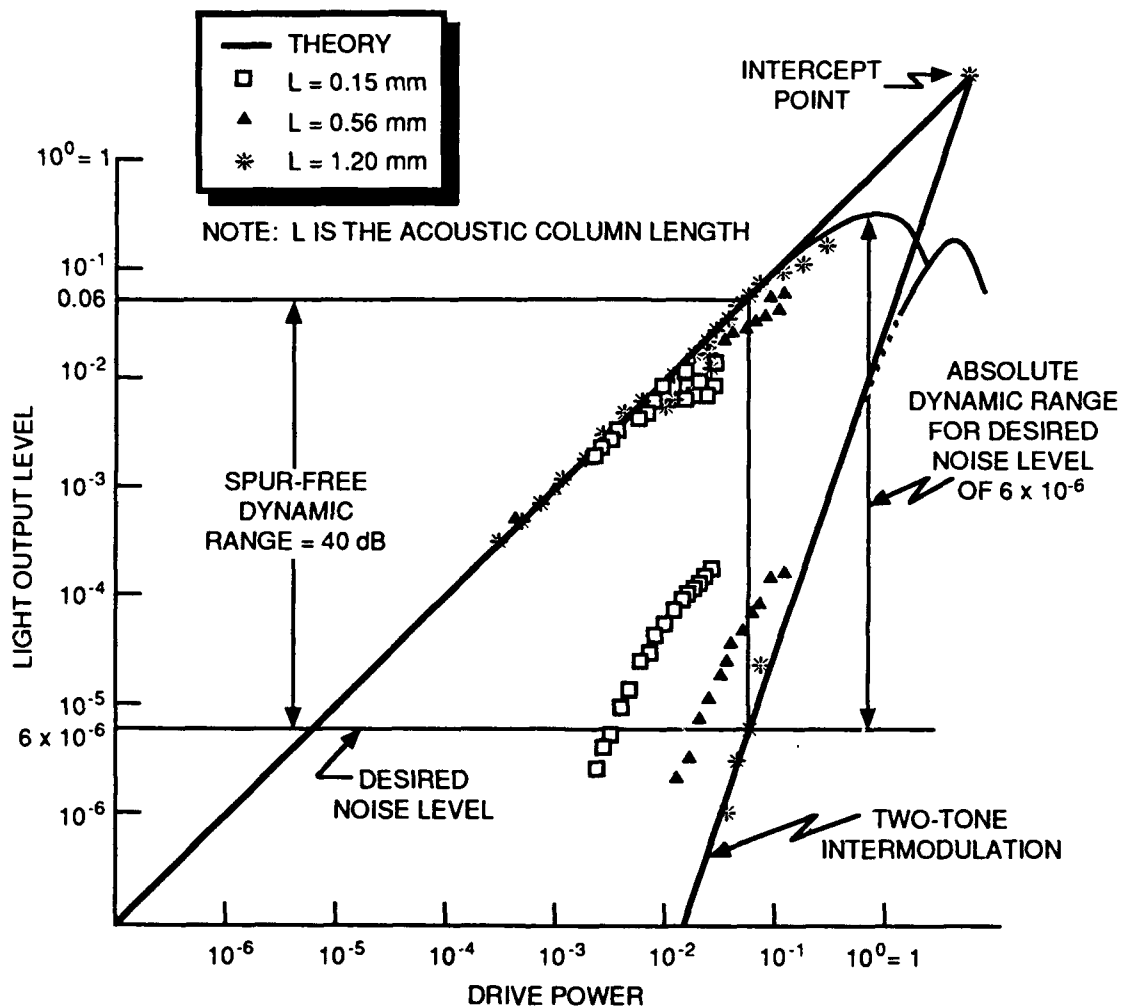


Figure 4-38. Two-Tone Intermodulation Products

A more severe requirement results when considering the three-tone intermodulation products given by $f_1 + f_2 - f_3$ and $f_3 + f_2 - f_1$, as shown in **Figure 4-40**. For this situation, similar analysis as above yields the requirement that for equal intensity input frequencies:

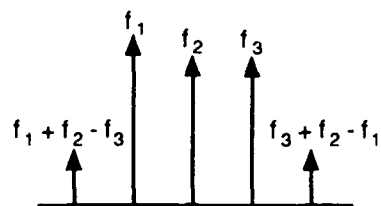
$$\eta_f = 3 \left[\frac{I_s}{I_{\text{desired}}} \right]^{1/2} \quad (4-75)$$

For the example above, this would result in a maximum diffraction efficiency of 3% per tap frequency.



SOURCE: Reference 22
TR-92-S101-0028

Figure 4-39. Two-Tone Intermodulation Dynamic Ranges of Longitudinal TeO_2 Bragg Cells for Several Acoustic Power Densities



SOURCE: Reference 21
TR-92-SIO1-0029

Figure 4-40. Three-Tone Intermodulation Products

5. CONCLUSIONS AND RECOMMENDATIONS

Many issues regarding design, analysis, and fabrication have been presented in this final report. Careful examination of the adaptive system in light of the radar requirements is necessary to develop such issues so they are not surprises in the future. The synergistic combination of processor simulation and hardware development should offer greater insight into the key aspects of the system. For example, the incremental changing of the adaptive weights using "block LMS" techniques must be further examined. There are a number of challenges yet to overcome, but we are confident that the continued development of this system will yield elegant solutions that take full advantage of the best attributes of optics and electronics. It is hoped that this serious consideration of algorithm and hardware analysis and design will direct Dynetics' resources to achieve the best possible product in the long run.

5.1 RADAR INSERTION CONSIDERATIONS

It appears that the MADOP is maturing to a point where it can be tested in a radar test-bed. To this end, there are several issues related to potential performance and system implementation that must be addressed. One of these is a concern for how the MADOP performs relative to a multichannel jamming suppression system that does not contain the delay-line feature. A further concern is whether or not the existing version of the MADOP offers better performance than an interference canceller that does not include the delay-line feature. There is a related issue of whether the nondelay-line version could be easily implemented with optical processing techniques. It is recommended that this area be pursued with analysis and simulation.

The C-band radar operated by OCCR appears to offer the most attractive Rome Laboratory test-bed for the MADOP. All the receiver channels are readily available and provide outputs at the proper IF. They also appear to have bandwidths that are compatible with the capabilities of the MADOP. The radar has a second auxiliary antenna that could be mounted near the existing auxiliary antenna to provide two auxiliary channels. Furthermore, it might be possible to form additional auxiliary channels by accessing individual subarrays of the main array. However, before such an approach is tried, it would be necessary to obtain details on the scanning characteristics of the subarray. If the subarrays are scanned, this could introduce complications into the operation of the MADOP. Other attractive features of the C-band array radar are the two jammers and a boresight tower associated with it. If a corner reflector or some type of signal repeater could be attached to the boresight tower, it could provide a target signal source for some of the testing.

Another area of performance that should be considered is the convergence time of the MADOP. This impacts the implementation, use and performance of the radar when it incorporates the MADOP. It may be that all pulses transmitted during the convergence period will not be available for other signal

processing functions. The net effect of this is a loss in radar resources. If the convergence period is a significant portion of the processing interval, this could seriously impact system performance. Another area related to convergence time is the use of the MADOP in a continuously scanning search radar. If the convergence time is too large, the scan rate of the radar would have to be slowed, which could affect overall performance of the radar. If jamming is severe enough, the resultant performance degradation could be much worse due to very long convergence times. Also related are the effects of MADOP operation on clutter cancellation, pulse distortion, and target parameter measurements.

In the area of system implementation, the problem exists as to just how the jammer suppression system should be implemented in the sum and difference channels of the radar and what effect the jammer suppression system would have on monopulse performance. It should also be noted that for search radars, which typically do not employ monopulse techniques, this may not be a problem; for track radars however, it will definitely be an issue. Furthermore, the impact on performance will depend upon the type of monopulse processing; e.g., two channel, three channel, or four channel. There is also a need to consider the implementation impact on multiple-beam antennas.

In Section 2, we discussed how the MADOP technology could be inserted into fielded systems and/or systems under development. In the future, it will be necessary to determine who, currently within the Air Force, is designing new radars and retrofitting or upgrading older radars. The people identified should be those who are in a position to authorize or recommend inclusion of new subsystems in the radars. A key facet to describing the capabilities is to define the MADOP in terms that are meaningful to a radar person; this includes careful use of terminology. It is recommended that performance results based on waveforms, modes, antenna scan characteristics, etc., that are compatible with the potential customer's radar be provided. Cost and schedule estimates for one of the MADOP systems should also be determined. Finally, if the potential customer shows any interest, he/she should be invited to Rome Laboratory to observe a demonstration of the MADOP in one of the Rome Laboratory radar test-beds when such a demonstration milestone is reached.

5.2 MADOP HARDWARE DEVELOPMENT CONSIDERATIONS

As summarized in this final report, progress on the design and hardware implementation of the two AO subsystems has been significant. Both subsystems are compatible with processing at the radar system IF and allow for coherent (magnitude and phase) processing. Two architectural variants of each AO subsystem were examined in both theory and hardware, and evaluated to assess ultimate system utility. The PC interface between the two AO subsystems remains a key design issue and needs to be further emphasized.

The testing performed on the in-line correlator has given much insight to the architecture setup, operation, capabilities and limitations as described in Subsection 4.2.1. Further analysis/testing should be performed since operation and performance of the new components, such as the multichannel AO cell and CCD array, may differ from that of the current components in the preliminary setup. Due to time and hardware constraints, full characterization of the in-line architecture did not occur. Considering the architectural comparisons presented in Subsection 4.2.3, it was decided that the emphasis for hardware implementation and testing would be the two-path correlator architecture. It is recommended that work on the in-line correlator hardware implementation proceed on an as-needed basis.

The two-path Mach-Zehnder correlator development reported on in Subsection 4.2.2 has offered a *second time-integrating correlator architecture* that is judged to have superior performance over the in-line architecture. Whereas the in-line architecture employs a laser diode and one AO cell, the Mach-Zehnder architecture uses two AO cells. For multichannel operation, either one or two multichannel AO cells can be employed, although current testing has been performed with one multichannel and one single-channel AO cell. It is recommended that two multichannel AO cells be employed in future implementations to reduced the optical system complexity and improve stability. Packaging of this MADOP subsystem on a 2 by 2 ft breadboard, and additional testing should be emphasized. Tests that should be performed include further dynamic range characterization, linearity, delay window uniformity, and the effects of the post-detection processing algorithms on these measurements.

Two AOTDL architectures were also developed to perform the filtering operations required in the MADOP. The Mach-Zehnder interferometric architecture, described in Subsection 4.3.1, was an initial attempt to obtain coherent operation at the system IF. Although heterodyne efficiency was high and output was at the system IF, it was recognized theoretically and observed experimentally that true time-delay was not achievable. In order to remedy this situation, a noninterferometric architecture was designed and implemented.

The noninterferometric AOTDL architecture was designed and implemented as described in Subsection 4.3.2. This AO system employs an electronic reference tone to improve heterodyne efficiency. The detected signal output is at a reduced center frequency and is mixed back up to the system IF after detection. Initial testing of frequency response and cancellation performance were accomplished but further testing must be performed in future efforts. Preliminary measurements made at the Photonics Center showed that true time-delay was achieved with this architecture, although later theoretical development implied that true time-delay should not be observed (see Equation 4-69). If the theory is verified and true time-delay is not achieved, the electronic reference approach should be dropped. A third architecture that mixes the undiffracted and diffracted beams (see Equation 4-64) should then be developed. It is also

recommended that the AOTDL subsystem be reduced to a 2 by 2 ft package to improve phase stability, which is critical to noise cancellation performed at the system IF.

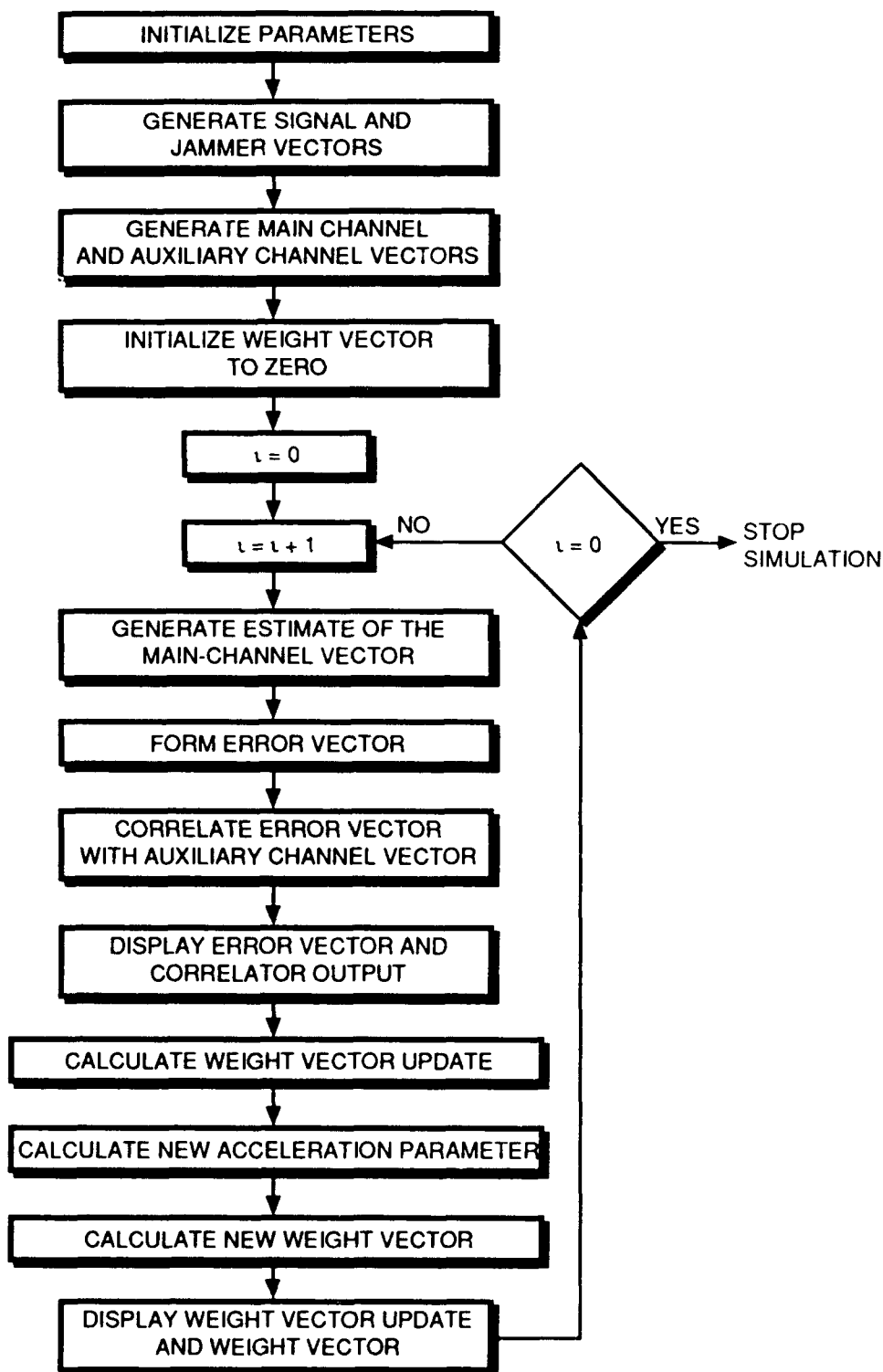
As noted above, a key limitation of the MADOP system is the current PC interface. Consideration of alternative hardware that offers improved interface and processing speed should be undertaken. Also algorithms for determining weight functions need to be further studied and coordinated with simulation activities. Finally, future alternative to the current PC interface being considered is a combined integrating photodiode/laser diode array. The integrating photodiodes would replace the CCD arrays in the time-integrating correlator while the laser diode array would replace the AOSLM to provide input weights to the AOTDL subsystem. Technology for implementing this approach needs to be further evaluated.

APPENDIX A. MATLAB SIMULATION ROUTINES

This appendix contains software listings described in Subsection 3.2 of this report. Parameters employed in these MATLAB routines are summarized in **Table A-1**, and a flowchart for OJC1 is shown in **Figure A-1**.

Table A-1. Parameters Employed in OJC1, OJC2, and OJC3

Parameter	Definition
d	Received main channel desired signal
s	Uncorrupted received signal
basenoise	Random Gaussian noise vector (filtered in OJC3)
nm	Main channel jammer signal
SJ	Signal to Jammer ratio in main channel
na	Auxiliary channel jammer signal
AM	Auxiliary-to-main channel jamming signal voltage ratio
AM1	AM for Jammer 1 in OJC2
AM2	AM for Jammer 2 in OJC2
pwrorig	Initial jammer power in d
pwr	Residual jammer power in e
w	weight vector
delw	Unthresholded weight update vector
delwold	Previous weight vector
absdelw	magnitude of delw normalized between 0 and 1
k	Vector of indices for which absdelw < 0.1
y	Output estimate of d
e	Error signal, $e = d - y$
r	Correlation of e and na used to generate weight update
a	Acceleration parameter [$\alpha(t)$ in Equation 3-2]
aold	previous acceleration parameter
[b1, a1]	Poles and zeros of Butterworth filter in OJC3
[rmax, indx]	Maximum value of r and its index



TR-92-SI01-0252

Figure A-1. Flowchart for OJC1

```

% Optical Jamming Canceller #1
% "white" noise case
% Iterative but reuses same signal and noise - not real world
% Uses Welstead's adaptive method for computing a in  $w=w+a*r$ 
% Only one jammer and one multipath
% Uses thresholded weight update
a=.3;
delwold=zeros(1,100);
%
% Spacing between time samples is 0.05  $\mu$ s (20 Mhz sample rate)
% Signal, s(:) is a 2  $\mu$ s pulse starting at 1  $\mu$ s
% Total duration of data is 10  $\mu$ s
s=zeros(1,400);
s(121:160)=ones(1,40);
% Generate jammer
% For now jammer is noise with a BW of  $1/(0.05 \mu\text{s}) = 20 \text{ MHz}$ 
% It is also Gaussian
rand('seed',0)
rand('normal')
basenoise=rand(1,500);
% basenoise is the basic jammer source - from which all others are
% derived. It represents the actual jammer output (sort of)
% Generate main channel jamming signal - delay basenoise by 2  $\mu$ s
nm=basenoise(21:420);
% Generate main channel signal plus jamming, d(t)
% SJ is the signal-to-jam ratio (volt/volt)
SJ=sqrt(0.1); % -10 dB
% Compute jammer power
pwrorig=10*log10((nm(101:300)*nm(101:300)')/200/SJ/SJ);
d= s + nm/SJ;
% Generate aux channel jamming signal - delay basenoise by 1  $\mu$ s
% AM is the aux-to-main ratio (volt/volt)
AM=sqrt(0.5); % (-3 dB)
AM=1;
na=basenoise(41:440)*AM;
% Define initial weights as all zeros
w=zeros(1,100);
%%%%%%%%%%%%%%%%%%%%%%%%%%%%%%%%%%%%%%%%%%%%%%%%%%%%%%%%%%%%%%%%%%%%%%%%
% Start loop
%%%%%%%%%%%%%%%%%%%%%%%%%%%%%%%%%%%%%%%%%%%%%%%%%%%%%%%%%%%%%%%%%%%%%%%%
for iter = 1:100
% form  $y=\sum w*na$  - the weighted aux channel signal
y=filter(w,1,na);
% form error signal,  $e=d-y$ 
e=d-y;
% Compute output power after cancellation
res=e(101:300)-s(101:300);
pwr=10*log10((res*res')/200);
% Correlate e and na call the result r
r=xcorr(e,na,'biased');
% plot interim results - error and correlation
clf
subplot(221),plot(e(101:300));title('error')
subplot(222),plot(r(351:550));title('correlator output')
% update weight vector

```



```

% use residues above threshold
delw=r(400:499);
absdelw=abs(delw)/max(abs(delw));
k=find(absdelw<0.1);
delw(k)=zeros(k);
numer=delwold * delwold';
denom=delwold * (delwold-delw)';
if (numer*denom) == 0
    a=0.5;
else
    a=aold*numer/denom;
end
aold=a;
delwold=delw;
w=w+a*delw;

```

Threshold Weight Vector Update

```

% pick peak weight only
%[rmax,indx]=max(r(400:499));
%delw=zeros(1,100);
%delw(indx)=rmax;
%numer=delwold * delwold';
%denom=delwold * (delwold-delw)';
%if (numer*denom) == 0
%    a=0.5;
%else
%    a=aold*numer/denom;
%end
%aold=a;
%delwold=delw;
%w=w+a*delw;

```

Peak Weight Update Only

```

% use all residues
%delw=r(400:499);
%numer=delwold * delwold';
%denom=delwold * (delwold-delw)';
%if (numer*denom) == 0
%    a=0.5;
%else
%    a=aold*numer/denom;
%end
%aold=a;
%delwold=delw;
%w=w+a*delw;

```

Full Weight Vector Update

```

subplot(223),plot(delw);title('thresholded weight increments')
subplot(224),plot(w);title('weight')
label= sprintf('Iteration = %3.0f, a= %6.3f',iter,a);
labell= sprintf('inp jmr pwr = %5.1f, out jmr pwr= %5.1f (in
                dB) ',pwrorig,pwr);
text(0.1,0.5,label,'c')
text(0.5,0.5,labell,'sc')

end

```

```

% Optical Jamming Canceller #2
% "white" noise case
% Iterative but reuses same signal and noise - not real world
% Uses Welstead's adaptive method for computing a in  $w=w+a*r$ 
% Only one jammer and but two multipaths in each antenna
% Uses thresholded weight update
a=.3;
delwold=zeros(1,100);
%
%Spacing between time samples is 0.05  $\mu$ s (20 Mhz sample rate)
%Signal, s(t) is a 2  $\mu$ s pulse starting at 1  $\mu$ s
%Total duration of data is 10  $\mu$ s
s=zeros(1,400);
s(121:160)=ones(1,40);
% Generate jammer
% For now jammer is noise with a BW of  $1/(0.05 \mu\text{s}) = 20 \text{ MHz}$ 
% It is also Gaussian
rand('seed',0)
rand('normal')
basenoise=rand(1,500);
% basenoise is the basic jammer source - from which all others are
% derived. It represents the actual jammer output (sort of)
%Generate main channel jamming signal - delay basenoise by 2  $\mu$ s
nm=basenoise(21:420) + 0.5*basenoise(31:430);
% Generate main channel signal plus jamming, d(t)
% SJ is the signal-to-jam ratio (volt/volt)
SJ=sqrt(0.1); % -10 dB
d= s + nm/SJ;
% Generate aux channel jamming signal - delay basenoise by 1  $\mu$ s
% AM is the aux-to-main ratio (volt/volt)
AM1=sqrt(0.5); % (-3 dB)
AM2=1; % (0dB)
na=basenoise(41:440)*AM1 + basenoise(66:465)*AM2;
% Define initial weights as all zeros
w=zeros(1,100);
%%%%%%%%%%%%%%%%%%%%%%%%%%%%%%%%%%%%%%%%%%%%%%%%%%%%%%%%%%%%%%%%%%%%%%%%
% Start loop
%%%%%%%%%%%%%%%%%%%%%%%%%%%%%%%%%%%%%%%%%%%%%%%%%%%%%%%%%%%%%%%%%%%%%%%%
for iter = 1:100
% form  $y=\sum w*na$  - the weighted aux channel signal
y=filter(w,1,na);
%form error signal,  $e=d-y$ 
e=d-y;
% Correlate e and na call the result r
r=xcorr(e,na,'biased');
%plot interim results - error and correlation
clf
subplot(221),plot(e(101:300));title('error')
subplot(222),plot(r(351:550));title('correlator output')
%update weight vector
delw=r(400:499);
absdelw=abs(delw)/max(abs(delw));
k=find(absdelw<0.1);
delw(k)=zeros(k);
numer=delwold * delwold';

```

```

denom=delwold*(delwold-delw)';
if (numer*denom) == 0
    a=0.5;
else
    a=aold*numer/denom;
end
aold=a;
delwold=delw;
w=w+a*delw;
subplot(223),plot(delw);title('thresholded weight increments')
subplot(224),plot(w);title('weight')
label= sprintf('Iteration = %3.0f, a= %6.3f',iter,a);
text(0.45,0.5,label,'sc')

end

```

```

% Optical Jamming Canceller #3
% bandlimited noise case - noise filtered by 2 Mhz, 5 pole Butterworth
% filter. Iterative but reuses same signal and noise - not real world
% Uses Welstead's adaptive method for computing a in  $w = w + a * r$ 
% Only one jammer and one multipath
% Uses thresholded weight update
a=.3;
delwold=zeros(1,100);
%Spacing between time samples is 0.05  $\mu$ s (20 Mhz sample rate)
%Signal, s(t) is a 2  $\mu$ s pulse starting at 1  $\mu$ s
%Total duration of data is 10  $\mu$ s
s=zeros(1,400);
s(121:160)=ones(1,40);
% Generate jammer
% For now jammer is noise with a BW of  $1/(0.05 \mu\text{s}) = 20 \text{ MHz}$ 
% It is also Gaussian
rand('seed',0)
rand('normal')
basenoise=rand(1,500);
[b1,a1]=butter(5,2/10);
basenoise=filtfilt(b1,a1,basenoise);
% basenoise is the basic jammer source - from which all others are
% derived. It represents the actual jammer output (sort of)
%Generate main channel jamming signal - delay basenoise by 2  $\mu$ s
rm=basenoise(21:420);
% Generate main channel signal plus jamming, d(t)
% SJ is the signal-to-jam ratio (volt/volt)
SJ=sqrt(0.1); % -10 dB
% Compute jammer power
pwrorig=10*log10((rm(101:300)*rm(101:300)')/200/SJ/SJ);
d= s + rm/SJ;
% Generate aux channel jamming signal - delay basenoise by 1  $\mu$ s
% AM is the aux-to-main ratio (volt/volt)
AM=sqrt(0.5); % (-3 dB)
AM=1;
na=basenoise(41:440)*AM;
% Define initial weights as all zeros
w=zeros(1,100);
#####
% Start loop
#####
for iter = 1:100
% form  $y = \sum w * na$  - the weighted aux channel signal
y=filter(w,1,na);
%form error signal,  $e = d - y$ 
e=d-y;
% Compute output power after cancellation
res=e(101:300)-s(101:300);
pwr=10*log10((res*res')/200);
% Correlate e and na call the result r
r=xcorr(e,na,'biased');
%plot interim results - error and correlation
clf
subplot(221),plot(e(101:300));title('error')
subplot(222),plot(r(351:550));title('correlator output')

```

```

%update weight vector
%use residues above threshold
%delw=r(400:499);
%absdelw=abs(delw)/max(abs(delw));
%k=find(absdelw<0.1);
%delw(k)=zeros(k);
%numer=delwold * delwold';
%denom=delwold * (delwold-delw)';
%if (numer*denom) == 0
% a=0.5;
%else
% a=aold*numer/denom;
%end
%aold=a;
%delwold=delw;
%w=w+a*delw;

% pick peak weight only
%[rmax,indx]=max(r(400:499));
%delw=zeros(1,100);
%delw(indx)=rmax;
%numer=delwold * delwold';
%denom=delwold * (delwold-delw)';
%if (numer*denom) == 0
% a=0.5;
%else
% a=aold*numer/denom;
%end
%aold=a;
%delwold=delw;
%w=w+a*delw;

% use all residues
delw=r(400:499);
numer=delwold * delwold';
denom=delwold * (delwold-delw)';
if (numer*denom) == 0
    a=0.5;
else
    a=aold*numer/denom;
end
aold=a;
delwold=delw;
w=w+a*delw;

% use
subplot(223),plot(delw);title('thresholded weight increments')
subplot(224),plot(w);title('weight')
label= sprintf('Iteration = %3.0f, a = %6.3f',iter,a);
labell= sprintf('inp jmr pwr = %5.1f, out jmr pwr= %5.1f (in
                dB)',pwrorig,pwr);
text(0.1,0.5,label,'sc')
text(0.5,0.5,labell,'sc')

end

```

REFERENCES

1. Ward, M. J., C. W. Keefer, and S. T. Welstead, Adaptive Optical Processor, In-House Report, RL-TR-91-270, August 1991.
2. Welstead, S. T., and M. J. Ward, Hybrid Electro-Optic Processor, Final Technical Report, RL-TR-91-164, July 1991.
3. Welstead, S. T., Optical Processor Evaluation, Final Technical Report, RL-TR-91-34, March 1991.
4. Ward, M. J., C. W. Keefer, D. J. Grucza, and S. T. Welstead, "Comparison of Spatial Light Modulators for Multipath Delay Estimation", OSA Technical Digest, Vol 14, p. 149, 1990.
5. Haykin, S., Adaptive Filter Theory, Prentice-Hall, Englewood Cliffs, NJ, 1986.
6. Widrow, B., and S. D. Stearns, Adaptive Signal Processing, Prentice-Hall, Englewood Cliffs, NJ, 1985.
7. Widrow, B., et al, "Adaptive Noise Cancelling: Principles and Applications", Proceedings of IEEE, Vol. 63, p 1692, 1975.
8. Rhodes, J. F., "Adaptive Filter with a Time-Domain Implementation using Correlation Cancellation Loops", Applied Optics, Vol. 22, p. 282, 1983.
9. Psaltis, D., and J. Hong, "Adaptive Acoustooptic Filter", Applied Optics, Vol. 23, p. 3475, 1984.
10. Penn, W. A., Acousto-Optic Adaptive Processor (AOAP)- Phase II, General Electric Co., RADC-TR-86-188, November 1986.
11. Montgomery, R. M., and M. R. Lange, "Photorefractive Adaptive Filter Structure with 40 dB Interference Rejection", Applied Optics, Vol. 30, p. 2844, 1991.
12. Berinato, R. J. and M. A. G. Abushagur, "Acousto-Optic Signal Processor for Adaptive Filtering", SPIE Vol. 1296, Adv. in Opt. Info Proc IV., p.232, 1990.
13. VanderLugt, A., "Adaptive Optical Processor", Applied Optics, Vol. 21, p. 4005, 1982.
14. Cohen, J. D., "Optical Adaptive Linear Predictors", Applied Optics, Vol. 24, p. 4247, 1985
15. Mansour, D., and A. H. Gray, Jr., "Unconstrained Frequency-domain Adaptive Filter," IEEE Trans Acoustics, Speech, and Signal Processing, Vol. ASSP-30, No. 5, October 1982.
16. Cioffi, J. M., "The Block-Processing FTF Adaptive Algorithm," IEEE Trans. Acoustics, Speech, and Signal Processing, Vol. ASSP-34, No. 1, February 1986.
17. Shynk, J. J., "Frequency-domain and Multirate Adaptive Filtering," IEEE Signal Processing Magazine, p.14, January 1992.
18. Welstead, S. T., Algorithms for Multichannel Adaptive Optical Processor, Final Technical Report, Contract F30602-88-D-0028, in preparation.
19. Goodman, J. W., Introduction to Fourier Optics, McGraw-Hill, New York, 1968.
20. VanderLugt, A., Optical Signal Processing, John Wiley and Sons, Somerset, NJ, 1992.
21. VanderLugt, A., "Signal Processing and Applications for Acousto-Optics", SPIE Tutorial T34, Orlando, FL, 8 April 1988.
22. Chang, I. C., "Acousto-Optic Devices and their Applications to Receiver Technology," SPIE Tutorial T11, Orlando, FL, 27 March 1989.

**MISSION
OF
ROME LABORATORY**

Rome Laboratory plans and executes an interdisciplinary program in research, development, test, and technology transition in support of Air Force Command, Control, Communications and Intelligence (C³I) activities for all Air Force platforms. It also executes selected acquisition programs in several areas of expertise. Technical and engineering support within areas of competence is provided to ESD Program Offices (POs) and other ESD elements to perform effective acquisition of C³I systems. In addition, Rome Laboratory's technology supports other AFSC Product Divisions, the Air Force user community, and other DOD and non-DOD agencies. Rome Laboratory maintains technical competence and research programs in areas including, but not limited to, communications, command and control, battle management, intelligence information processing, computational sciences and software producibility, wide area surveillance/sensors, signal processing, solid state sciences, photonics, electromagnetic technology, superconductivity, and electronic reliability/maintainability and testability.